System Performance Modeling of the Lunar Flashlight CubeSat Instrument

Author: Quentin Vinckier[1] (322 - vinckier@jpl.nasa.gov)

Co-authors: Paul O. Hayne[2], Jose M. Martinez-Camacho[1] (322), Christopher Paine[1] (382), R. Glenn Sellar[1] (383), Udo J. Wehmeier[1] (383), Barbara A. Cohen[3]

[1] Jet Propulsion Laboratory, California Institute of Technology, Pasadena, CA 91109

[2] University of Colorado, Boulder, CO 80309

[3] NASA Goddard Space Flight Center, Greenbelt, MD 20771

Lunar Flashlight mission

- Lunar Flashlight (LF) is an innovative CubeSat mission to be launched by NASA's AES (Advanced Exploration Systems) division on the first SLS (Space Launch System) test flight.
- **Goal ?** Detect, quantify and map surface H_2O ice in the PSRs (Permanently-Shadowed Regions) – where previous missions have already revealed strong indications of H_2O ice presence [1-6] – and occasionally sunlit regions of the lunar South Pole. In addition to be identified as a NASA Strategic Knowledge Gap (SKG) for Human Exploration, polar volatile deposits are also crucial to address outstanding questions in planetary science, such as testing hypotheses regarding the delivery and retention of water and other volatiles in the inner Solar System.
- **How ?** By measuring 0° phase angle bidirectional surface reflectance band ratios using four different wavelengths in the SWIR (shortwave infrared) spectral region between 1 and 2 µm.

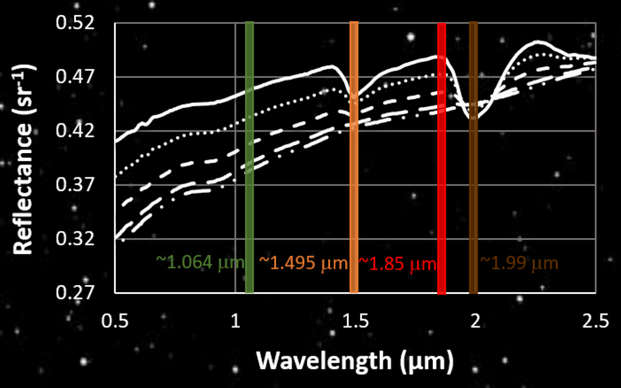

wt%: H_2O ice weight percent. Spectra calculated using Hapke theory [7], with water ice optical constants from [8] and a reflectance spectrum of Apollo 14 lunar highlands sample 14259-85.

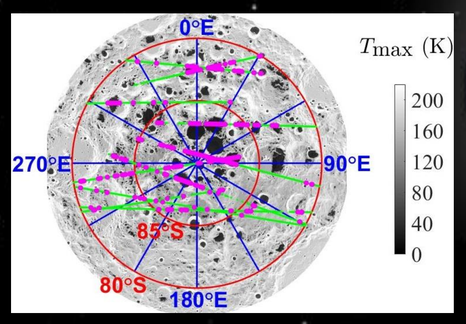

LF spacecraft Science data paths on the lunar South Pole. The gray scale shows the maximum temperature; the green and pink segments are the Science paths with the pink dots indicating the PSRs.

- The lasers fire sequentially for 1-6 ms , followed by a pause of 1-6 ms with all lasers off.
- When all lasers are off, background is measured and subtracted from the measured signals.
- In order to increase the SNR (Signal-to-Noise Ratio), measurements are averaged for each of the spectral band over the lunar ground-track corresponding to the desired mapping resolution.
- Continuum/absorption reflectance band ratios are then analyzed to quantify the weight percent of water ice (wt%) in the illuminated FOV (Field Of View).

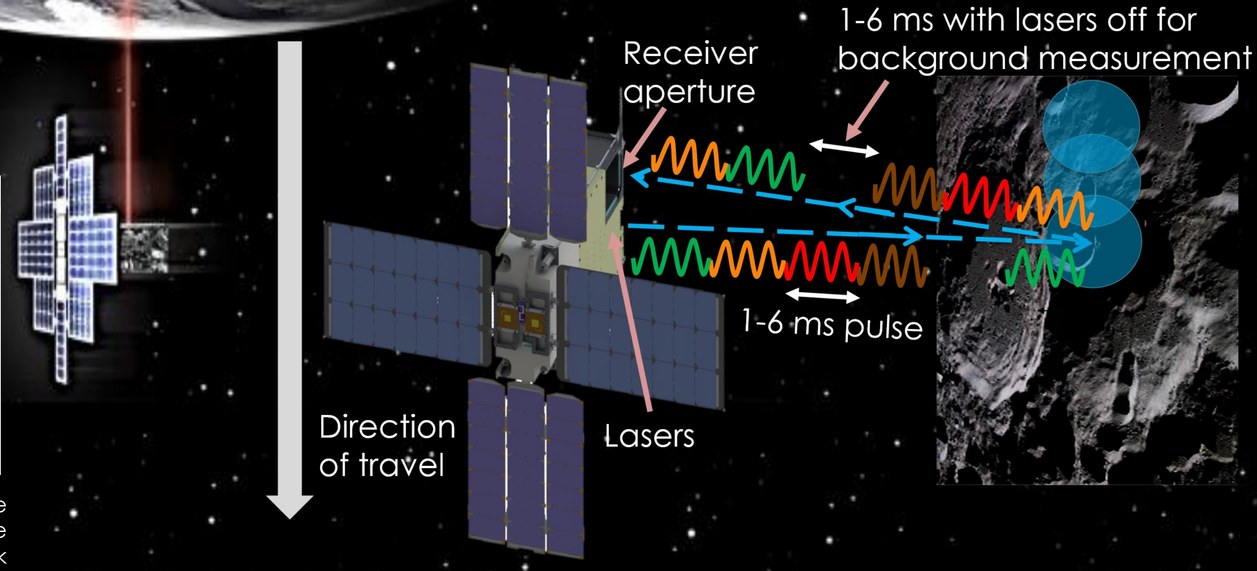

System modeling

We have modeled Gaussian and systematic uncertainty sources as a function of the spacecraft position for each of the wavelength. From this, we evaluate the fraction of covered area for which the SNRs are high enough to discriminate between dry regolith and a given water ice content as a function of the confidence level. Below is the estimated error tree corresponding to a mapping resolution of 10 km (i.e. after averaging) and 6 ms pulses, using the two shortest wavelengths. TBD (To Be Determined) values have been set to zero.

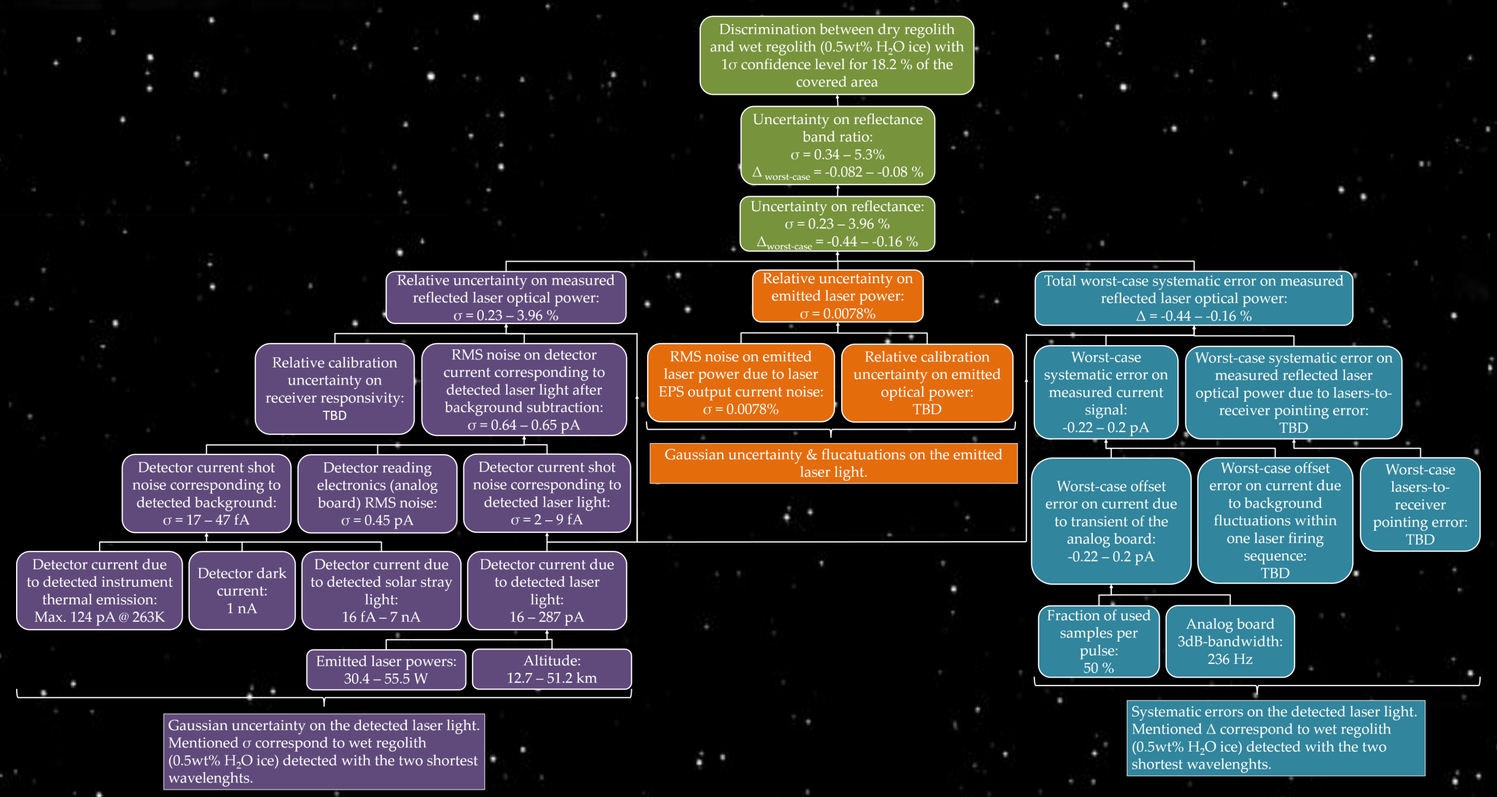

LF multi-band SWIR laser reflectometer

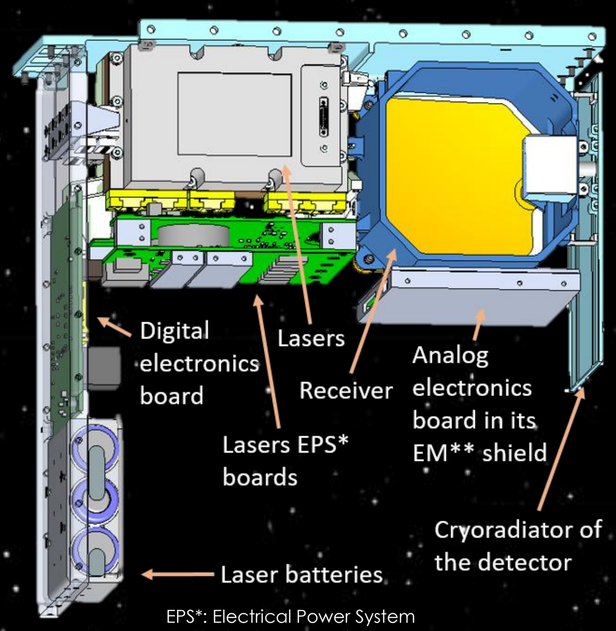

EPS*: Electrical Power System
EM**: ElectroMagnetic

- Optical receiver: 70×70-mm off-axis Al paraboloidal mirror; 70 mm focal length; single pixel 2 mm diameter InGaAs detector cooled at -65°C (1 nA dark current); 20.2 mrad uniform FOV; optimized for stray solar light rejection from outside the FOV.
- Detector reading electronics (analog board): 0-10 nA current range; 0.5 pA/Hz$^{1/2}$ RMS (Root Mean Square) Nyquist noise spectral density; 236 Hz 3dB-bandwidth.
- Diode lasers: 15-55 W optical power; wavelengths: ~1.495 µm & ~1.99 µm (H_2O ice absorption peaks) and ~1.064 µm & ~1.850 µm (nearby continuum); > 99.6% emitted energy encircled within 20.2 mrad.

Results and Discussion

Mapping resolution: 10 km & Pulse width: 6 ms

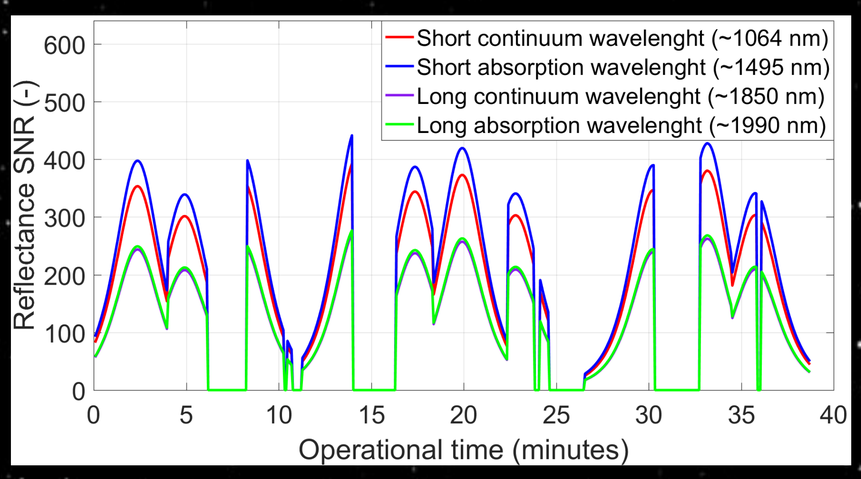

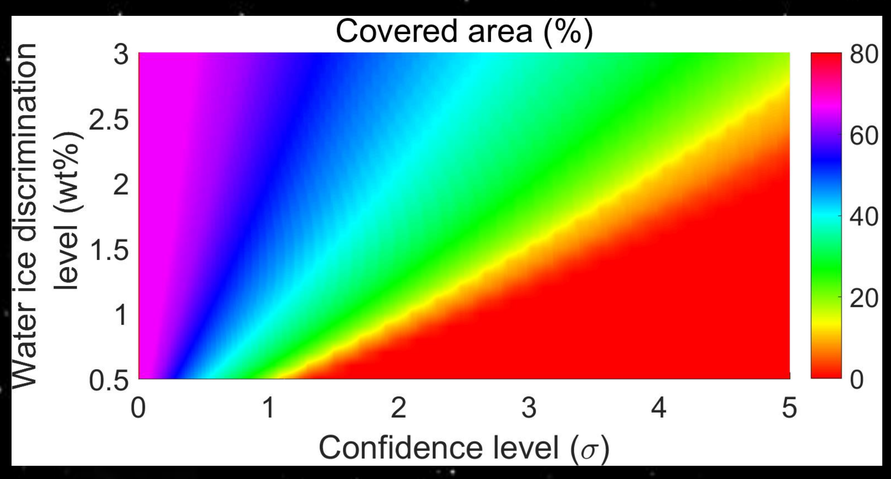

Conclusion:

- The detector reading electronics (analog board) constitutes the major source of noise.
- Thermal constraints limit the laser power available, and thus the instrument SNR.
- Trade off between mapping resolution and instrument SNR.
- This highly mass- and volume-constrained (2U) instrument payload will demonstrate several firsts at a much lower cost than previously possible, including being one the first instruments onboard a CubeSat performing science measurements beyond low Earth orbit and the first planetary mission to measure reflectance using active sources from orbit.

Next steps:

- Complete TBD values in the error tree (achievable instrument calibration accuracy, background fluctuations impact, lasers-to-receiver pointing error) and finalize the calculations of the instrument performance. .
- Manufacture of flight modules, calibration & characterization, integration to the CubeSat.

National Aeronautics and Space Administration

Jet Propulsion Laboratory
California Institute of Technology
Pasadena, California
www.nasa.gov

[1] Paige, D. A., et al. (2010) Science, 330, 479-482. [2] Mitrofanov, I. G., et al. (2010) Science, 330, 483-486. [3] Gladstone, G. R., et al. (2012) JGR, 117, E00H04. [4] Zuber, M. T., et al. (2012) Nature, 486, 378-381. [5] Hayne, P. O., et al. (2015) Icarus, 255, 58-59. [6] McCord, T. B., et al. (2011) JGR, 116. [7] Hapke, B. (1981) JGR, 86(B4), 3039-3054. [8] Warren, S. G., & Brandt, R. E. (2008) JGR, 113(D14).

Poster No. T-01

National Aeronautics and Space Administration

WATSON: An ultraviolet Raman and fluorescence spectrometer for subsurface organic detection on the Greenland ice sheet

Evan Eshelman (3225), Greg Wanger (USC), Michael J. Malaska (3225), Kenneth S. Manatt (3225), Madelyne C. Willis (MSU), William J. Abbey (3225), Luther W. Beegle (3225), John C. Priscu (MSU), Rohit Bhartia (3225)

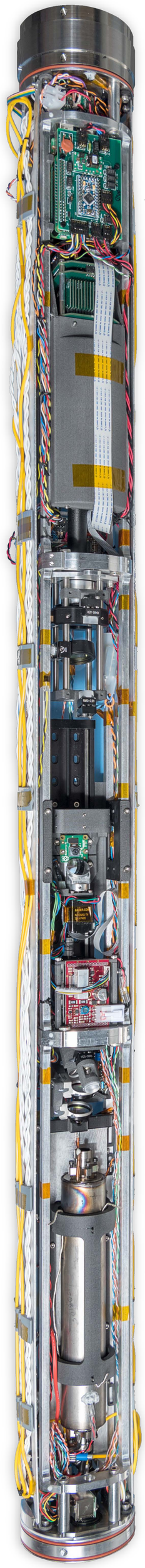

Power / electronics
An onboard CPU, electronics, and power package coordinate the firing of the laser with the motorized stages and communication with the detector.

Spectrometer
A filter in the spectrometer separates Raman and fluorescence emission, sending each component to separate gratings and focusing onto two 32 channel PMT detectors.

Motorized carriage
Motorized carriage on a linear stage containing the focusing objective, context camera, and rotational mirror for rastering the laser across the sample surface.

Laser cleanup optics
Exiting the laser, the 248.6 nm line is isolated and other NeCu transitions, primarily a 252.9 nm line, are removed by two custom edge filters

Laser and LPS
Excitation is provided by a 248.6 nm NeCu hollow-cathode laser, along with a custom laser power supply capable of operating up to 160 Hz.

Instrument overview and objectives

Icy environments have been found to both preserve organic material and even contain potentially habitable niches[1,2]. Traditional methods of ice analysis involve melting bulk samples, losing spatial information regarding the distribution of cells and their relation to other chemical or morphological features.

WATSON's goal is to determine the spatial distribution of organic material, including microbes, present in glacial ice by in situ measurements of the ice borehole wall, obtaining spectral maps containing signatures of organic material present.

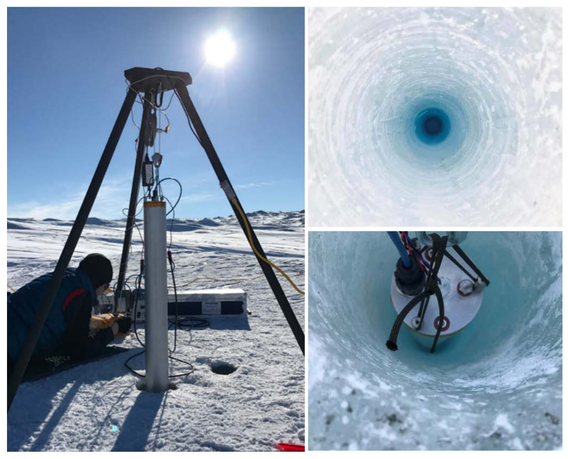

Left: WATSON prototype engineering deployment in Kangerlussuaq, Greenland. A 14 cm × 4.5 m borehole was used for WATSON testing.

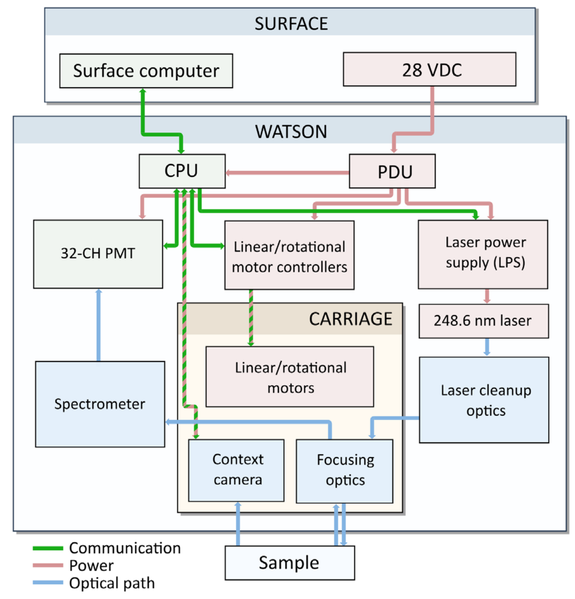

WATSON block diagram. A surface power supply and computer are connected to WATSON through an Ethernet and power tether. Inside WATSON, a CPU and power distribution unit control and power the PMT detectors, motors for scanning the laser across the sample, and the laser power supply.

Combined Raman and fluorescence spectrometer

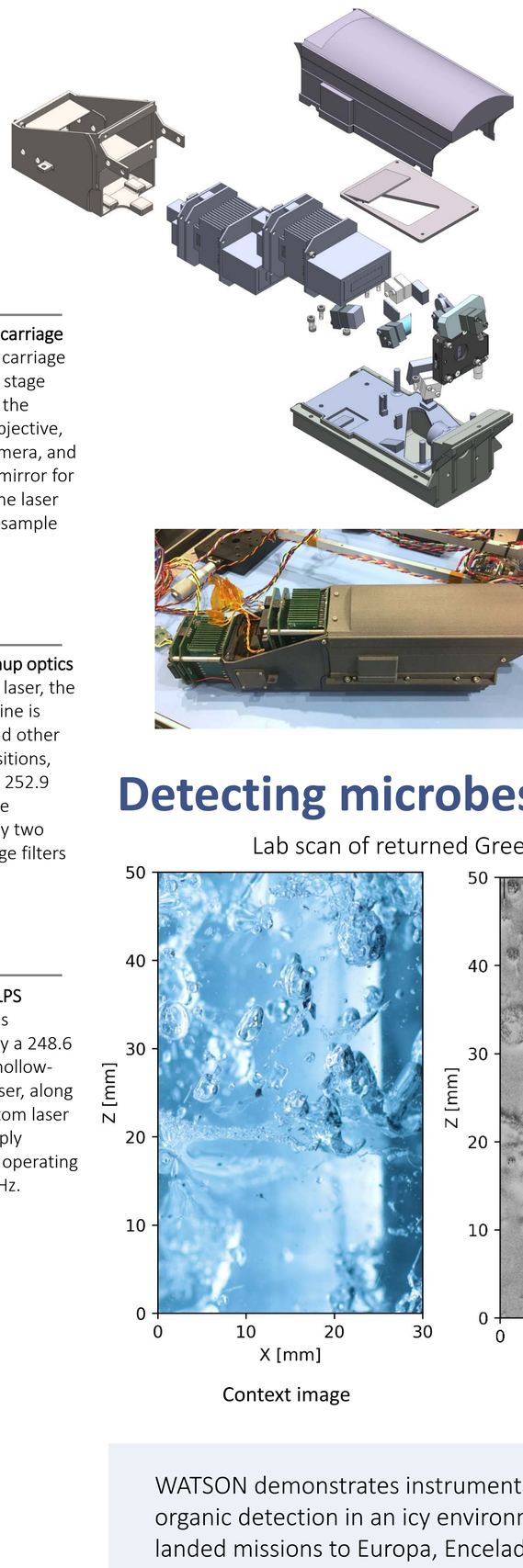

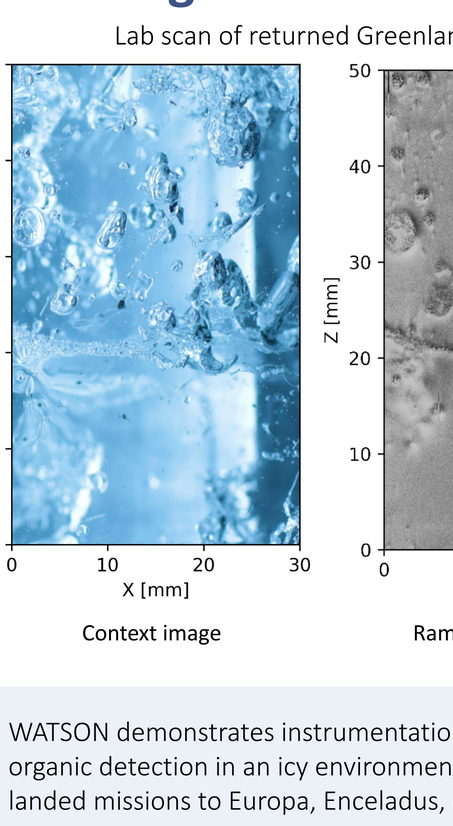

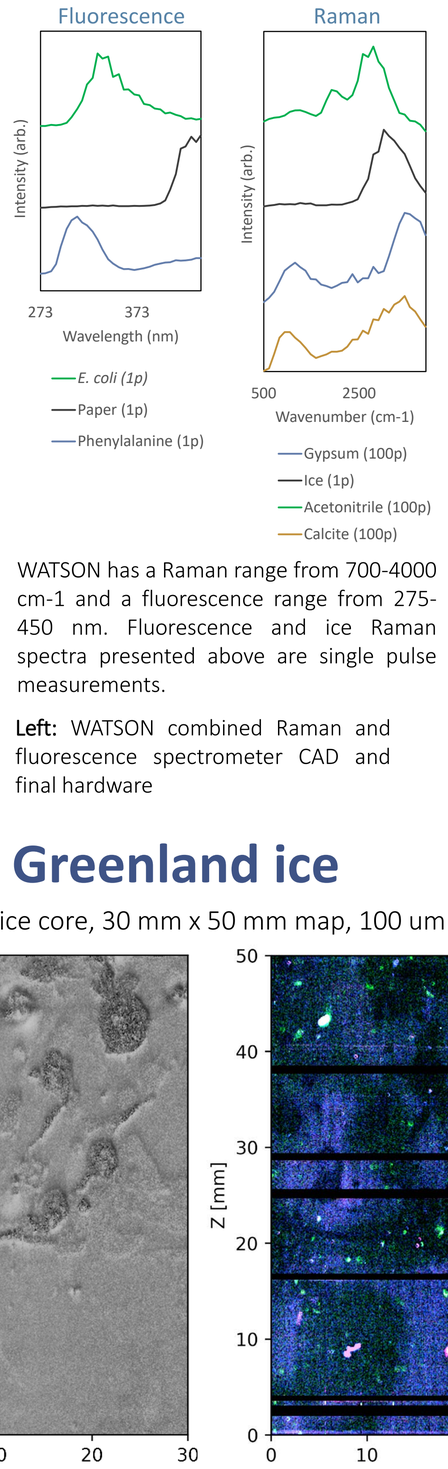

WATSON has a Raman range from 700-4000 cm-1 and a fluorescence range from 275-450 nm. Fluorescence and ice Raman spectra presented above are single pulse measurements.

Left: WATSON combined Raman and fluorescence spectrometer CAD and final hardware

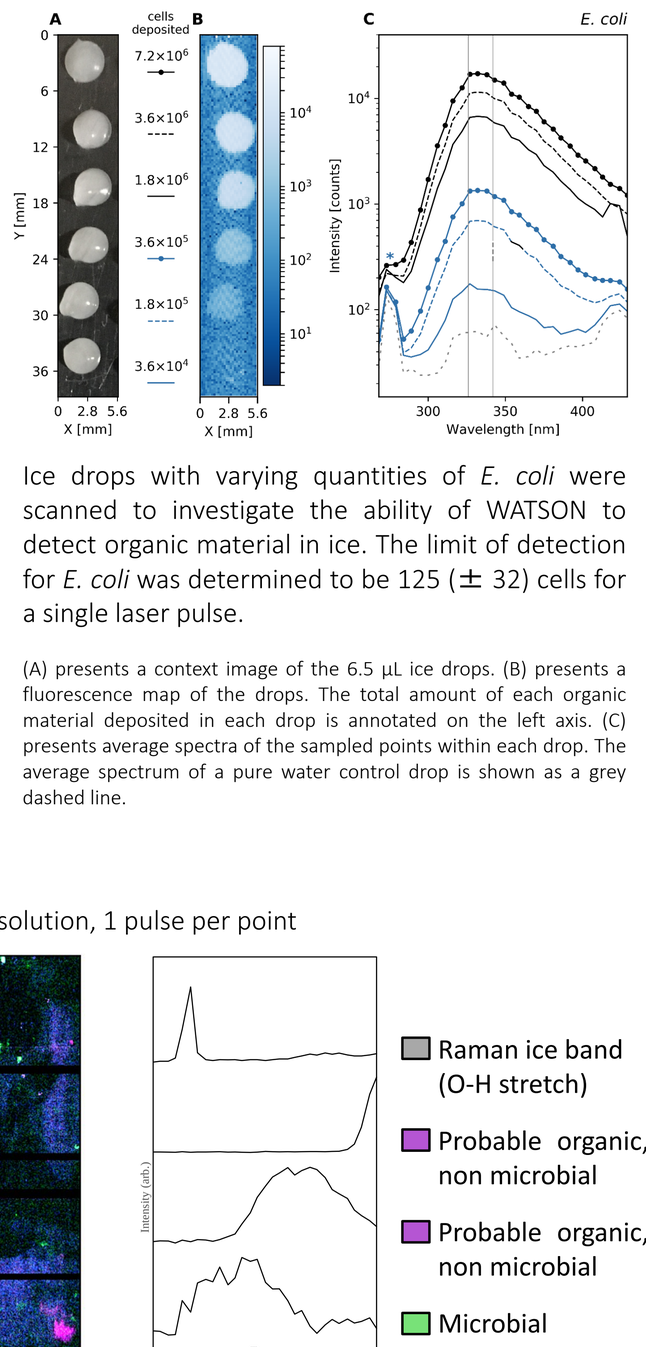

Ice drops with varying quantities of *E. coli* were scanned to investigate the ability of WATSON to detect organic material in ice. The limit of detection for *E. coli* was determined to be 125 (± 32) cells for a single laser pulse.

(A) presents a context image of the 6.5 µL ice drops. (B) presents a fluorescence map of the drops. The total amount of each organic material deposited in each drop is annotated on the left axis. (C) presents average spectra of the sampled points within each drop. The average spectrum of a pure water control drop is shown as a grey dashed line.

Detecting microbes in Greenland ice

Lab scan of returned Greenland ice core, 30 mm x 50 mm map, 100 um resolution, 1 pulse per point

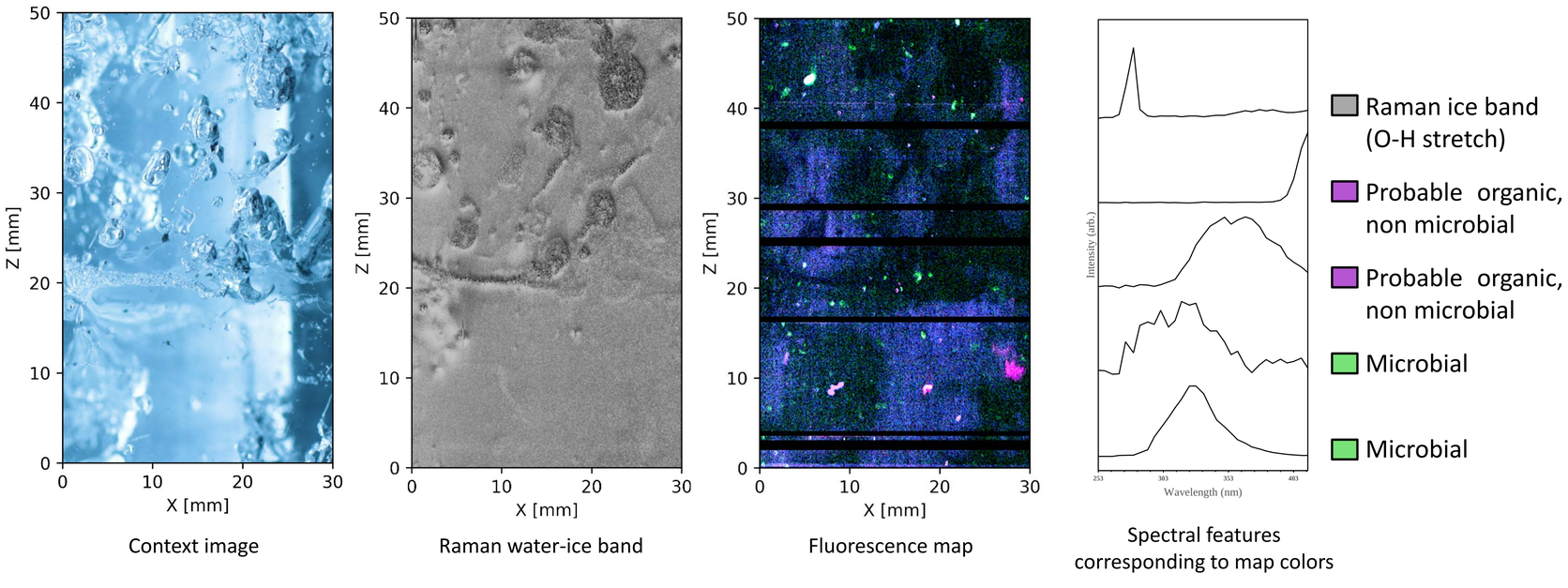

WATSON demonstrates instrumentation and measurement techniques for organic detection in an icy environment that may be desirable for future landed missions to Europa, Enceladus, or the Martian polar caps.

This work was carried out at the Jet Propulsion Laboratory, The California Institute of Technology under a PSTAR contract from NASA. Thanks to Jim Wilcox and Photon Systems for electronics support.

National Aeronautics and Space Administration

Jet Propulsion Laboratory
California Institute of Technology
Pasadena, California

[1] J. C. Priscu, C. H. Fritsen, E. E. Adams, S. J. Giovannoni, H. W. Paerl, C. P. McKay, P. T. Doran, D. A. Gordon, B. D. Lanoil and J. L. Pinckney (1998). Perennial Antarctic lake ice: An oasis for life in a polar desert. Science, 280 (5372), 2095-2098.
[2] V. Miteva, C. Teacher, T. Sowers and J. Brenchley (2009). Comparison of the microbial diversity at different depths of the GISP2 Greenland ice core in relationship to deposition climates. Environmental Microbiology, 11 (3), 640-656.

Poster No. T-02

National Aeronautics and Space Administration

Precision Radial Velocity at Palomar Mountain: PARVI and P3K

Author: Christopher Matthews (326)
Co-Authors: Gautam Vasisht (326) and the PARVI team

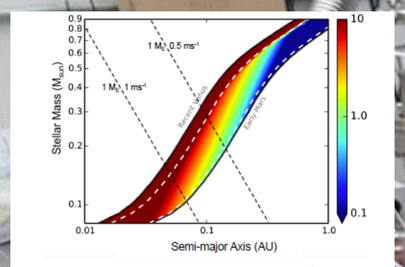

Figure 1.1-1. Improving RV sensitivity from 50 cms^{-1} opens up orbital space. A stellar mass vs. semi-major axis diagram showing the boundary to which 1 M$_E$ planets may be detected with 1 ms^{-1} and 0.5 ms^{-1} RVs. The colors within the HZ show Earth-ocean masses lost via UV driven escape due to proximity to the star. Dry worlds are in red, wetter ones in blue.

PARVI

The Palomar Radial Velocity Instrument (PARVI) is a fiber-fed diffraction-limited near-IR spectrograph being built for the P3K ExAO system on the Hale telescope at Palomar Observatory. By working at the diffraction limit PARVI maintains a small footprint and can be kept extremely stable, and thus will provide improved RV sensitivity. By combining an extremely stable spectrograph with an f-2f locked self-referencing laser frequency comb (LFC) for calibration PARVI has a goal of detecting reflex motions as small as 30 cm/s. The instrument is currently being built using components from the Project 1640 Coronagraph and Hyperspectral Imager (P1640) which recently completed its 99 night direct imaging survey at Palomar Observatory. Reusing the P1640 H2RG detector, cryostat, and breadboard as well as parts of the control software and electronics has greatly accelerated PARVI's development and the team aims to begin commissioning at Palomar in early 2019.

P1640 bellow the Hale Cass cage

P3K

The Palm 3000 (P3K) extreme adaptive optics (ExAO) system is the facility AO instrument for the Hale telescope.

- The system uses a 64x64 subaperture Shack-Hartmann wavefront sensor (WFS)
- A 66x66 actuator high-order deformable mirror (DM) and a 349 actuator low-order DM in a woofer-tweeter configuration provide high Strehl ratio correction

P3K is currently undergoing an upgrade to the WFS arm. The transmissive optics in the path have been replaced to improve throughput and remove a know residual astigmatism in the WFS. The camera is being replaced with a new deep-depletion EMCCD OCAM-2K camera developed by First Light Imaging. The new camera will provide faster frame rates (3kHz) and improved sensitivity particularly in the red to NIR part of the spectrum. The RTC hardware and software is also being upgraded, moving from a GPU based architecture to a faster and more reliable DSP based system.

Motivation

The radial velocity (RV) method has detected 254 planets since the discovery of 51 Peg b in 1995. The majority of these were detected using optical spectrographs, which have recently surpassed 1 m/s sensitivity. IR observations have been limited in the past due to technical restrictions, but improvements in AO and IR detector technology provide the potential for precision RV (PRV) observations in the IR. Recent discoveries, such as the TRAPPIST-1 planets, have also peaked interest in cooler stars which are particularly amenable to IR observations.

PARVI is designed to provide 30 cm/s sensitivity in the near-IR (NIR) between 1.2 – 1.8 µm. This provides a great opportunity to investigate several poorly understood classes of exoplanets.

- **Planets around M stars:** PARVI will have sufficient sensitivity to detect an Earth-mass planet in the habitable zone around cool M dwarfs
- **Young exoplanets:** PARVI will allow the detection of forming gas giants, as well as young planets around nearby stars.
- **TESS/K2 follow up:** PARVI will also provide valuable follow up of transiting planets discovered by TESS and K2, allowing better determination of the planet's physical properties

PARVI will also provide valuable technology development for ground-based PRV spectrographs, as well as Laser Frequency Comb development which will be of great value to future spectrographs both in ground-based facilities as well as future space missions.

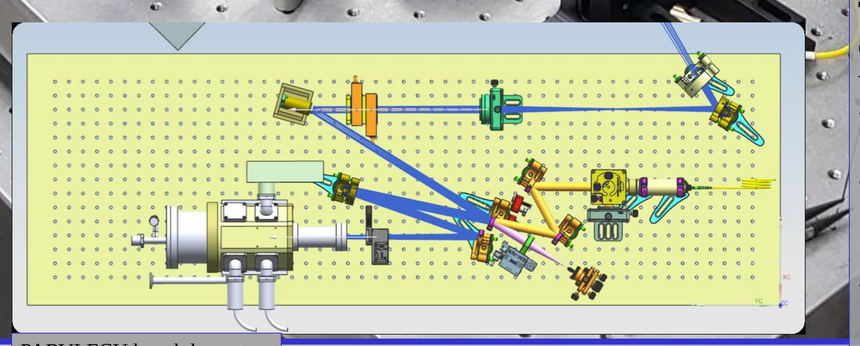

PARVI FCU bench layout

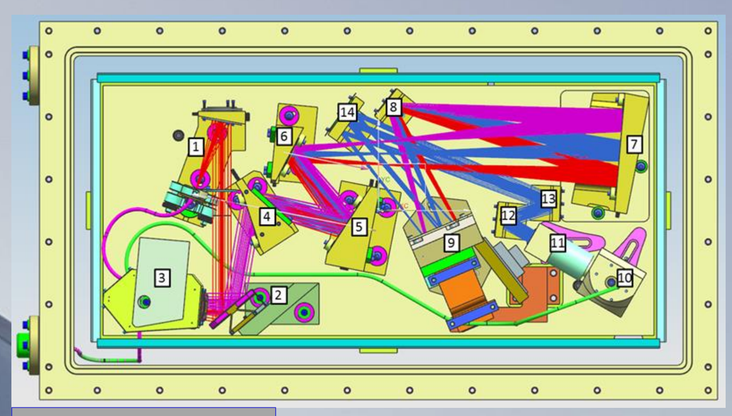

PARVI Spectrograph layout

PARVI has three primary components

The Fiber Coupling Unit (FCU) interfaces with the P3K ExAO system, coupling the light from the 200in Hale Telescope into a single mode fiber which leads to the spectrograph located in a separate location.

- By using SMF minimal modal noise is introduced and a space-quality PSF can be obtained
- Locating the spectrograph away from the telescope removes the changing gravity vectors, reduces vibration and thermal variation which reduce RV sensitivity
- Using a fiber connection also means the spectrograph itself never needs to be installed/removed from the telescope, providing improved stability between observing runs
- Light from the LFC is injected into the science fiber using the FCU

The Spectrograph is a cross-dispersed Echelle design fed by fiber connections to the FCU mounted in the Cass cage of the Hale telescope.

- The R4 Echelle grating will provides a resolving power of R~90,000 to 125,000
- A silicon prism (the only transmissive optic in the spectrograph) cross-disperses the spectra
- A three-mirror anastigmat images 2 NIR bands on the 2Kx2K H2RG detector
- The LFC provides relative wavelength calibration, a thermal source and gas-cell (CO_2, CH_4, C_2H_2) provides an absolute wavefront reference, and a monochrometer provides color-dependent flats
- The compact design of the spectrograph combined with its physical isolation will provide excellent stability at a fraction of the cost of traditional seeing-limited designs

The Laser Frequency Comb (LFC) provides a stable and well calibrated wavelength reference over the 1.2 – 1.8 µm bandpass of the spectrograph.

- The LFC will be located remotely in the observatory computer room
- LFC development for PARVI will advance astrocomb technology readiness, helping pave the way for future ground and space-based implementations
- Several upgrades are already planned for the LFC to improve the initial 10 cm/s comb stability to an ultimate goal of 3 cm/s

ID	Technology	Technology Gap	Technology Description	Current Performance	Needed Performance
M-1	**Extreme Precision Ground-based Radial Velocity**	Radial Stellar Motion	Ground-based radial velocity instrumentation capable of measuring the mass of candidate exo-Earths in the habitable zone and to maximize efficiency of space telescope surveys.	Single measurement precision: 80 cm/s HARPS instrument; NN-EXPLORE's NEID (WYNN observatory) in development: goal 27 cm/s	Signal from exo-Earths is 10 cm/s; Need to reduce systematic errors to 1 cm/s on multi-year timescales; statistical uncertainties of 1 cm/s on monthly timescales for late F, G, and early K stars
M-2	**Laser Frequency Combs**	Radial Stellar Motion	Laser Frequency Combs (LFCs) are precise calibration sources for extreme-precision radial velocity measurement.	Lab: Electro-optic-modulation frequency combs demonstrated on ground-based observatories with needed mode spacing, need miniaturization and power reduction. Non-NASA work is advancing miniaturization. Flight: Fiber laser-based optical frequency combs demonstrated on sounding rocket (TEXUS 51 4/15 and TEXUS 53 1/16) w/ ~ few hundred MHz mode spacing. System mass is > 10 kg.	Space-based Laser Frequency Combs to calibrate high resolution, fiber-fed spectrographs for radial velocity precision better than 10 cm/s. Desired parameters are: • mode spacing of 5-10 GHz • bandwidth span 380 nm to 2400 nm • Allen deviation < 10^{-10} • Low SWaP

Figure 1.1.2. The technologies for Precision Radial Velocity and Laser Frequency Comb are identified in the Exoplanet Exploration Progam's Technology Gap List as excerpted here (https://exoplanets.nasa.gov/exep/technology/gap-lists/).

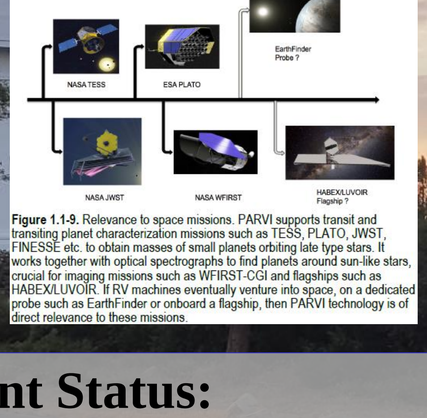

Figure 1.1-9. Relevance to space missions. PARVI supports transit and transiting planet characterization missions such as TESS, PLATO, JWST, FINESSE etc. to obtain masses of small planets orbiting late type stars. It works together with optical spectrographs to find planets around sun-like stars, crucial for imaging missions such as WFIRST-CGI and flagships such as HABEX/LUVOIR. If RV machines eventually venture into space, on a dedicated probe such as EarthFinder or onboard a flagship, then PARVI technology is of direct relevance to these missions.

Current Status:

- The P3K WFS frontend optics have been replaced. The new WFS camera will be installed later this year when the Hale secondary is removed for recoating
- The PARVI Spectrograph is currently being assembled, with the camera undergoing initial warm alignment.
- The PARVI FCU is undergoing initial alignment. The FCU camera is being characterized and the ADC assembly is being designed.
- An initial LFC has been demonstrated with NIRSPEC at Keck, and the comb has been successfully broadened to cover the full PARVI bandpass.

PARVI Instrument Error Budget

Instrumental Error (Uncalibratable)	**15.7**
Fiber & Illumination	**5.8**
Calibration source modal noise	0
Continuum modal noise	0
Near-field scrambling	0
Far-field scrambling	0
Stray light and ghosts	3
Polarization	5
Focal ratio degradation (science)	0
Focal ratio degradation (calibration)	0
Double scrambler mechanical drift	0
Fiber Fiber contamination	0
Reformater drift	0
Detector effects	**13.1**
Latent images	9
Pixel inhomogeneity/Non-linearity	9
Interpixel capacitance	3
Barycenter correction	**4.2**
Algorithms	1
Exposure midpoint time	4
PSF variation	1
Coordinates and proper motion	0
Reduction pipeline	**5.0**
Software algorithms	5

Instrumental Error (Calibratable)	**31.4**
Calibratable Error Contribution	**4.7**
Thermal-Mechanical	**29.6**
Thermal stability (grating)	9
Thermal stability (cross-disperser)	15
Thermal stability (bench)	12
Thermal stability (camera)	8
Optical elements (tilt)	10
Vibrational stability	2
Pressure stability	5
LN2 fill transient	15
Zerodur phase change	1
Optical elements (focus)	3
Detector effects	**10.5**
Pixel inhomogeneity	10
Electronic noise	1
Pixel location error	0
Detector thermal expansion	3
Readout thermal transients	0
CTE	0
Total Instrumental Error	**19.8**

Calibration Source (Uncalibratable)	**11.0**
Calibration Source (uncalibratable)	**10.2**
Wavelength stability	10
Photon noise	2
Calibration process	**4.0**
Software algorithms	4
External Error (Uncalibratable)	**0.0**
Telescope	**0.0**
Guiding errors	0
Atmospheric Dispersion Corr.	0
Focus	0
Windshake	0
General Parameter	**Value**
Calibration factor	0.85
On sky fiber diameter (")	0.06
Instr. Resolution	100000
Number of science slices	1

National Aeronautics and Space Administration

Jet Propulsion Laboratory
California Institute of Technology
Pasadena, California

www.nasa.gov

Poster No. T-04

National Aeronautics and Space Administration

Tropospheric ozone lidar upgrade and automation at JPL Table Mountain Facility

Author: Fernando Chouza-Keil (329H)
Thierry Leblanc (329H), Mark Brewer (329H), Patrick Wang (329H)

Abstract As part of the international efforts to monitor global ozone, different satellite missions (e.g. TROPOMI) were deployed and others, like TEMPO, are planned for the near future. Considering the importance of the validation stage of these missions, several modifications were introduced to the TMF tropospheric ozone lidar to provide accurate and extensive datasets for this purpose. These modifications include 1) the full automation of the system, which is now capable of measuring automatically and autonomously during satellite overpasses, and 2) the addition of a new receiver extending the measurement capabilities of the system down to about 120 m above the surface. The characterization of this new receiver, based on an ozone sensor carried by a tethered balloon, is also discussed.

System automation

The system automation hardware was implemented in a modular approach in order to ease its migration to other TMF lidar systems. Communication between subsystems is conducted via Ethernet interface, while to power of each subsystem is controlled with an Ethernet controlled Power Distribution Unit (PDU). Since there is no window protecting the lidar from precipitation, a hardware interlock was implemented to ensure that in case of precipitation and hardware failure, the protective hatch automatically close.

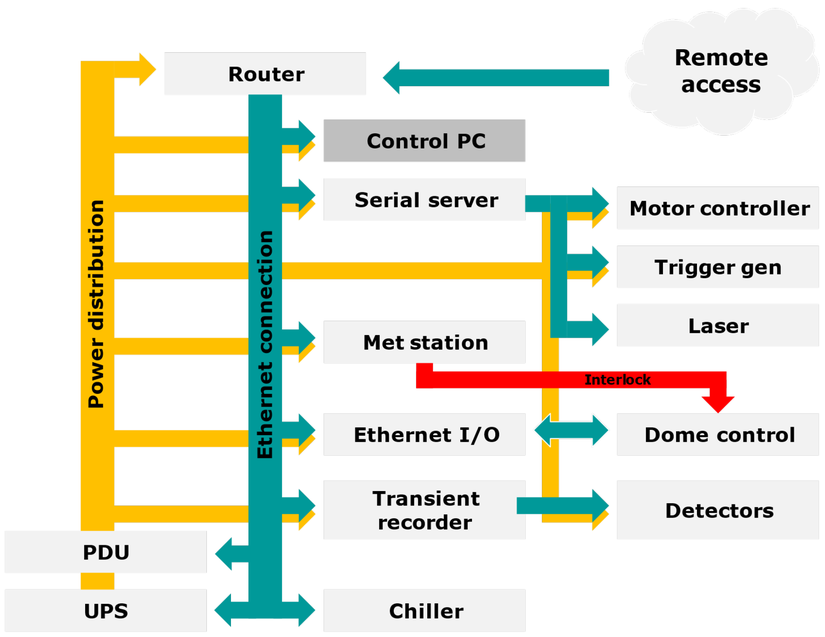

Figure 1. Automation hardware block diagram

The control software is implemented in Python, with a web browser-based user interface implemented with Bokeh library. The control software is divided in five different modules: a web interface that allows the programming of the system and the monitoring of its status, a scheduler that deliver the program commands to the rest of the modules, a housekeeping module that controls most of the lidar hardware, an alignment module that performs alignment on the receivers before each measurement period and an acquisition module that stores the measurements together with system status data and meteorological data to help to interpret measurements and help on the debugging of possible problems.

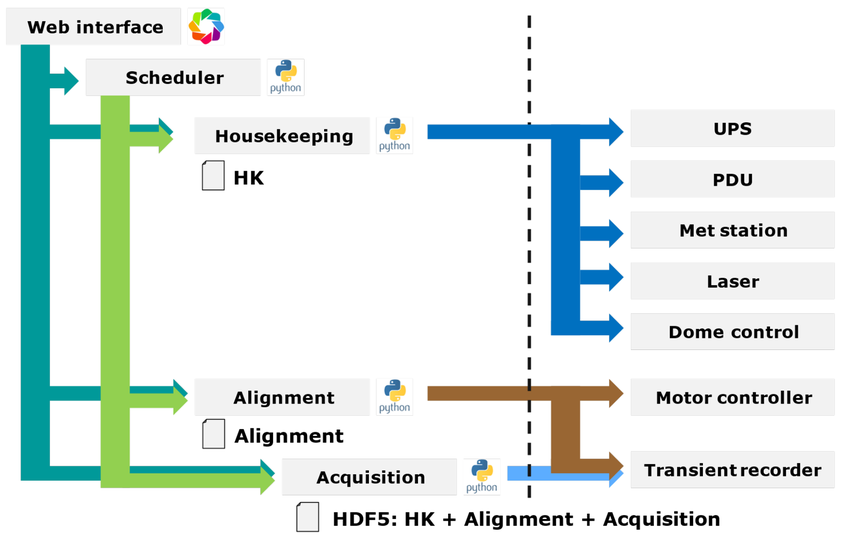

Figure 2. Automation software block diagram

Very-near-range receiver

A novel very-near-range receiver was developed in order to reduce the minimum achievable range of the tropospheric ozone lidar to about 100 m AGL. Atmospheric backscatter is collected by a 2-inch lens and divided in two beams by a pellicle beam splitter (BS) which minimizes the overlap difference between both arms of the receiver. Interference filters (IFs) filter out solar background light and the reciprocal DIAL wavelength before being detected by the photomultipliers (PMTs).

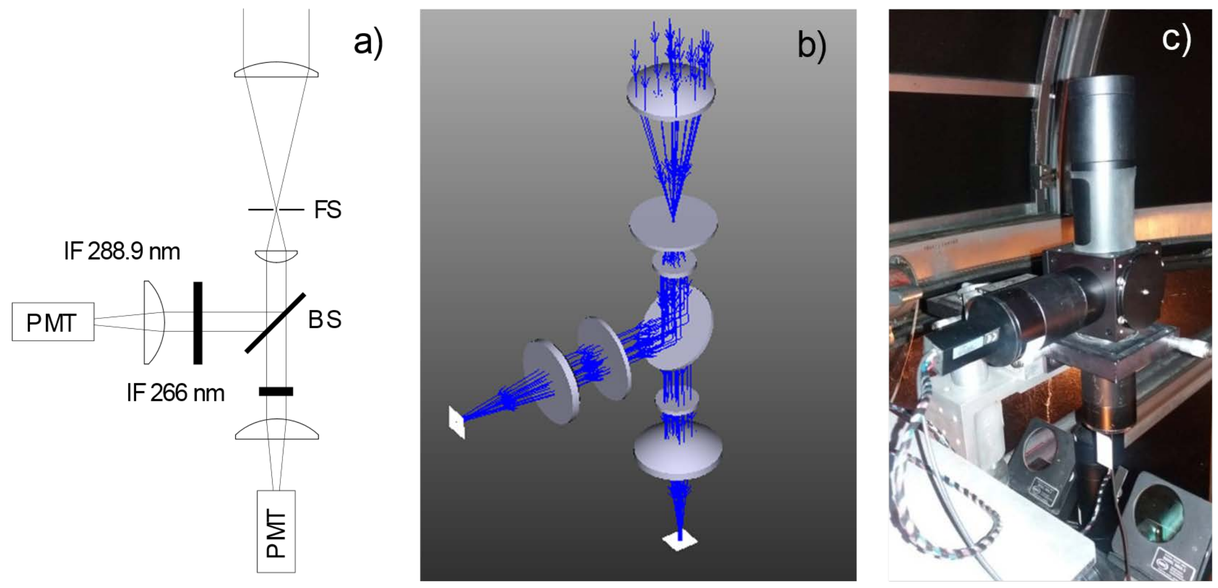

Figure 3. a) Block diagram of new very-near-range receiver. FS is a field-stop, BS is a dichroic beamsplitter, IF are interference filters and PMTs are the photomultipliers. b) Raytracing simulation of the receiver. c) Photo of the actual receiver.

As part of the validation procedure for this new very-near-range receiver, a set of measurements with a balloon-borne ozone sonde were conducted. Results show a very good agreement down to about 120 m AGL. This additional channel would allow to investigate near surface ozone variability as required for air quality studies.

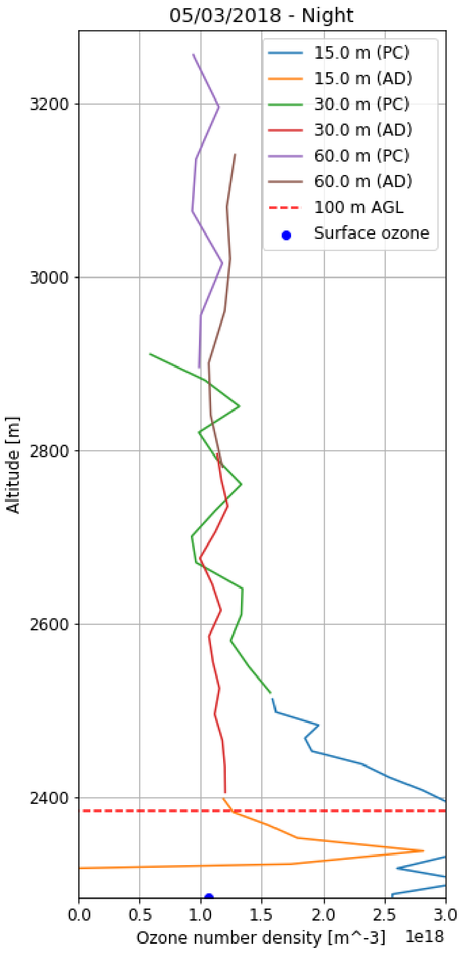

Figure 4. Example of measurements conducted with the new very-near-range channel using analog detection (AD) and photocounting detection (PC). Surface ozone measurements are shown for comparison.

Conclusions

The new automation capabilities increased the TMF ozone lidar system capabilities to perform measurements as required for long-term ozone monitoring as well as satellite validation. On the other hand, the additional receiver, validated by means of surface ozone measurements and balloon-borne ozone sonde indicate, reduced the minimum achievable range from 1 km to 120 m AGL.

National Aeronautics and Space Administration

Jet Propulsion Laboratory
California Institute of Technology
Pasadena, California

www.nasa.gov

Poster No. T-05

National Aeronautics and Space Administration

A 90-102 GHz CMOS Based Pulsed Fourier Transform Spectrometer: Development of a Portable High-Resolution Millimeter Wave Gas Sensor

Deacon J. Nemchick (329H), Brian J. Drouin (329H)

Introduction

- We present a system level description of a cavity enhanced millimeter-wave spectrometer that is the first in its class to combine source and detection electronics constructed from architectures commonly deployed in the mobile phone industry and traditional pulsed Fourier transform techniques to realize a compact device capable of sensitive and specific *in situ* gas detections.
- The instrument, which has an operational bandwidth of 90 - 102 GHz, employs several unique components including a custom designed pair of millimeter-wave transmitter and heterodyne receiver integrated circuit chips constructed with 65 nm complementary metal-oxide semiconductor (CMOS) techniques.
- These elements are directly mated to a hybrid coupling structure that enables free-space interaction of the electronics with a small gas volume while also acting as a cavity end mirror. Instrument performance for sensing of volatile compounds are highlighted with experimental trials taken in bulk gas flows and seeded molecular beam environments.

JPL Developed SpecChip Instrument

- Instrument mimics a Balle-Flygare style pulsed Fourier transform spectrometer where millimeter wave radiation is injected into a resonant Fabry-Perot cavity containing an gas analyte.
- The keystone constituent is a printed circuit board (PCB) which hosts all source and detection electronics including a pair of millimeter-wave transmitter (Tx) and receiver (Rx) integrated circuit (IC) chips purpose built for this instrument.

CMOS Footprint	CMOS Power Consumption	Operational Bandwidth
<5 mm^2	~350 mW	90-102 GHz

- Gross mechanical adjustment of the mirror position afforded by a sliding stage that clamps directly to vertical guide rods with a piezoelectric stage allowing for precision tuning to sub-μm resolution over a 15 mm range.
- A custom designed hybrid element (coupler plate) serves as a cavity end mirror while also hosting embedded coplanar waveguide features for the direct injection (detection) of radiation into (out of) the optical cavity.

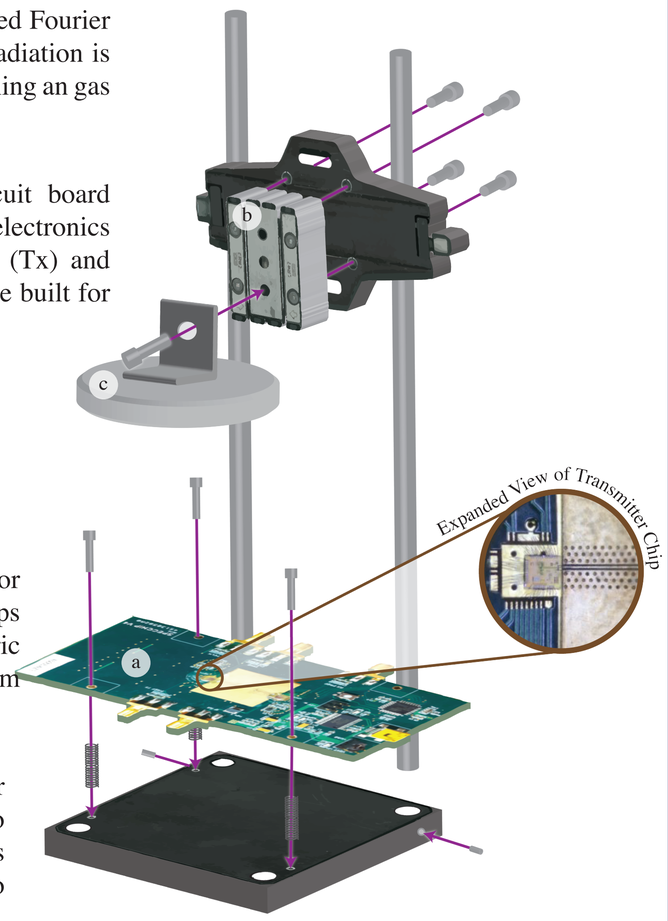

Automated Performance Across Instrument Bandwidth

- Bandwidth scanning accomplished with an automated routine that iteratively sets Tx/Rx SoCs and tunes optical cavity length.

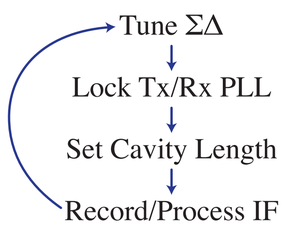

- A single cavity mode is tracked across the instrument bandwidth each of which was fit with a Lorentzian lineshape to extract cavity quality factors (also plotted).

Quality Factors	Effective Pathlength
4300 - 2800	2.28 - 1.32 m

- Instrument sensitivity allows for observation of multiple isotopologues in a bulk (3 mT) sample of carbonyl sulfide (OCS).

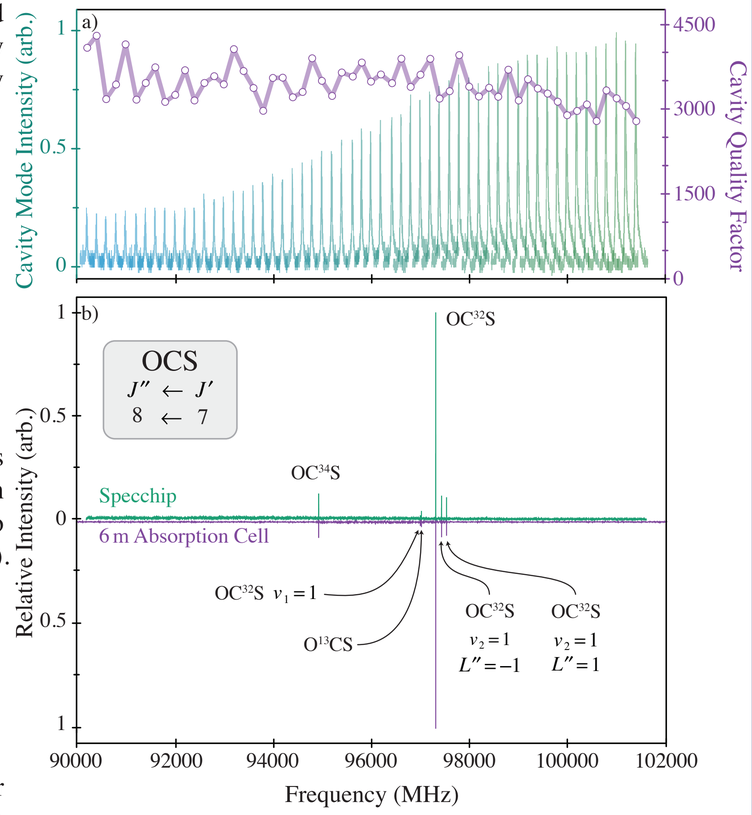

Isotopologues	$OC^{32}S$	$OC^{34}S$	$O^{13}C^{32}S$	$OC^{33}S$
Abundance	0.9374	0.04158	0.01053	0.0074

Overview of Printed Circuit Board Components

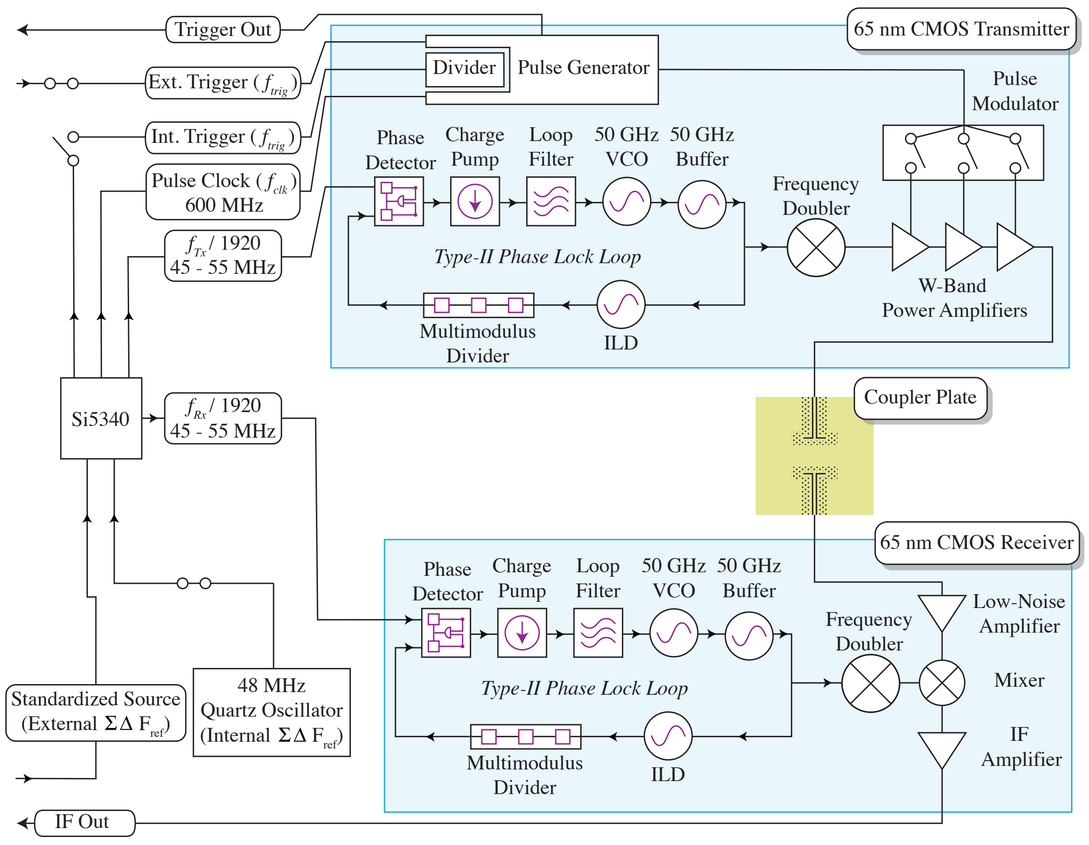

- The 90 - 102 GHz output of the transmitter and input of the receiver with matching bandwidth are wirebonded directly to separate grounded coplanar waveguides embedded in the planar cavity end mirror (*i.e.*, coupler plate).
- Supporting frequencies including f_{Tx}/1920, f_{Rx}/1920, f_{clk} (pulser clock), and f_{trig} (internal trigger), are provided by a ΣΔ clock generator which is also mounted on the PCB.

Sensitivity to Targeted Pure Rotational Transitions

- Detection limits determined by intersection of integrated peak volumes at various pressures with noise floor.
- Linear response indicates operating below the limit of perturbing influences such as self-broadening
- The echoes were collected with 50 ns excitation pulses where the first 5μs of the FID following the pulse is collected at a sampling rate of 1Gs/s with a total of 1500 time traces being averaged before Fourier transform.

Each trace constitutes 1 second of signal averaging/processing

- Repeated with different molecular resonances across the instrument bandwidth.

	CH_3CN	$OC^{34}S$	CH_3OH	$OC^{33}S$	N_2O
GHz	91.7	94.9	95.1	97.3	100.5

- Results for various mirror geometries can be used to formulate a generalized instrument sensitivity model using databased cataloged spectroscopic parameters.

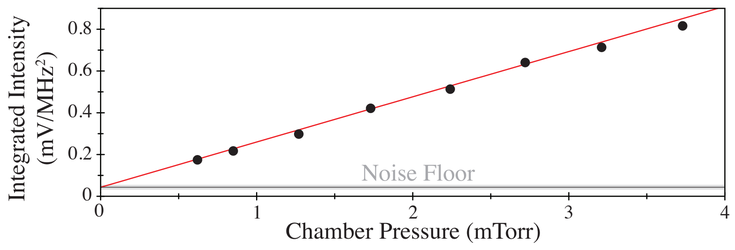

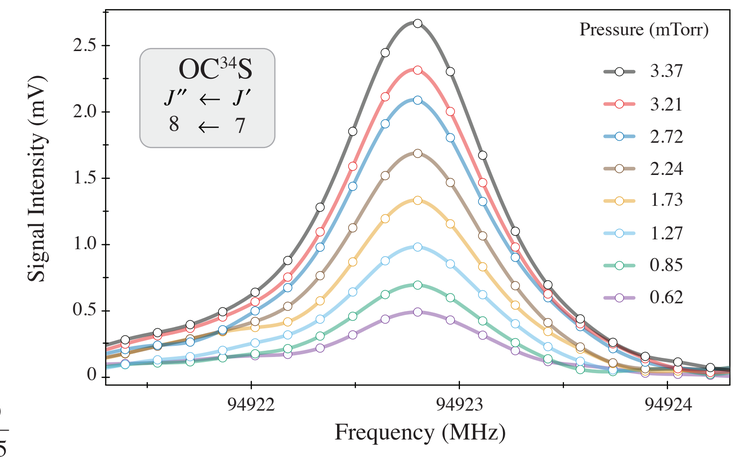

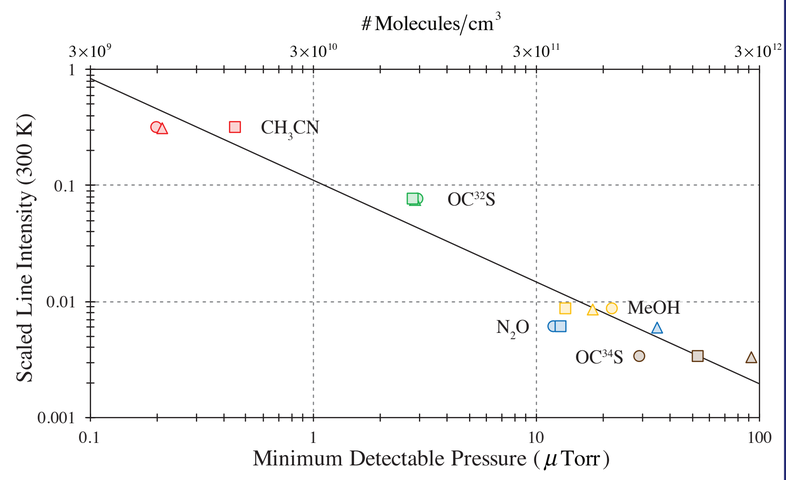

Summary and Future Engineering Goals

- A 177 -205 GHz synthesizer fabricated in 28 nm CMOS has also been developed which will be integrated into the existing PCB electronics to allow for molecular detections in the G-band.
- This multiplexed W-band/G-band system could measure H2O, HDO, and D2O allowing for in situ characterization of the isotopic content of water and ice samples.
- Future plans to add an appropriate bandwidth analog to digital converter and fast Fourier transform electronics designed to process just enough bits to capture the dynamic range of the instantaneous IF signal would allow for generation of real time frequency domain spectra.

National Aeronautics and Space Administration
Jet Propulsion Laboratory
California Institute of Technology
Pasadena, California

Poster No: T - 06

National Aeronautics and Space Administration

Optical link acquisition simulator for inter-spacecraft laser heterodyne interferometers

Author: Samuel Francis (335B)

Contributions by: Jehhal Liu (335B), Chris Woodruff (335B), Brent Ware (383H), Bob Spero (383A), Kirk McKenzie (3350) & Bill Klipstein (7090).

Optical link acquisition

Acquiring the optical link in an inter-spacecraft laser interferometer, such as the GRACE Follow-On laser ranging interferometer (LRI) or the Laser Interferometer Space Antenna (LISA), is a challenging problem with many degrees of freedom. Acquisition is vital to the success of the mission – without light, there is no science – however, since these interferometers operate over baselines greater than 200 km, it is difficult to completely test acquisition on the ground. Simulations are therefore an invaluable tool that enable us to understand all factors affecting acquisition of the optical link, allowing us to plan and test contingencies.

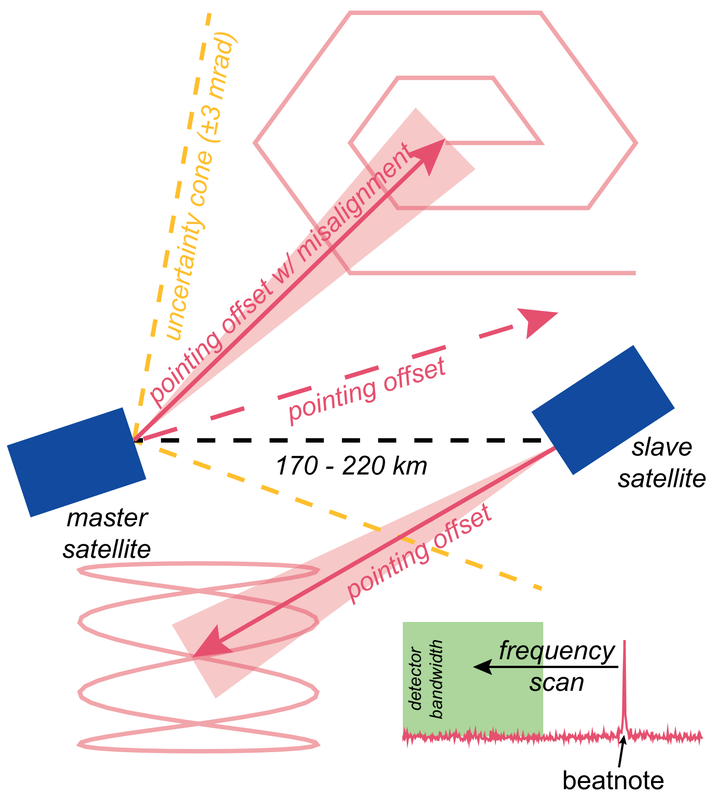

Figure 1: Optical link acquisition on GRACE Follow-On has 5 degrees of freedom. Relative pointing of the two lasers and the laser frequency offset are optimized using a number of scans.

In the two satellite GRACE Follow-On, optical link acquisition is a 9-hour scan that must resolve 5-degrees of freedom: tip and tilt of the two satellites and a frequency detuning of the lasers. During acquisition the master satellite performs a hexagonal scan while the slave performs a faster, Lissajous scan and sweeps its laser frequency. Each satellite monitors an FFT of the photodetector signal – recording scan position, laser frequency and amplitude – when a flash (a MHz heterodyne beatnote) is observed. The satellites then return to the scan positions and laser frequency at which they saw the largest beatnote, optimize the link and are then ready for science.

What can we learn?

In addition to learning the pointing and frequency offset of the optical link, acquisition can also be used to improve the signal-to-noise ratio (SNR) of the beatnote.

If the mirrors in the Triple Mirror Assembly (TMA), a segmented retroreflector, is misaligned, the beatnote SNR will drop. We can correct for a misalignment of the TMA (referred to as a co-alignment error) by adding an offset to the steering mirrors on each satellite. To do this (and to make sure we aren't making things worse) we need to measure co-alignment error to better than 10 µrad.

Our plan to measure co-alignment uses the timing of the flashes on the master and slave satellites during acquisition. A co-alignment error means the master and slave will see flashes at different times: the master satellite will be pointing at different parts of the sky when the satellites see their respective flashes. The difference in pointing can be used to estimate the co-alignment error.

National Aeronautics and Space Administration

Jet Propulsion Laboratory
California Institute of Technology
Pasadena, California

www.nasa.gov

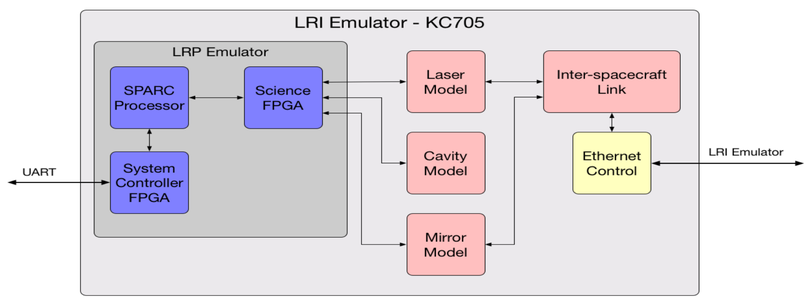

Figure 2: The "System on a chip" (SoC) simulator used to test optical link acquisition for the GRACE Follow-On LRI.

Optical link acquisition simulator

The system on a chip (SoC) is a full simulation of the GRACE Follow-On LRI that runs on a Kintex®-7 FPGA KC705 development board. Connecting two SoCs with ethernet allows a dual-satellite LRI simulation to be performed, providing a way to test optical link acquisition. Within the simulation, pointing and frequency offsets between the two satellites and co-alignment error can be changed, allowing the impact of these variables on the SNR of the acquired beatnote to be studied over many acquisition attempts.

Co-alignment error tests with the SoC

The SoC was used to investigate how accurately the Triple Mirror Assembly co-alignment error could be measured from the timing of the link acquisition data.

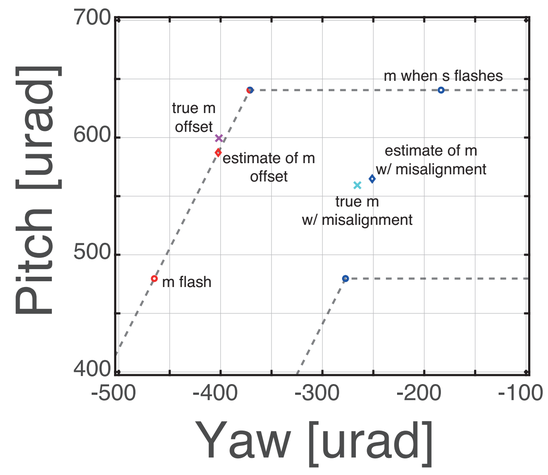

Figure 3: Co-alignment error can be inferred from acquisition using the timing of master and slave flashes.

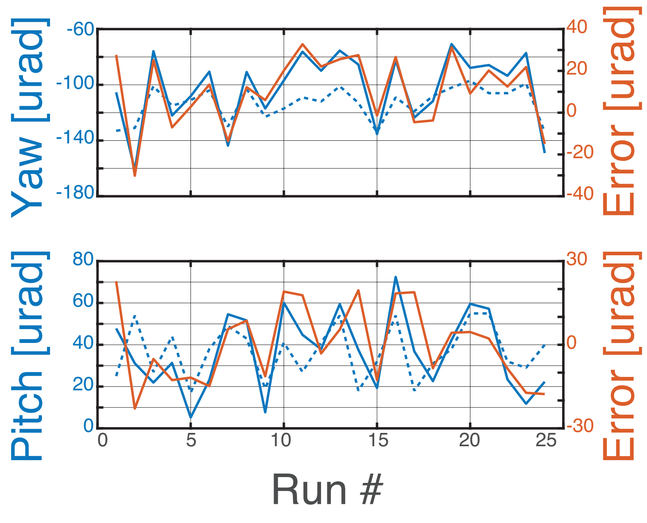

Figure 4: Co-alignment errors were measured over 24 acquisition runs on the SoC to evaluate the proposed measurement.

The error was found by comparing the size of the simulated co-alignment error with an estimate found by fitting a Gaussian to the master and slave flashes. As Figure 4 shows however, in these measurements the error has a standard deviation of 17 µrad in yaw and 14 µrad in pitch, failing to meet the 10 µrad goal.

Updating the acquisition scan

The large uncertainty was determined to be a result of the 185 µrad spacing between points in the master scan. To reduce the uncertainty in the co-alignment error estimate, the SoC simulations were repeated using the scan in Figure 5, a hexagonal scan 3 times as dense as the scan in Figure 3.

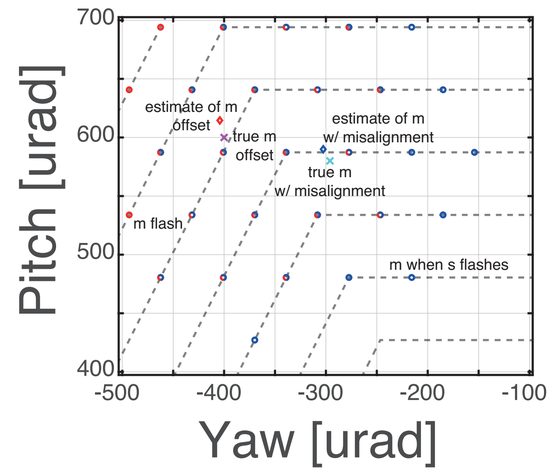

Figure 5: A denser scan could reduce the error when estimating co-alignment error from the timing of flashes.

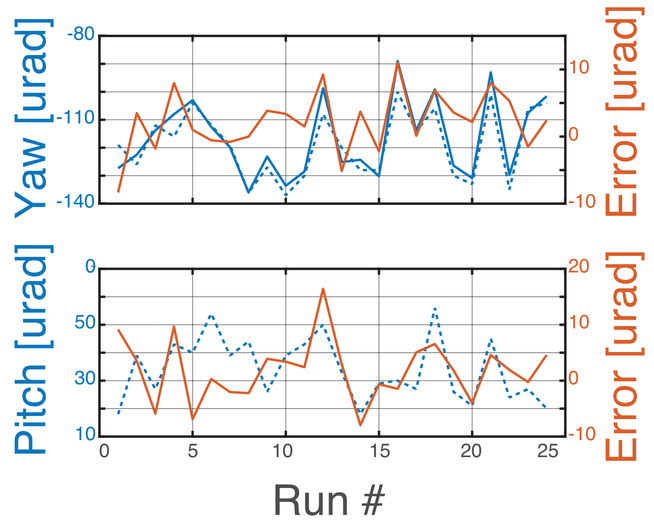

Figure 6: The uncertainty in the co-alignment estimate reduced to < 10 µrad when a denser scan was used.

The denser scan reduced the error in the co-alignment error estimate below 10 µrad: the error has a standard deviation of 4.6 µrad in yaw and 5.6 µrad in pitch.

What's next?

GRACE Follow-On is in Initial Operational Capability (IOC) right now. Optical link acquisition will be the week of July 4th. Based on these results, if the SNR after acquisition is lower than desired, the denser scan shown in Figure 5 will be used to measure the co-alignment error and then this will be applied as a correction to the steering mirror pointing.

Looking ahead, we want to build a SoC for LISA. LISA has three spacecraft separated by 5 million kms. The longer light delays (16.67 s vs. 0.67 ms) and additional laser links (6 vs.2) require a larger FPGA board and more memory to simulate. We have started looking for new hardware.

We plan to use the LISA SoC for testing the reacquisition algorithms that will optimize the optical link following acquisition. Reacquisition has not been studied for LISA but would benefit from testing as the long light travel times and slower actuation (pointing will be from spacecraft actuation rather than a steering mirror) make it sufficiently different from the GRACE Follow-On reacquisition.

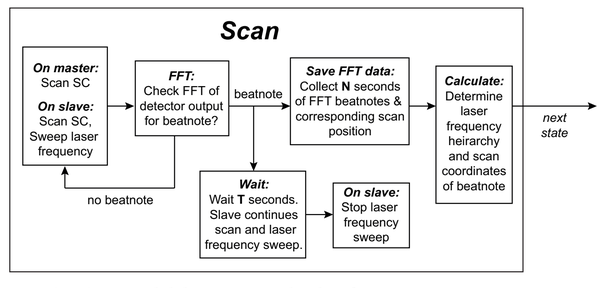

Figure 5: A SoC would be a good platform to test reacquisition algorithms for LISA.

Poster No. T-07

National Aeronautics and Space Administration

Infrasound as a Geophysical Probe for Venus

Author: Siddharth Krishnamoorthy (335)
Attila Komjathy (335) Michael T. Pauken (353) James A. Cutts (4300)

What do we know about the interior structure of Venus?

Not very much.

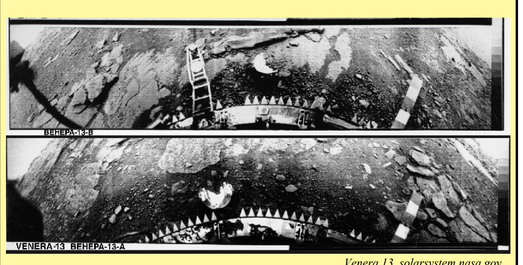

Venera 13, solarsystem.nasa.gov

- The planetary evolution and structure of Venus remain uncertain more than half a century after the first visit by a robotic spacecraft.
- Venus is very similar in size (0.95 R_{Earth}) and mass (0.82 M_{Earth}) as the Earth. Venus' extremely hot surface (>460°C surface temperature) ensures that the crust is much thinner than the Earth. The exact thickness of the crust is unknown.
- There is no evidence of Earth-like plate tectonics. However, the surface is geologically young and shows tell-tale signs of local seismic activity.
- The absence of a planetary dipolar magnetic field indicates the absence of strong convection in the mantle.
- To understand how Venus evolved, it is necessary to study its internal structure, for which it is important to investigate its seismic activity (as we have done for the Earth).

What are some ways we can study the interior structure of Venus?

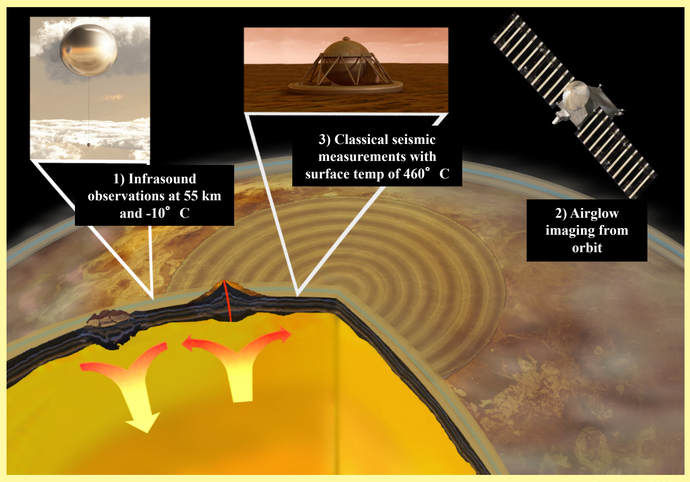

Cutts et al. (2015)

- Due to the adverse surface conditions on Venus, it is infeasible to place seismometers on the surface for an extended period of time. Therefore, seismic activity has never been measured directly on Venus.
- However, due to dynamic coupling between the solid planet and the atmosphere, atmospheric fluctuations generated by seismic activity can be detected in the atmosphere itself.
- Atmospheric fluctuations cause fluctuations in the "airglow" of Venus in the infrared, which may be imaged from orbit. This method is sensitive to strong quakes (magnitude 5 and above).
- Alternatively, atmospheric fluctuations may be intercepted by barometers on a floating balloon at approximately 55 km altitude, where the temperature and pressure are Earth-like and sensors can survive for long periods of time. This method may be sensitive to quakes of magnitude 2 and above.

What is infrasound and how can we use it on Venus?

- "Infrasound" is the term given to pressure waves with frequencies below the limit of human hearing, i.e., 20 Hz.
- Motion in the solid planet generates disturbances in the atmosphere. Volcanic eruptions can also directly deposit energy into the atmosphere.
- The infrasonic, low-frequency part of these fluctuations can travel hundreds of kilometers away from the originating event and 80-100 km in altitude with relatively little damping.
- Venus' thick atmosphere couples energy from the solid planet into the atmosphere 60 times better than the Earth – the infrasound waves are almost exact replicas of the vertical ground motion profile.
- Aside from studying seismicity, acoustic measurements from balloon platforms can also investigate Venus climatology and atmospheric dynamics.

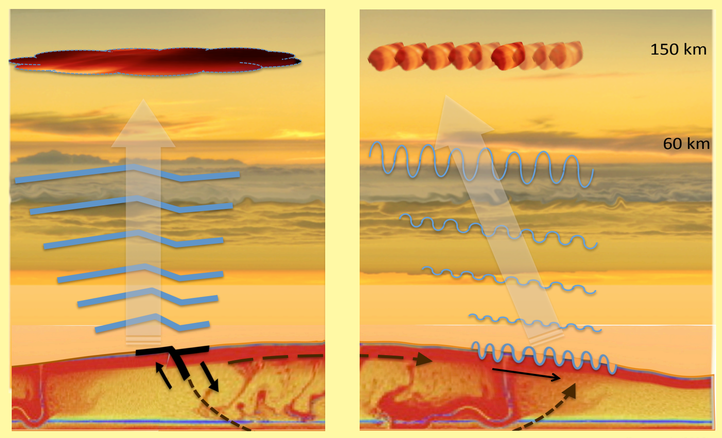

Cutts et al. (2015)

Epicentral Infrasound **Secondary Infrasound**

Have we detected quakes on Earth using infrasound?

Yes, we have. Multiple times.

- Infrasound has been detected by ground stations over 500 km away from the epicenter from earthquakes of even moderate intensity (magnitude 4.5).
- **Earthquake infrasound had never been detected from a balloon platform.** In June 2017, we conducted an experiment in Pahrump, NV, where we generated earthquakes by striking the ground with a 13 ton "seismic hammer" and detected the infrasonic pressure waves generated by the vibration of the ground from barometers on a balloon approximately 300 m away.

13 metric ton "seismic hammer" struck the ground repeatedly

Ground-based and moored balloon-based (aerostat) barometers detected pressure changes

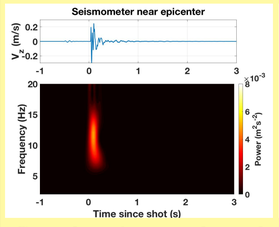

Ground motion was detected by seismometers near the hammer.

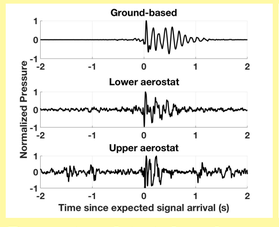

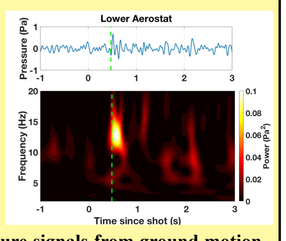

Barometers detected weak pressure signals from ground motion and reproduced its infrasonic frequency content. The left plot shows stack of multiple shots for three different barometers, the right plot shows the pressure trace and spectrogram for a single representative shot detected by the lower aerostat barometer.

What about volcanic eruptions?

- Infrasound has been detected from volcanic eruptions by nearby ground stations and also aerostat-based barometers.
- We mimic the detection of infrasound from volcanoes in a much more cost-effective way – we detect infrasound from rocket launches from Vandenberg Air Force Base – that's a free "volcanic explosion" once a month.
- The infrasonic signature of rocket launches is remarkably similar to gas jets in volcanic plumes. We have been able to detect these signatures from over 200 km away for 7 launches since November 2017 (including the InSight launch on May 5, 2018).
- These data will help us study volcanic signatures and also develop source strength and location inversion techniques.

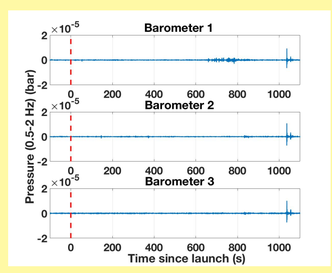

InSight launch, May 5, 2018

Falcon 9 launch, Dec. 22, 2017

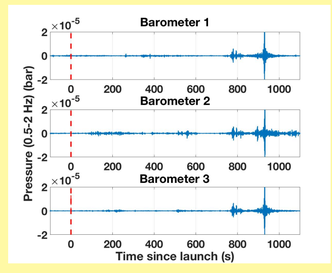

Falcon 9 launch, Dec. 22, 2017

Where do we go from here?

To Venus, via Sweden, Nevada, and Oklahoma.

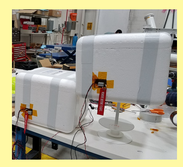

The Payload for Infrasound Measurement in the Arctic (PIMA) will fly as a secondary payload on the PMC-Turbo balloon flight from **Sweden** to Canada in June 2018 at an average altitude of 130,000 feet. This experiment will measure the stratospheric infrasonic background and will be the first test of our sensors in a stratospheric environment.

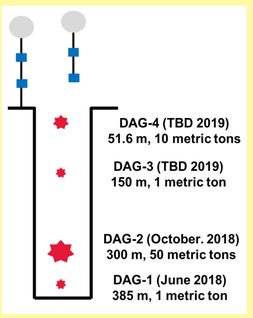

We will deploy an aerostat and a free-floating balloon with two barometers on a tether over sub-surface explosions in **Nevada** as part of the 2018-19 Dry Alluvium Geology (DAG) experiment. The energy released by these explosions is much larger than the seismic hammer and infrasound detection will be attempted from over a mile away.

Oklahoma has the largest concentration of earthquakes in the continental United States. On average, there is a magnitude 3 earthquake in Oklahoma everyday. We aim to fly a loitering balloon over Oklahoma to detect naturally occurring earthquakes in the stratosphere. This will be the closest Earth analog to Venus and a first of its kind experiment.

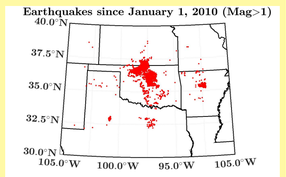

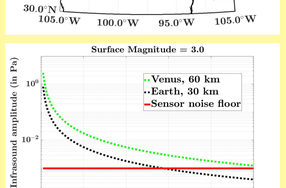

It's time to unveil Venus.

Key Takeaways

- **Venus' surface is too hot for electronics to last long enough to study its seismicity and internal structure.**
- **Seismic events create pressure disturbances that can be measured from balloons floating in a cooler Venus environment.**
- **We can answer a lot about Venus' interior without needing to land on it.**

National Aeronautics and Space Administration

Jet Propulsion Laboratory
California Institute of Technology
Pasadena, California

www.nasa.gov

The authors would like to acknowledge the Strategic R&TD Program at JPL for funding this research.

Poster No. T-08

National Aeronautics and Space Administration

Kalman filtering as a novel approach to determine celestial reference frames

B. Soja[1], H. Krasna[2,3], J. Böhm[2], C. Jacobs[1], R. Gross[1]

Contact:
Benedikt Soja
bsoja@jpl.nasa.gov
@b_soja

1. Jet Propulsion Laboratory, Section 335, California Institute of Technology 2. Technische Universität Wien 3. Astronomical Institute, Czech Academy of Sciences

Celestial reference frames

CRF
↓ defined by
coordinates of extra-galactic radio sources
↓ as observed by
Very Long Baseline Interferometry (VLBI)

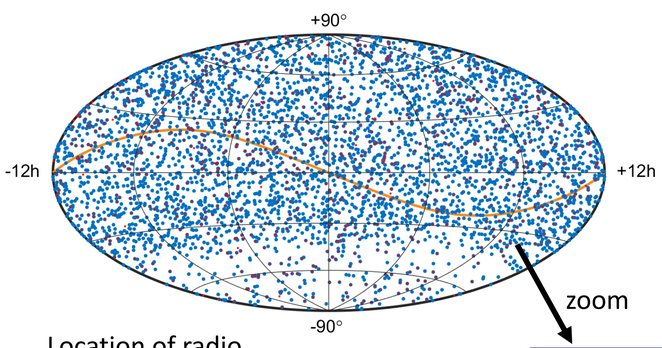

Location of radio sources used in this study

zoom

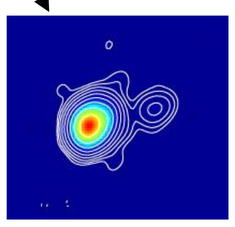

Image of radio source 4C 39.25
vlbi.obs.u-bordeaux1.fr

VLBI telescope, nrao.edu

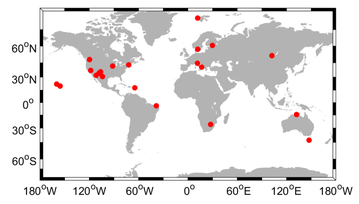

Location of VLBI telescopes used in this study

Accurate CRFs are needed for the navigation of NASA's spacecraft
(and for several other applications in astronomy & space sciences)

Problem of current CRFs

Assumption of constant radio source coordinates – in reality, radio sources are not point-like, but exhibit structure and changes therein

Solution

CRF defined by coordinate time series from Kalman filtering – to take into account variability in radio source coordinates

Computation of CRFs

First step: computation of a CRF using all observed radio sources

Constant CRF
- Least-squares adjustment
- Input: single session VLBI data
- 4097 radio sources

Most radio sources have been observed less than five times → constant model computationally very efficient

Second step: computation of a CRF from well-observed sources

Kalman filter CRF
- Kalman filter
- Input: residuals based on constant CRF
- 822 radio sources

Irregular behavior of radio source coordinates (e.g., due to source structure) → Kalman filter time series able to capture these non-linear effects

All computations based on VLBI data: Time frame: 1980 – 2016.5
Number of sessions: 5446

Kalman filter setup

Kalman filter & smoother for radio source positions
Refined stochastic model taking into account:

Source-dependent process noise

obtained from the Allan deviation of radio source coordinate time series

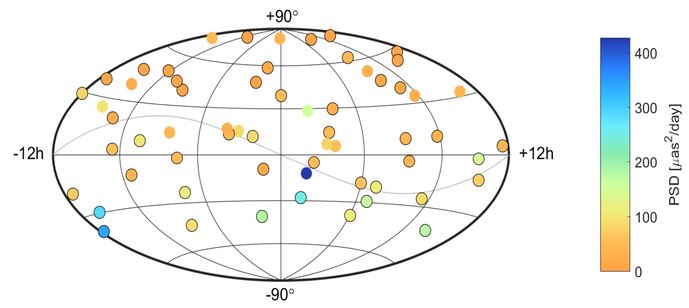

Jet directions

obtained from radio source images. Usually, there is higher variability along the jet. The process noise is scaled accordingly.

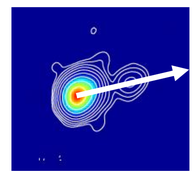

Results: CRF solution examples

0119+115
ICRF2 defining source

4C 39.25
ICRF2 special handling source

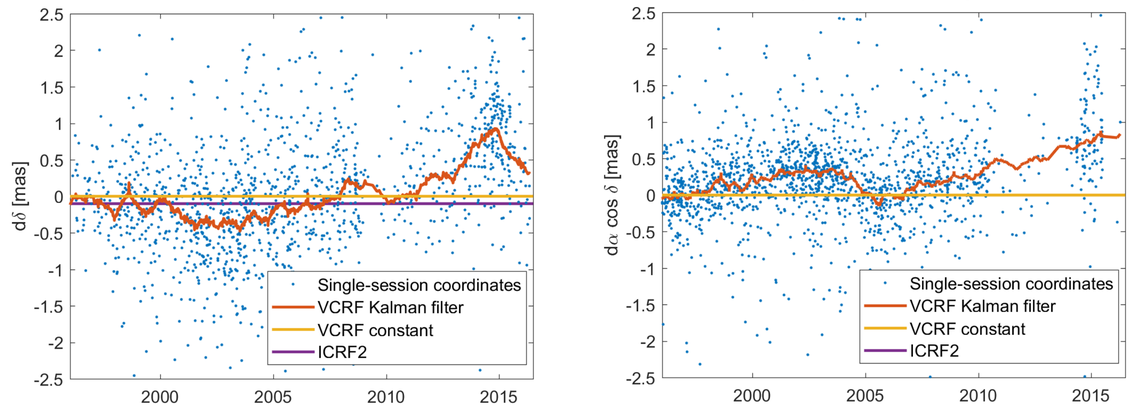

Kalman filter CRF (red) tracks irregular coordinate variations in the observed VLBI coordinates (blue) unlike the constant frame (yellow)

CRF solution evaluation

Source coordinate offsets estimated in VLBI analysis with respect to a priori CRFs

Improvement when using Kalman filter →

WRMS [μas]	RA cos(DE)	DE	2D
CRF constant	429	576	728
CRF Kalman filter	336	470	586
Δ(KF – constant)	-22%	-18%	-20%

Conclusions

- **Successful determination** of a **Kalman filter CRF**: time series radio source coordinates take into account **irregular coordinate variations**, e.g. due to changes in **source structure**
- Kalman filter CRF is consistent with a **complete constant** CRF
- **Performance in VLBI analysis:** estimated coordinate offsets **improved by 20%** when using Kalman filter CRF

National Aeronautics and Space Administration
Jet Propulsion Laboratory
California Institute of Technology
Pasadena, California

www.nasa.gov

Poster No. T-09

Mineral and Organic Characterization with an Instrument Payload on the LEMUR Rock-Climbing Robot

Author: Kyle Uckert (347C)
Aaron Parness (347M), Rohit Bhartia (3225), David Flannery (3225)

Introduction:

Planetary caves are desirable destinations for future robotic astrobiology investigations. A rock-climbing robot equipped with an instrument payload designed to identify biosignatures and characterize subsurface mineralogy is ideally suited to explore these extreme environments.

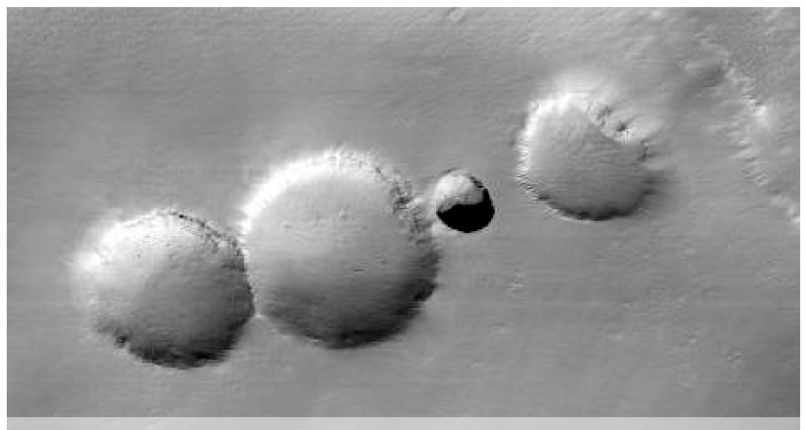

THEMIS image of a skylight exposed by a crater chain (Arsia Mons)

Objectives:

- Develop a suite of instruments to detect biosignatures in extreme, extraterrestrial environments.
- Define field operation procedures to autonomously and rapidly identify biosignature candidates while minimizing data acquisition time.
- Characterize the mineralogy and spatial distribution of organics associated with biovermiculation patterns and stromatolites *in situ*.

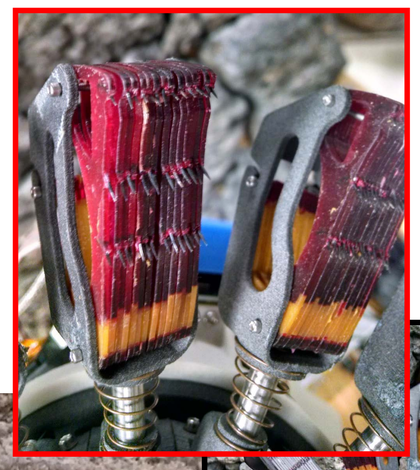

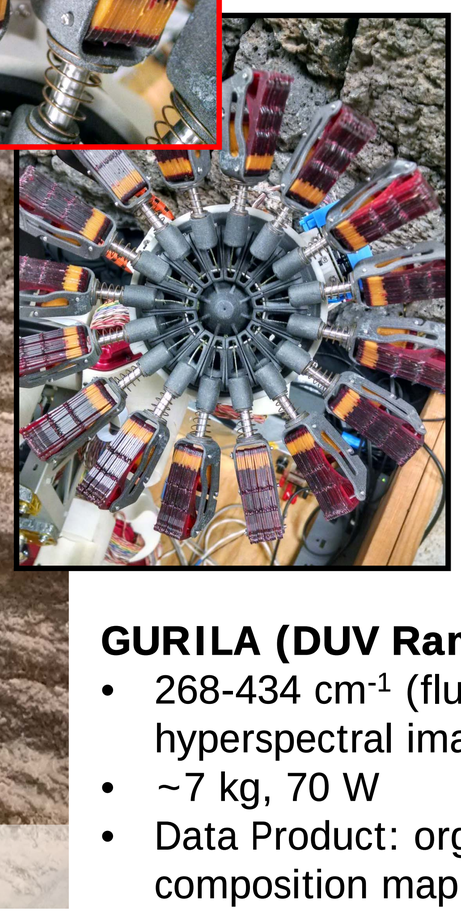

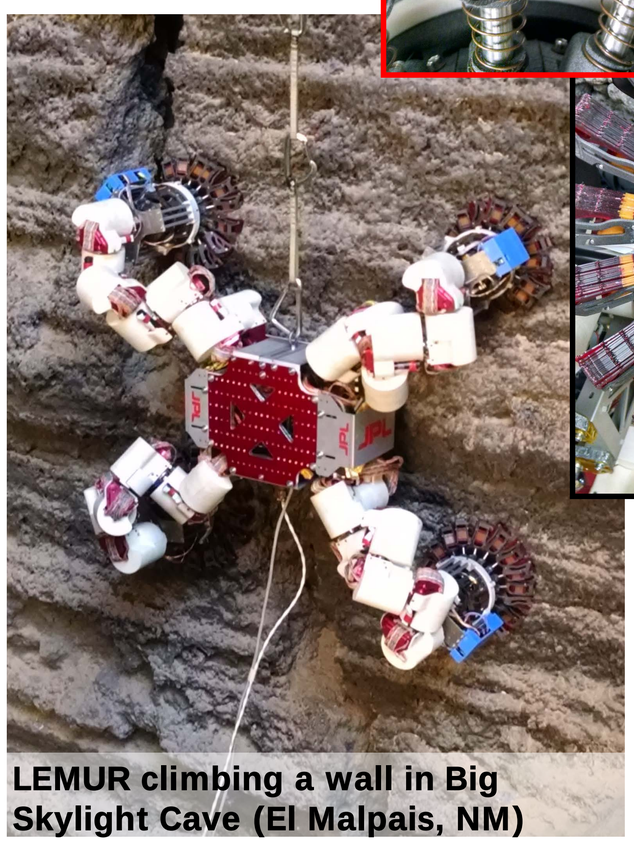

LEMUR climbing a wall in Big Skylight Cave (El Malpais, NM)

Field Operations:

- Develop a focus map (right) of an unprepared target from a stack of context camera images.

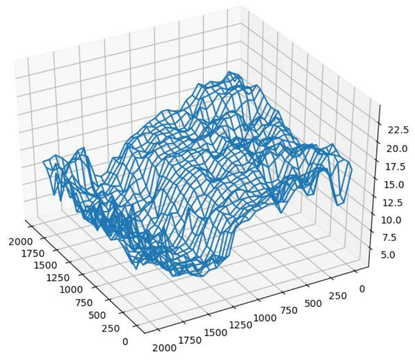

- Autonomously identify regions-of-interest (ROI) for detailed follow-up measurements based on rapid, low-resolution fluorescence scans.

LEMUR (robotic platform):

- Climbs varied, uneven, rocky surfaces autonomously using LIDAR point cloud data inputs.
- Anchors itself to surfaces with hundreds of sharp microspines
- Fielded on basalt (El Malpais lava tubes, Pisgah crater) and granite (Granite Mountain Range).

PASA (NIR Spectrometer):

- 1.6-3.6 µm point spectra
- ~1 kg optical head, 30 W
- Data Product: mineralogy

GURILA (DUV Raman/Fluorescence Spectrometer:

- 268-434 cm^{-1} (fluorescence) 500-4000 cm^{-1} (Raman) hyperspectral images (2x2 cm, 100 µm resolution)
- ~7 kg, 70 W
- Data Product: organic and major mineralogical composition map

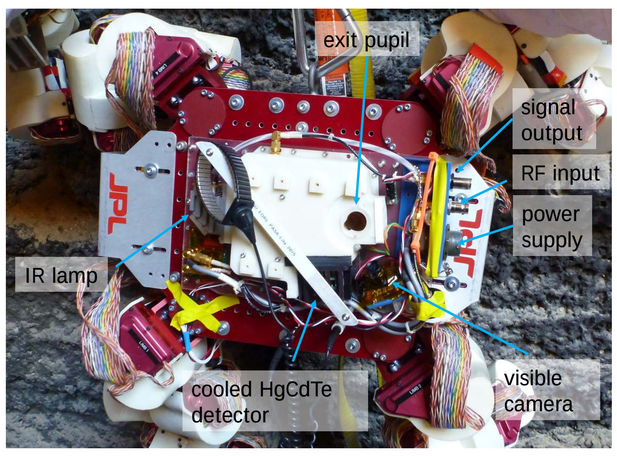

APE (XRF Spectrometer):

- 0-25 keV XRF hyperspectral image (2x2 cm, 100 µm resolution)
- ~1 kg, 4 W
- Data Product: elemental composition map

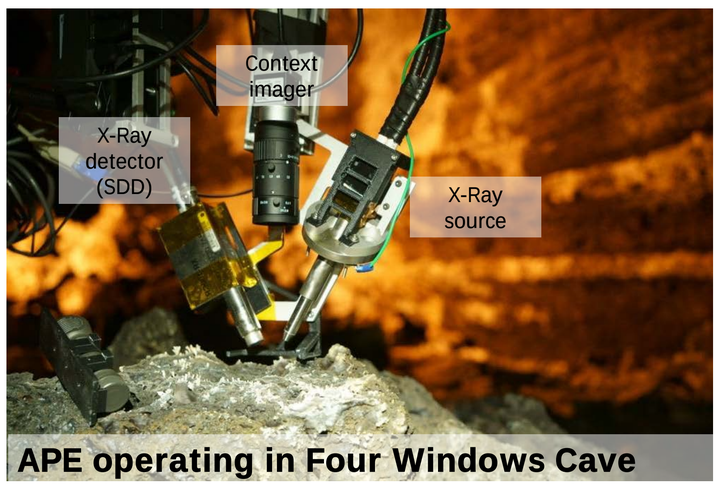

APE operating in Four Windows Cave

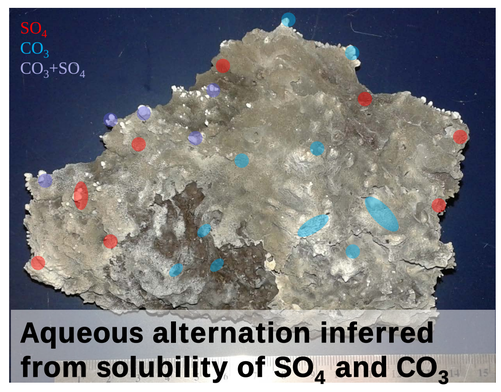

Aqueous alternation inferred from solubility of SO_4 and CO_3

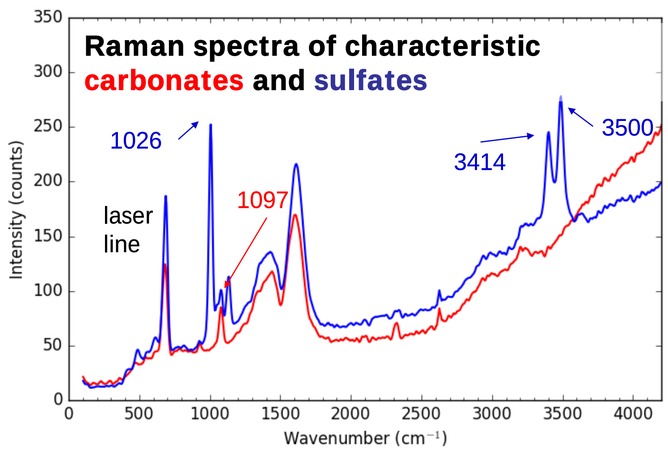

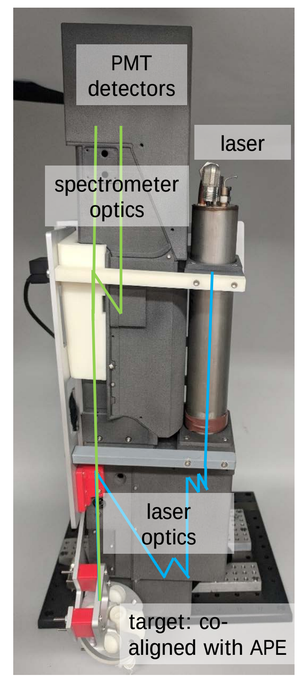

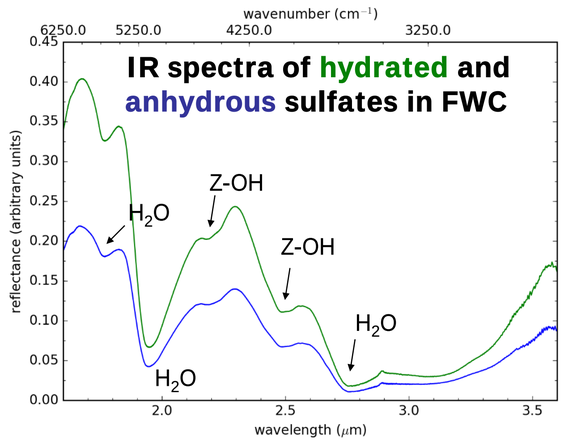

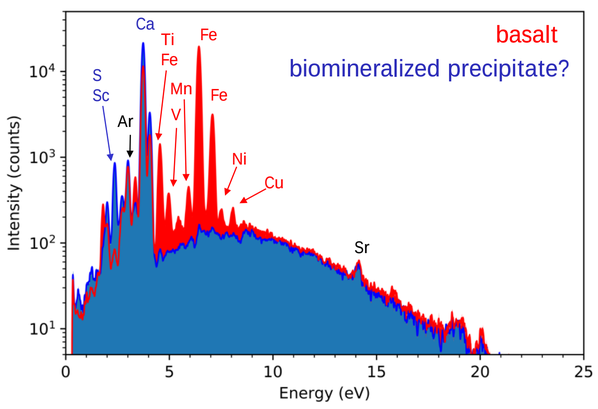

Conclusions:

- Measurements of astrobiologically relevant targets with the LEMUR instrument payload reveal:
  - Aqueous alteration history
  - Trace elements
  - Organic and mineralogical composition
- Autonomous ROI selection reduces data acquisition time in the field

Poster No. T-11

National Aeronautics and Space Administration
Jet Propulsion Laboratory
California Institute of Technology
Pasadena, California

www.nasa.gov

National Aeronautics and Space Administration

Driving Energy Estimation for Mars Rovers
Using a Newly Developed Single Wheel Testbed

Author: Shoya Higa (347), Masahiro Ono (347)

HIGHLIGHT:

- Developed the new single wheel testbed to acquire the wheel-terrain interaction data under controlled environment
- Allows single-wheel test both indoor and outdoor

MOTIVATION:

- Future Mars rover missions require energy-optimal navigation.
- For energy-constrained missions, path planning that accurately predict energy consumption before the rover travels is essential.
- To develop energy consumption model of rovers' mobility, collecting motor current with wheel-terrain interaction is required.

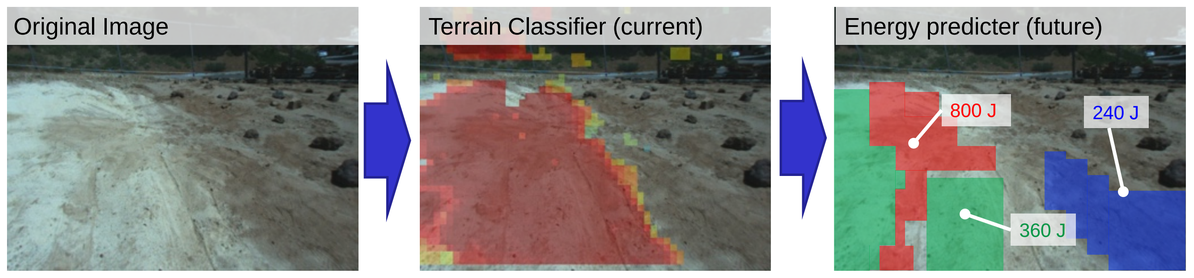

GOAL OF THIS RESEARCH:

- Set up testbed and collect data needed for driving energy estimation

Control variables:
- Wheel speed
- Wheel load
- Slip ratio
- Traction drag

Measurements:
- Slip/Sinkage
- Motor current
- Force/Torque

FEATURES:

- Operates both indoor and outdoor environments
- Drives with free- or forced-slip conditions
- Takes additional weights to simulate arbitrary wheel load
- Operates with CLARAty and ROS

EXPERIMENTAL SETUP:

- Target terrain: rock plate, flat sand, two rough sand terrains
- Test wheel: Athena rover's wheel
- Wheel diameter: 20 cm, Wheel width: 12.3 cm
- Wheel speed: 3 cm/s , Wheel load: ~18 N

Flat sand

Rough sand (a)

Rock plates

Rough sand (b)

PROCEDURE:

1. Place the portable single wheel testbed on a target terrain
2. Run the testbed 1 m and measure wheel current with wheel-terrain interaction data

RESULTS:

- Detected current oscillations due to wheel surface geometry (lugs) when driving on firm sand or rock plate
- Detected significant difference in current profiles between different terrain types
- Further data collection is needed to collect sufficient data for training machine learning model

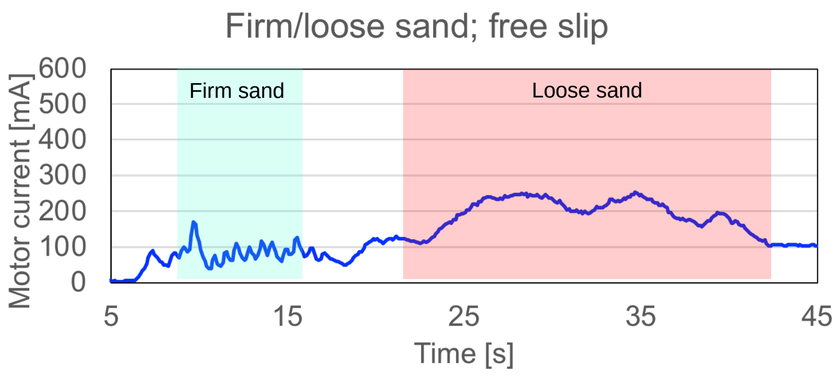

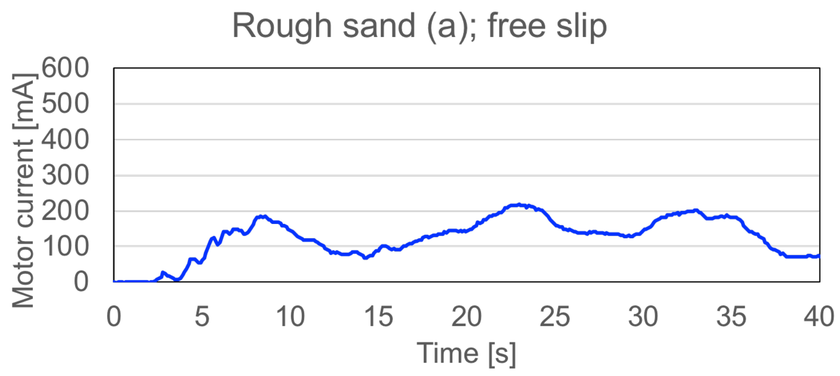

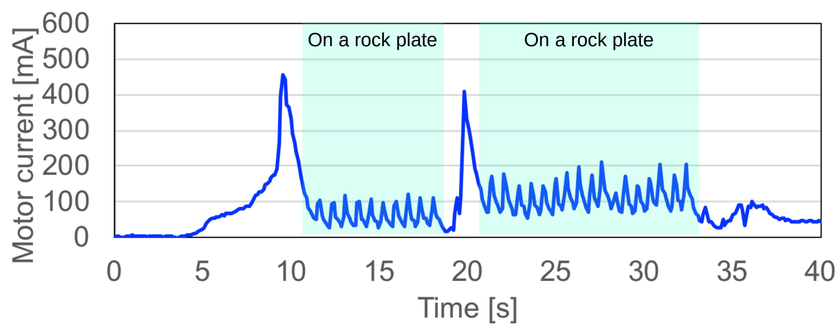

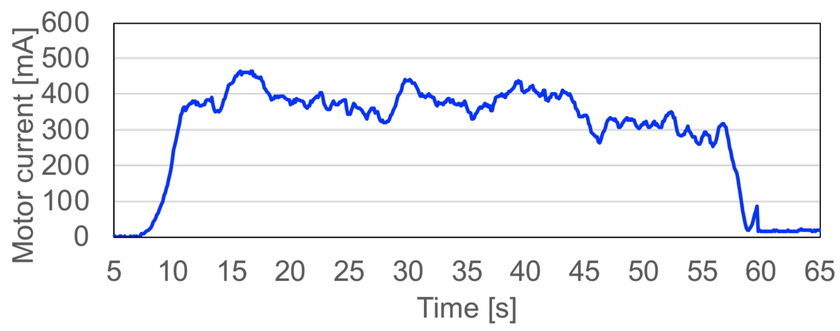

FUTURE PROSPECTS:

- Acquire wheel current data on various terrains by single-wheel test
- Develop an energy model of a wheel based on current measurements

National Aeronautics and Space Administration

Jet Propulsion Laboratory
California Institute of Technology
Pasadena, California

www.nasa.gov

Poster No. T-13

National Aeronautics and Space Administration

Infusion of CMOS for Radar and Spectroscopy

Author: Yanghyo (Rod) Kim (386-A)
Adrian Tang (386-A), Theodore Reck (386-A)

Advent of CMOS Technology

CMOS Technology Evolution

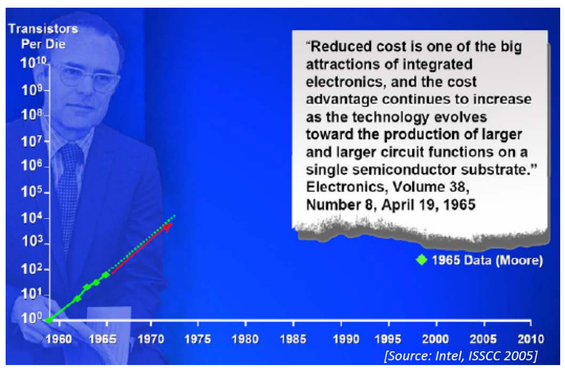

- 5 decade long Moore's law
- Device scaling and integration
- Explosion of consumer electronics

Nano-Scale Device

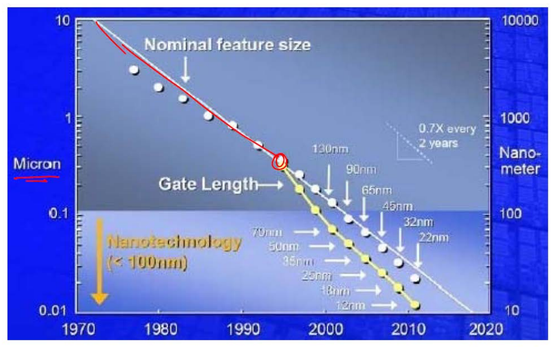

- Industry main stream: < 28nm
- 7nm in production
- 65nm available at reasonable cost

CMOS Device Performance

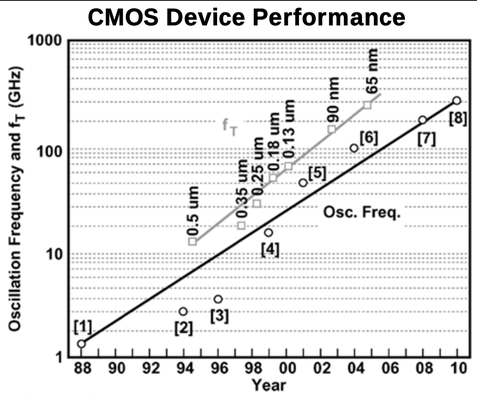

- f_t, f_{max} of 65nm exceeding 200GHz
- Avenue to mm-wave amps, synth, etc

Standard Logic

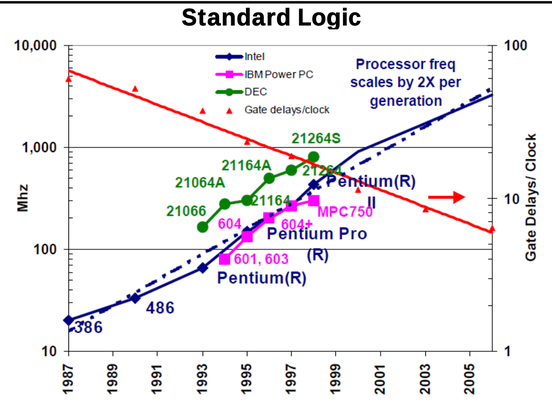

- Reduced unit gate delays per clock
- Avenue to high-speed DDS, AWG, etc

Major Benefits to NASA Instruments: Size, Weight, and Power (SWAP)

6GS/s 4K Point CMOS Spectrometer Processor

Instrument Objective & System Simulation

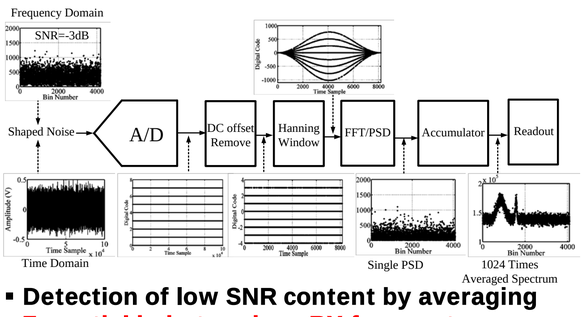

- Detection of low SNR content by averaging
- Essential in heterodyne RX for spectroscopy

System Block Diagram

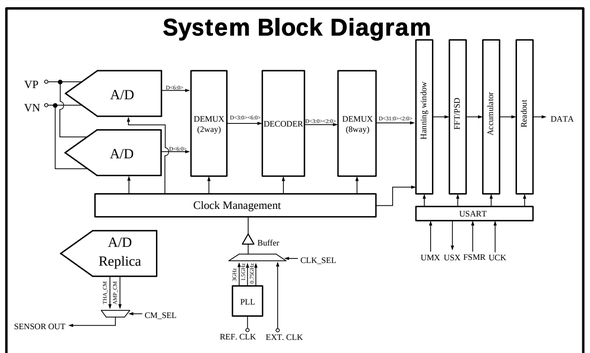

- Interleave two of 3GS/s ADC for 6GS/s
- ADC replica for bias calibration
- DEMUX and RETIME for timing requirement
- On-chip FFT/PSD/Accumulator (SRAM)
- On-chip PLL for clock generation
- Integrate all to replace power hungry FPGA

Analog Core Design

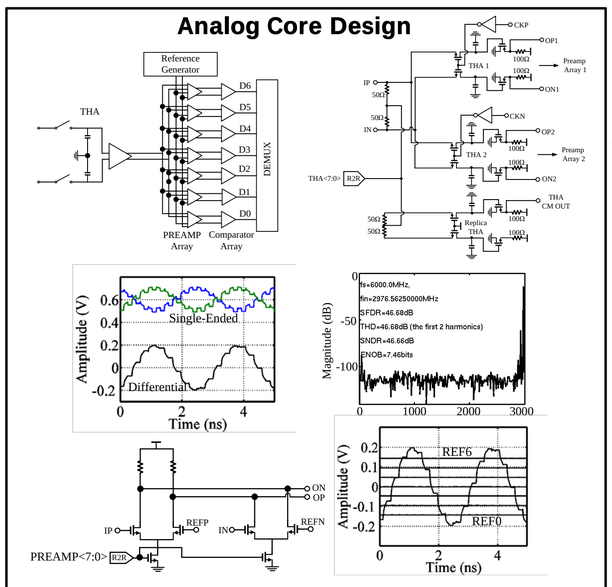

- 3-bit Flash ADC for simple and fast design
- Differential signaling to cancel clock feed

Data Flow and Clock Calibration

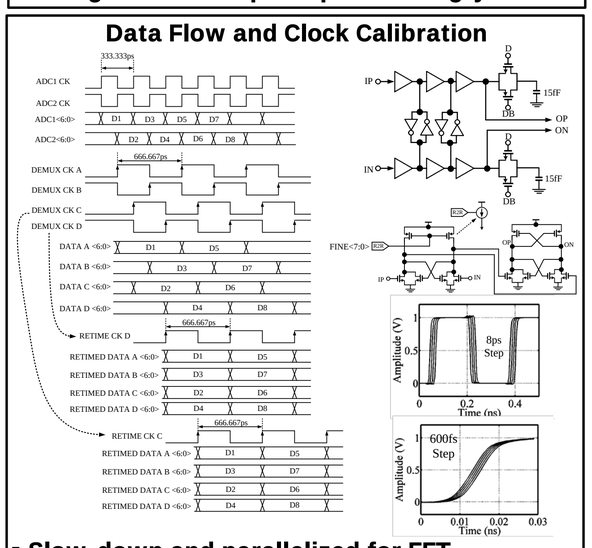

- Slow-down and parallelized for FFT
- Coarse and fine tuner for DEMUX/RETIME

Programmable Reference Generator

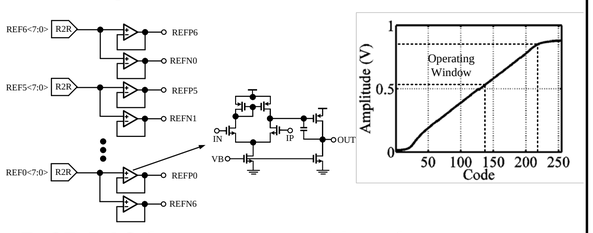

- R-2R DAC for programmable reference
- Interleaved channel mismatch calibration

Implementation

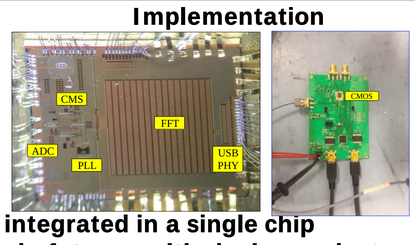

- All integrated in a single chip
- Key in future multi-pixel array instrument

Measurement

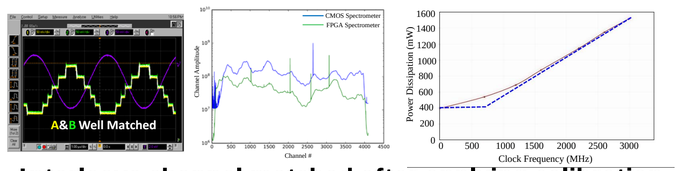

- Interleave channel matched after applying calibration
- 1.5W power vs. 50W FPGA spectrometer

Ku-Band CMOS FMCW Radar for Snowpack Remote Sensing

Science Objective

- Drastic snowpack retreat in Sierra
- 60% of California water supply
- Need for accurate SWE estimates
- Snow cover, depth, density
- This work: Radar for dry-snow depth

Existing Snow Sensing

	Microwave	IR	Optical
Snow Cover Estimate	Reasonable	Excellent	Excellent
Snow Depth Estimate	40 % Error	N/A	N/A
Attainable Resolution	25 km	100 m	10 m
Snow Density Estimate	>20 % Error	N/A	N/A

New Approach:
- Design low-power/volume CMOS radar
- Fly over mountain on small air-craft

Dry-Snow Property

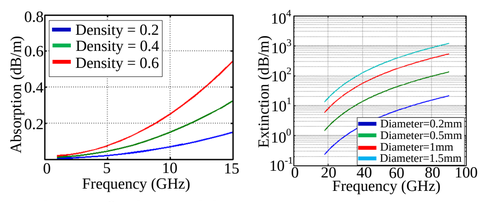

- Consists of air and ice
- Absorption dominates below 15GHz
- Scattering dominates beyond Ku-band
- Select Ku-band for dry-snow depth

System Considerations

Parameters	Values
Antenna Size (A)	30 cm (aircraft payload)
Transmit Power (Pt)	0.5 W (available hardware)
RX Noise Figure (NF)	7 dB
Bandwidth (B)	2 GHz (from resolution)

Parameters	Values
Range/Altitude (R)	100 m (avoid trees)
Scatter Coefficient (σ)	-12 dB (worst case)
Temperature (T)	250 K (worst case)
Snow Losses (S)	10 dB (from study)

System Simulation

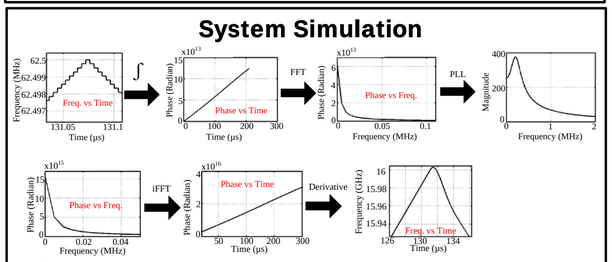

- Proves direct-chirp generation

Implementation

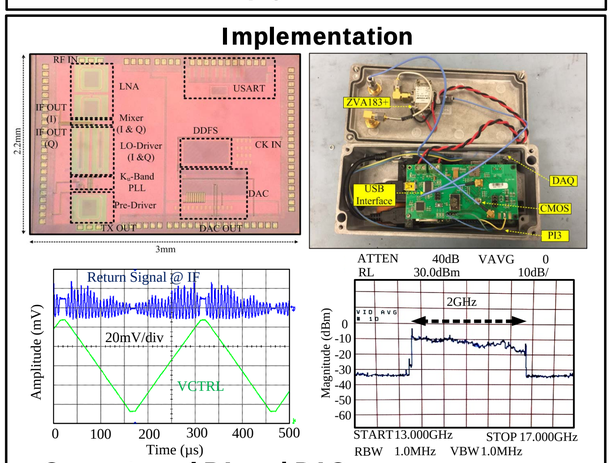

- One external PA and DAQ
- Measurement confirms
- CMOS TRX Power Consumption: 252mW

System Block Diagram

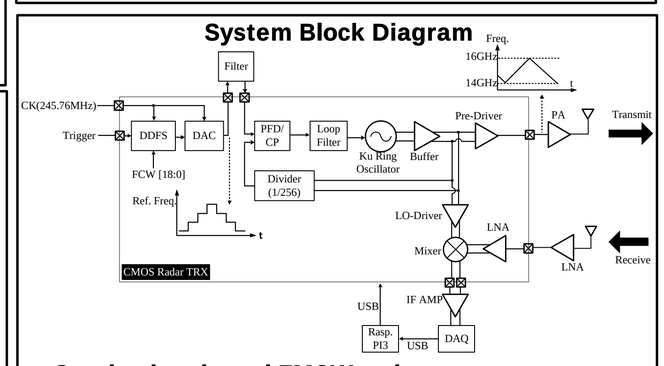

- Synthesizer based FMCW radar
- Ring-VCO: Wideband chirp (2GHz)
- Integrated DDS, DAC, PLL, TX, RX, Mixer

Mammoth Mountain Deployment

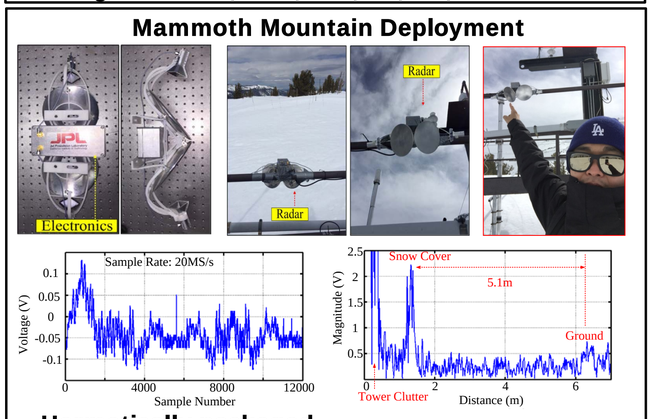

- Hermetically packaged
- Successful snow depth detection

183 GHz CMOS Heterodyne Receiver

Instrument Objective &System Block Diagram

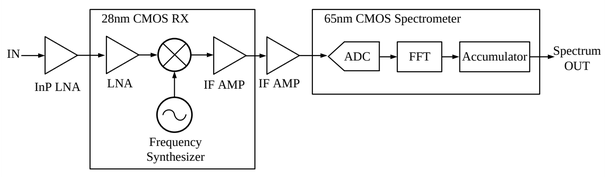

- Detect 183GHz water vapor absorption line
- Integrate LNA, Mixer, 183GHz Synth, IF Amp
- Pair with external 183GHz LNA
- Pair with developed CMOS spectrometer

Implementation

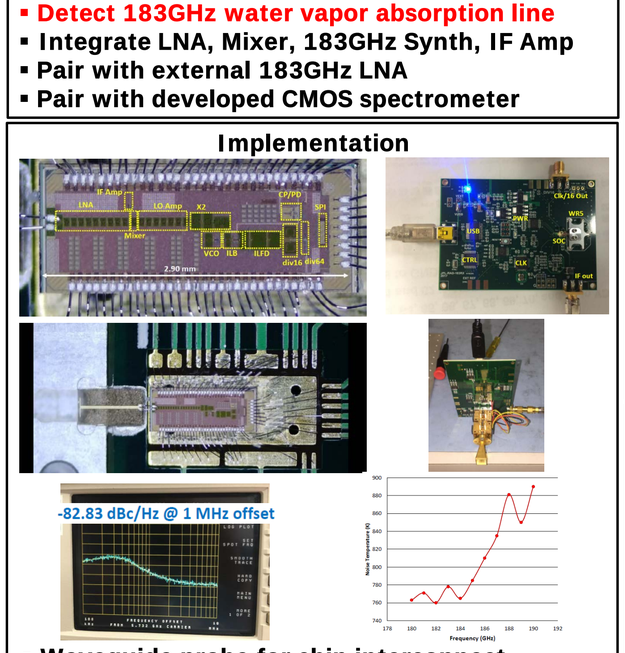

- Waveguide probe for chip interconnect
- Requires one external LNA

183GHz CMOS Synthesizer Design

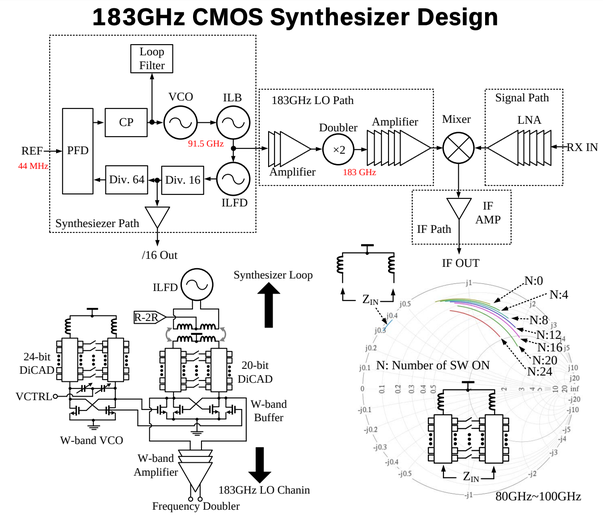

- Design W-band synthesizer
- Digitally controlled frequency tuning strips
- On-chip doubler and 183GHz amp for LO

Measurement

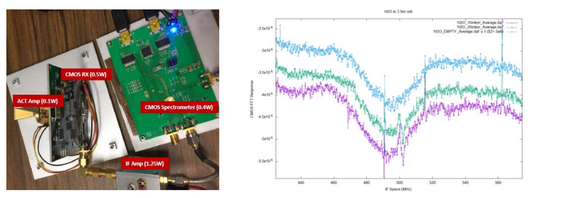

- CMOS RX consumes ~0.5W power
- Water line detected by frequency switch method

List of Related Publications

- Y. Kim, et. al. "A Ku-Band CMOS FMCW Radar Transceiver for Snowpack Remote Sensing," IEEE TMTT, 2018
- Y. Kim, et. al. "A Ku-Band CMOS FMCW Radar Transceiver with Ring Oscillaotor Based Waveform Generation for Snowpack Remote Sensing," IMS2017
- Y. Kim, et. al. "A 1.5 W 3 GHz Back-End Processor in 65nm CMOS for Sub-millimeter-wave Heterodyne Receiver Arrays," IEEE ISSTT, 2018
- Y. Zhang, Y. Kim, et. al. "A 2.6GS/s Spectrometer System in 65nm CMOS for Spaceborne Telescopic Sensing," IEEE ISCAS, 2018
- A. Tang, Y. Kim, et. al. "Evaluation of 28nm CMOS Receivers at 183GHz for Space-borne Atmospheric Remote Sensing," IEEE MWCL, 2017
- 1st Author Journal in Progress: 183GHz Integrated CMOS Receiver with Spectrometer Processor for Water Vapor Spectroscopy

National Aeronautics and Space Administration

Jet Propulsion Laboratory
California Institute of Technology
Pasadena, California

www.nasa.gov

Poster No. T-14

National Aeronautics and Space Administration

Low-loss Silicon MEMS Phase Shifter Operating at 550 GHz

Author: Sofia Rahiminejad (386)

M. Alonso del Pino (386), C. Jung-Kubiak (389), G. Chattopadhyay (386), T. Reck (386)

Background

Today mapping is done by re-orientation of the space craft or mechanical scanning

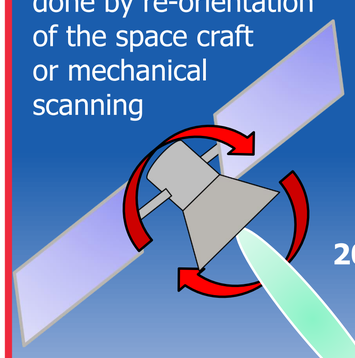

Unfortunately:
Todays phase shifters cannot operate above **200 GHz**. High resolution mapping needs higher frequencies.

Proposed solution:
An array antenna using phase shifters to electronically steer the beam

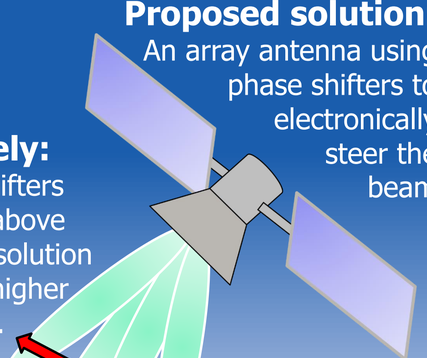

JPL wants to be able to study:
- Atmospheric compositions
- Surface properties of cold bodies

Objective

Design and fabricate a Si MEMS phase shifter

- **Operating between 500-600 GHz.**
- **Achieve phase shifts between 0°-180°.**
- **Low loss i.e. S11 <-20 dB.**
- **Fabricate the MEMS phase shifter with Si micromachining.**
- **Achieve different permittivities in the Si by introducing a periodic hole pattern, thus achieving the desired phase shift.**

Accomplishments

- **Two phase shifters were designed**
  - **One 180° Phase shifter**
  - **One 2x90° Phase shifter**
- **Both phase shifters have a span of 180° phase shift.**
- **The reflection coefficient (S11) is below -20 dB between 500-600 GHz.**
  - **For all poistions of the Si slabs.**
- **A Si micromachining process plan is presented.**
- **The permittivity of the Si slab is changed by introducing a periodic hexagonal hole pattern.**

Design

By moving the Silicon arms into the waveguide, different phase shifts occurs depending on the position.

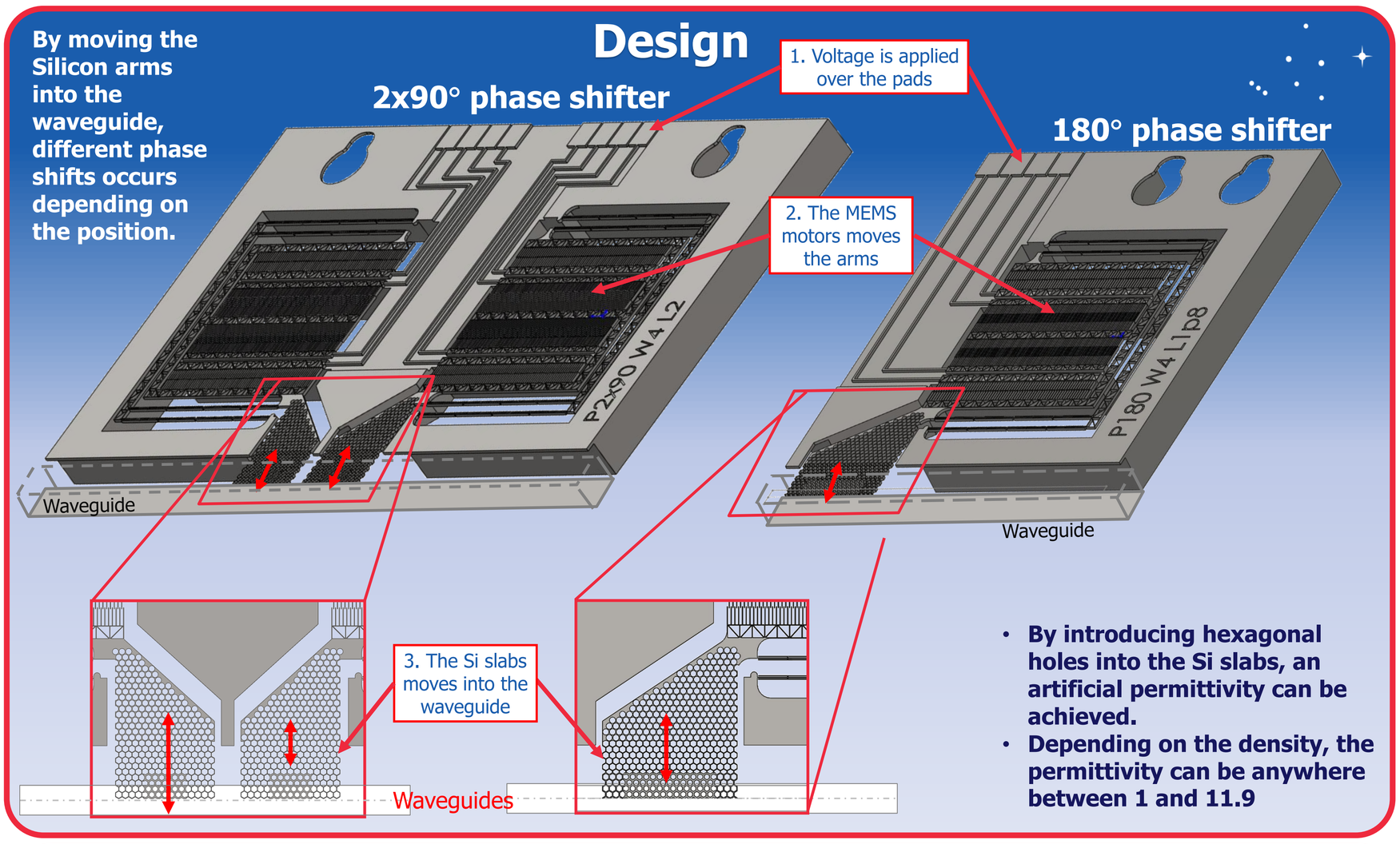

- **By introducing hexagonal holes into the Si slabs, an artificial permittivity can be achieved.**
- **Depending on the density, the permittivity can be anywhere between 1 and 11.9**

Process plan

1. **An oxidized 4" SOI (Silicon on Insulator) wafer is used. The "insulator" in this case SiO_2 is used as an etch stop.**

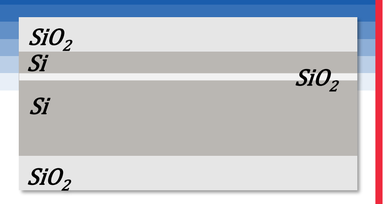

2. **The top SiO_2 is patterned with photoresist (PR) and etched with Inductive Coupled Plasma (ICP). The patterned SiO_2 acts as a hard mask.**

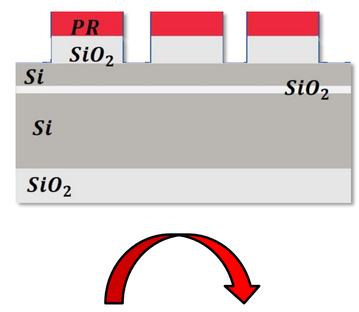

3. **The wafer is flipped and the backside is patterned in the same way as in step 2.**

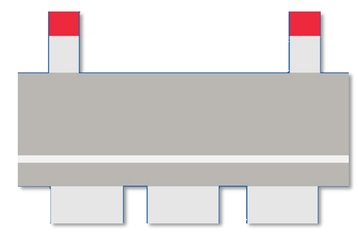

4. **The backside Si is etched with an optimized Bosch process (alternating SF_6 and C_4F_8 plasma exposure).**

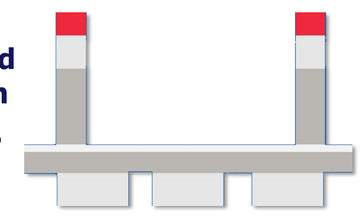

5. **The wafer is flipped back and the front is etched in the same way as in step 4.**

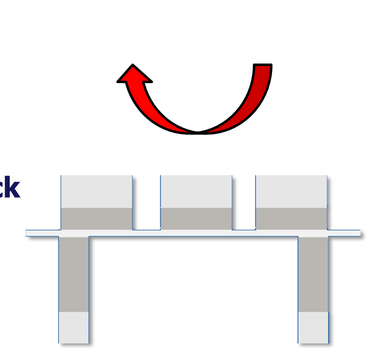

6. **The SiO_2 is removed with ICP and left is the MEMS phase shifter.**

Performance

Four cases of interest. A and B are each, one 90° Si slab.

2x90° phase shifter

The reflection coefficient S11 for the four cases.

180° phase shifter

The reflection coefficient S11 for when:
- the Si slab is completely out of the waveguide (red)
- the Si slab is completely inside the waveguide (blue)

Phase shift depending on how much the Si slabs are inserted into the waveguide

SEM image of the MEMS motor and Si slabs

Poster No. T15

National Aeronautics and Space Administration

Jet Propulsion Laboratory
California Institute of Technology
Pasadena, California

www.nasa.gov

National Aeronautics and Space Administration

Differential Absorption Radar near 170 GHz for Remote Sensing of Boundary Layer Water Vapor

Author: Richard Roy (386A-Affiliate)
Coauthors: Ken Cooper (386A), Matt Lebsock (329J)

Introduction

Problem: Passive humidity sounding instruments have limited ability to perform high-resolution, unbiased measurements of vertical water vapor profiles in the presence of clouds. This deficiency in the existing network of remote sensing satellites constitutes an important gap to be addressed by new technologies, with impacts on both numerical weather prediction and climate data records.

Proposed solution: Millimeter-wave differential absorption radar (DAR) offers a unique, active remote sensing system for measuring humidity inside of clouds. The 167-174.8 GHz DAR discussed here builds on years of sub-mm-wave radar development at JPL, and utilize state-of-the-art solid-state G-band components, also designed at JPL. Additionally, from an airborne (or spaceborne) platform, the radar returns from the Earth's surface allow for measurements of total column water vapor.

Earth science applications: Scientific questions that can be addressed with these high-resolution, in-cloud humidity profiles include the coupling of cloud cover to the vertical distribution of water vapor, the dependence of ice-crystal growth rate on humidity, and the vertical transport of water vapor within the boundary layer.

The differential absorption radar (DAR) method

- Same methodology as the mature differential absorption lidar (DIAL) technique
- Exploit frequency-dependent absorption in the vicinity of water vapor absorption line (183 GHz)
- Assumes frequency independence of reflectivity and extinction from hydrometeors
- Measure ratios of radar echo powers from different ranges ⇒ hardware systematics (common mode) cancel out
- Use *relative* measurement to extract *absolute* humidity

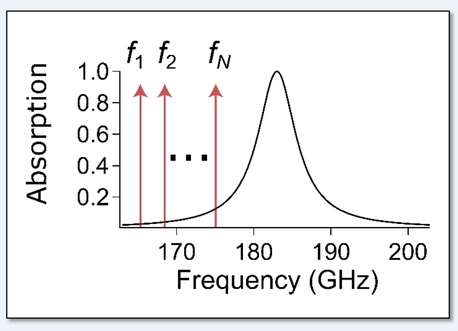

$$\frac{P_e(r_2,f)}{P_e(r_1,f)} \propto e^{-2\alpha(r_1,r_2,f)}, \quad \alpha(r_1,r_2,f) \propto \frac{\kappa(f)}{r_2-r_1}\int_{r_1}^{r_2}\rho_v(r')dr'$$

Range-resolved echo power

One-way optical depth proportional to line shape function κ and average humidity ρ_v

The vapor in-cloud profiling radar (VIPR)

- Proof-of-concept, airborne DAR for in-cloud humidity profiling
- Surface returns enable total column water measurement
- Tunable G-band transmitter (up to 500 mW) spanning restriction-free (IUT) 167 – 174.8 GHz band
- Radar operated in frequency-modulated, continuous-wave (FMCW) configuration to maximize sensitivity given transmit power limitations
- Novel mm-wave components designed at JPL include:
  1. High-power, GaAs Schottky diode frequency multipliers
  2. InP low-noise amplifiers (T_N = 500 K)
  3. Polarization-based Tx/Rx duplexing (90 dB isolation)

VIPR airborne radar concept

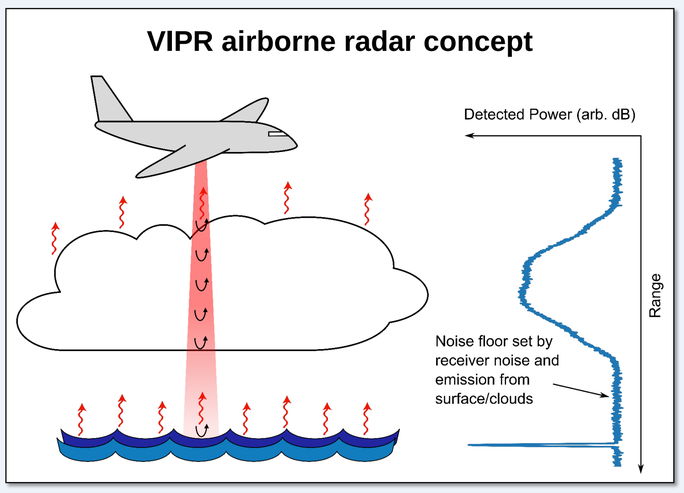

Radar block diagram

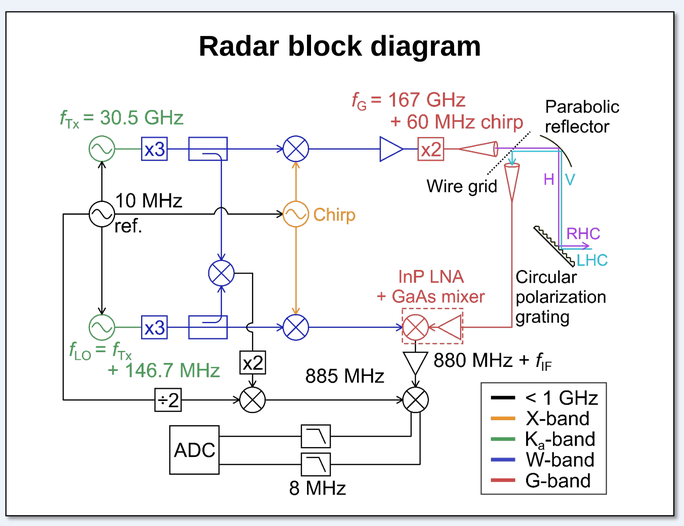

FMCW radar basics

- Carrier modulated with linear chirp
- Homodyne detection converts time-delay of echo chirp to static frequency offset in IF band (f_{IF})
- Taking FFT of IF signal reveals range-resolved power spectrum

Radar signal processing developments

- Subtracting off noise floor contribution to detected power spectrum critical for accurate humidity retrieval
- Need to characterize noise floor in real time, since it can change due to changing scene brightness temperature (e.g. different surfaces) and hardware drift
- Use sequential frequency chirps of opposite slope (i.e. triangle-wave) ⇒ radar spectrum reflects about zero-range point in IF band ⇒ acquire noise spectrum in real time and *no loss of duty cycle*
- Implemented data acquisition software in Python with real-time signal processing, data compression, and display – resulting duty cycle >90%.

Triangle-wave chirp for noise floor subtraction

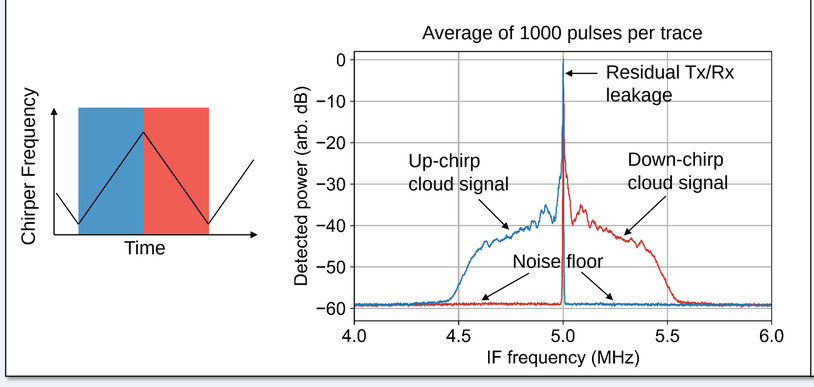

Data flow diagram

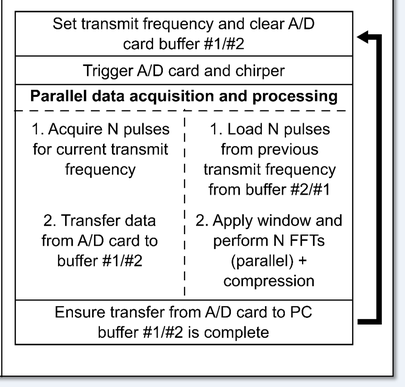

Ground testing and humidity retrieval

We currently have an operational ground-based radar, and have performed tests of the DAR method and associated retrievals in preparation for airborne measurements.

Experimental parameters

- Radar pointing angle: 30˚ above horizontal
- Chirp/pulse duration: 1 ms
- Radar range resolution: 2.5 m
- 12 equally spaced transmit frequencies from 167-174.8 GHz
- Pulses acquired per transmit frequency: N_p = 2000
- Average N_p radar power spectra and subtract noise floor to get echo power, P_e

Cloud detection and differential absorption observation at JPL (March 14, 2018)

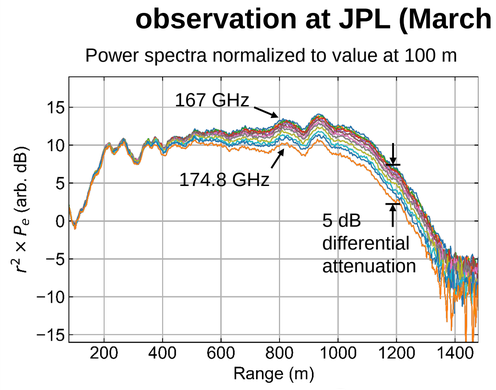

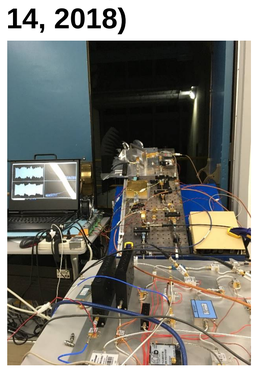

$$r^2 P_e(r,f) \propto Z(r)e^{-2\alpha(r,f)}$$

Plot power spectrum scaled by r^2 to reveal range dependence of reflectivity $Z(r)$

Retrieve humidity by fitting absorption line shape

- Three example fits for different signal-to-noise ratios (SNR)
  Note: Arbitrary offsets added for displaying purposes
- Humidity profile retrieved from above power spectra

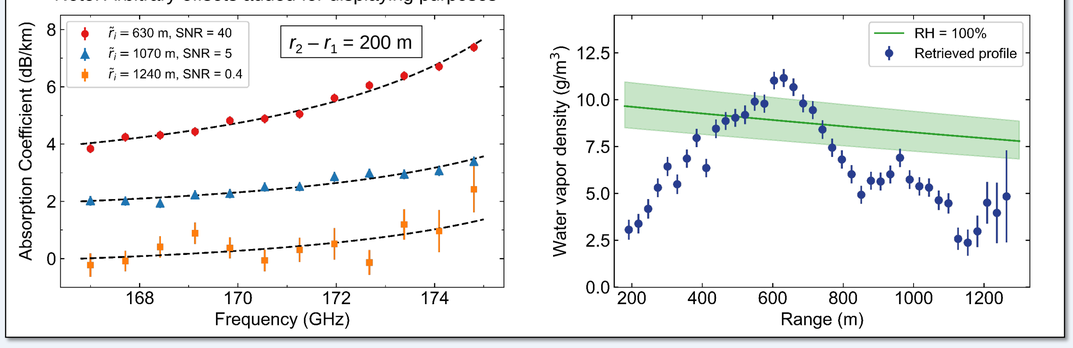

Conclusions and outlook

- A proof-of-concept humidity profiling cloud radar has been successfully tested from the ground, with high-resolution humidity retrievals implemented.
- The radar architecture includes many state-of-the-art components, employs novel signal processing techniques, and features high duty cycle operation, all of which enable future airborne measurements with high sensitivity and high throughput data acquisition.
- Near-future plans for the system include the installation of a 60 cm primary aperture, and corresponding 20 dB increase in gain, and validation of measurement accuracy from ground-based tests with coincident radiosonde measurements. The VIPR instrument will subsequently be deployed from an airborne platform.

National Aeronautics and Space Administration
Jet Propulsion Laboratory
California Institute of Technology
Pasadena, California
www.nasa.gov

Poster No. T-16

National Aeronautics and Space Administration

Let‘s Put Something New on that Spacecraft Boom –
Quantum-Engineered Silicon Carbide Solid State Magnetometry

Hannes Kraus[389R], Corey Cochrane[389R], Phil Neudeck[NASA GRC], David Spry[NASA GRC]

WHY?

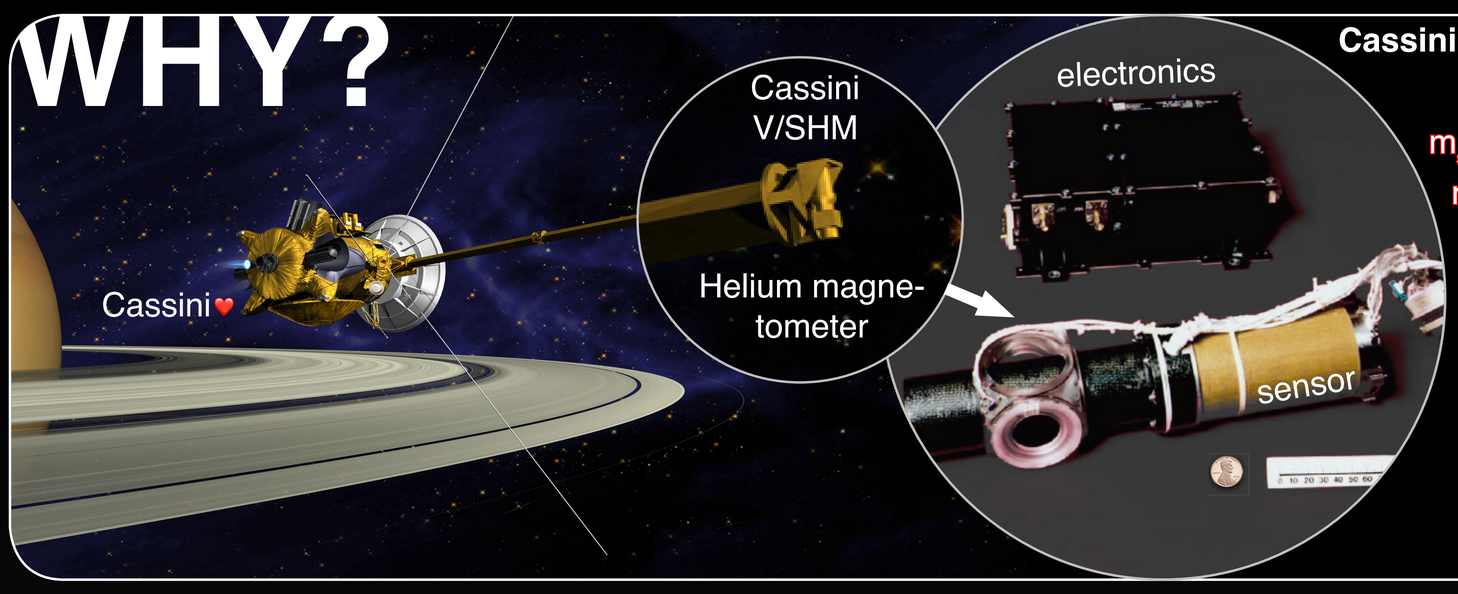

Cassini V/SHM

m_{sensor} = 0.71 kg
m_{total} = 8.82 kg
P ~ 12W
sensitivity ~ 1nT

vs.

SiCMAG

m_{sensor} < 0.1 kg
m_{total} < 0.4kg
P < 1 W (anticipated)
sensitivity ~100 nT

Silicon Carbide Solid State Magnetometer

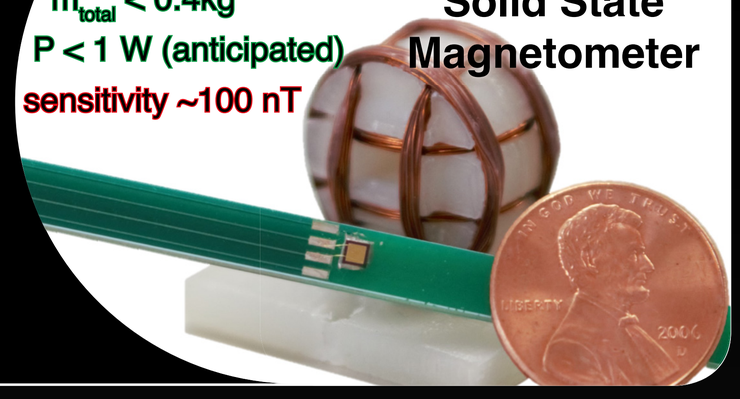

THE SENSOR

4H **Silicon Carbide (SiC)** carries optically and **spin-active** quantum centers, e.g. **silicon vacancies V_{Si}**

V_{Si} carry a $^3/_2$ **spin quartet**, whose spin states undergo a **Zeeman splitting** under an external magnetic field.

Spin **transitions** can be induced under resonance conditions $E_{Zeeman}=h\nu=g\mu_{Bohr}B$.

These spin transitions show up in changes in **device current** (electrically detected magnetic resonance – *EDMR*)

The device current also changes close to **zero field**, even without RF excitation, when the involved spin states become **degenerate** (spin dependent recombination – *SDR*)

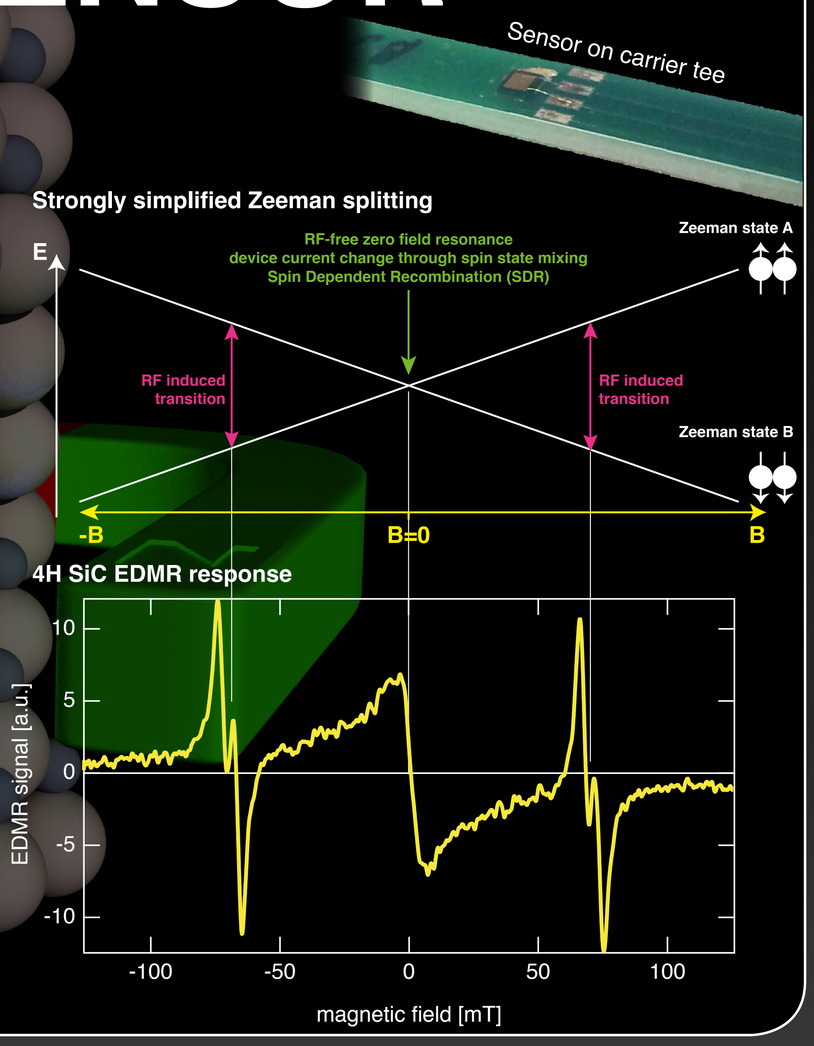

MAGNETOMETRY

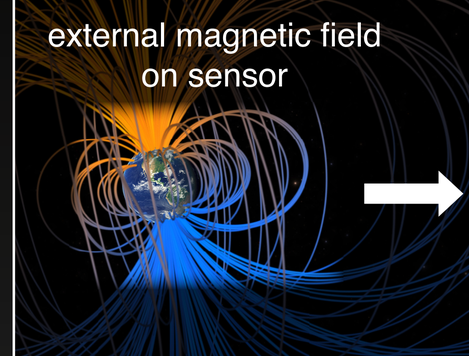

External (planetary) magnetic field lifts spin state degeneracy

Diode current changes. „Error current“ is detected

3D field coils generate nulling field to shim diode current back to zero field conditions

Nulling field current is equivalent to external field.

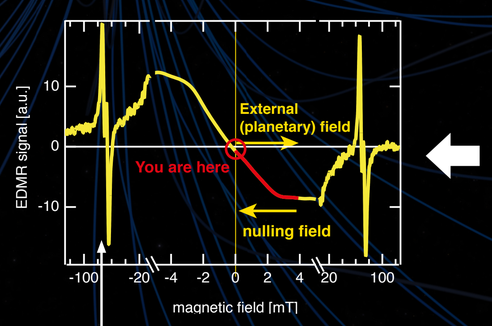

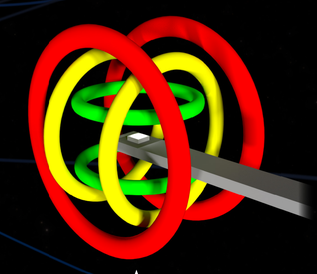

CALIBRATION

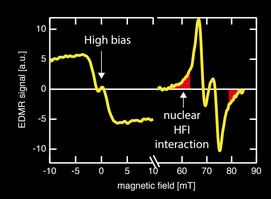

SiC EDMR has fixed features stemming e.g. from device bias or **hyperfine interaction** of band electrons with nonzero spin nuclei (Si^{29}). The latter are **temperature- and time-independent**; both can be used for self-calibration.

THREE-AXIS

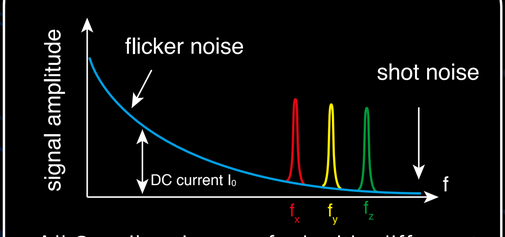

All 3 coil pairs are fed with different modulation frequencies. The diode current modulation for each field axis correlates with its frequency, and can be reconstructed through lock-in measurement.

SENSITIVITY

$$\frac{\delta B}{\sqrt{\Delta f}} = 2\boldsymbol{\sigma}\sqrt{\pi e}\frac{\sqrt{I_0}}{\boldsymbol{\Delta I}}\left(\frac{T}{\sqrt{Hz}}\right)$$

Magnetic field sensitivity (δB/√Δf) of SiCMAG‘s SiC sensor is governed by SDR linewidth **σ** and diode current modulation **ΔI**. The signal height is proportional to V_{Si} quantum center density.

We will increase quantum center density in the device interface layer by **proton irratiation**, minimizing damage to other device layers.

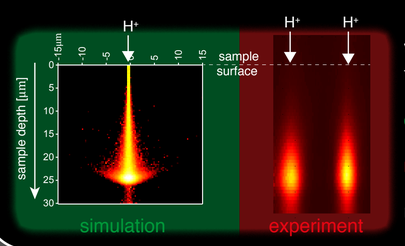

V_{Si} implantation in SiC through 1.7MeV focused proton irradiation, as **calculated** (ion stopping power in solids), and **measured** (V_{Si} emission in 3D micro-photoluminescence)

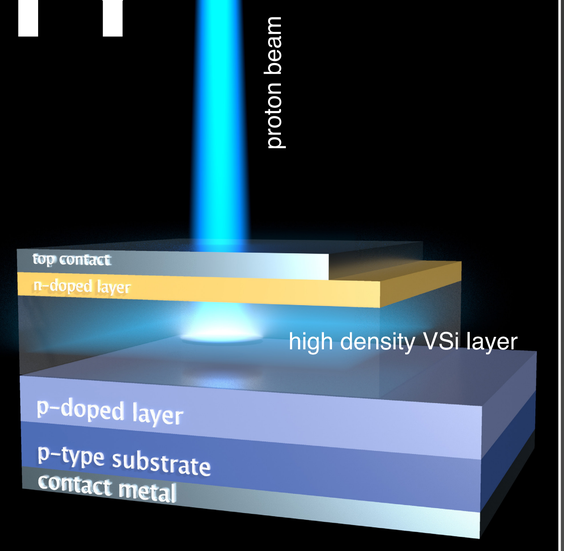

PROJECT

NASA PICASSO – **SiCMAG** (C. Cochrane)
NASA Postdoctoral Program – **SiCstSense** (H. Kraus)

2017

- ✓ Designed magnetometry specific diodes (in conjunction with NASA Glenn RC)
- ✓ Calculated irradiation parameters for fitting defect densities
- ✓ Tested commercial SiC p-i-n diodes for viability as magnetometry sensors

2018

- WIP Finalized diode design - diodes in fabrication at GRC
- WIP Engaged collaboration with irradiation facilities in Japan
- TO DO GRC devices - characterize sensitivity - assess necessary quantum center density
- TO DO Defect-engineer (irradiate and characterize) devices
- TO DO Find out more about hyperfine interaction and bias features

FURTHER READING

C. Cochrane et al.
Vectorized Magnetometer for Space Applications
Sci. Rep. 6, 37077 (2016)

H. Kraus et al.
3D Proton Beam Writing in of Vacancy Spins in SiC
Nano Lett. 17, 2865 (2017)

National Aeronautics and Space Administration

Jet Propulsion Laboratory
California Institute of Technology
Pasadena, California

www.nasa.gov

Poster No. T-19

National Aeronautics and Space Administration

Simultaneous Analysis of Inorganic Cations and Amino Acids by Capillary Electrophoresis and Contactless Conductivity Detection for Astrobiology Studies

Author: Mauro Sergio Ferreira Santos (389T)
Aaron Noell (389T), Maria Fernanda Mora (389T)

Introduction

The search for life in our Solar System is one of the highest priorities at NASA. Amino acids are powerful biosignatures in the search for life beyond Earth. The soluble constituents are also of primary importance to biological activity and the thermo-physical properties of any liquid mixture. Thus, the characterization of the distribution of inorganic ions is essential to assess the habitability of an extraterrestrial environment.

why amino acids and which ones?

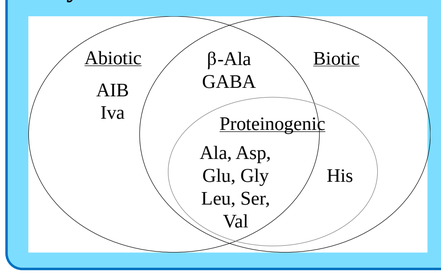

which cations?	Relevance to Planetary Studies
Mg^{2+}	Mars Phoenix Lander; likely Europa relevance
Ca^{2+}	Mars Phoenix Lander
Na^{+}	Mars Phoenix Lander; likely Europa relevance
K^{+}	Mars Phoenix Lander
Li^{+}	Hydrothermal vents, Europa, Enceladus relevance
NH_4^{+}	Possible Titan relevance

Objective

To develop analytical methods capable of measuring simultaneously inorganic cations and amino acids in samples of varying salinity by capillary electrophoresis with contactless conductivity detection (CE-C^4D).

The Challenge

To develop a method that allows the detection of amino acids and inorganic salts in samples of low, medium, and high salinity while being simple and compatible with flight systems.

Materials and Methods

- The separation and detection was performed by CE-C^4D;
- A set of 12 amino acids and 6 inorganic ions was selected;
- Five separation conditions employing different background electrolytes (BGE) were evaluated;

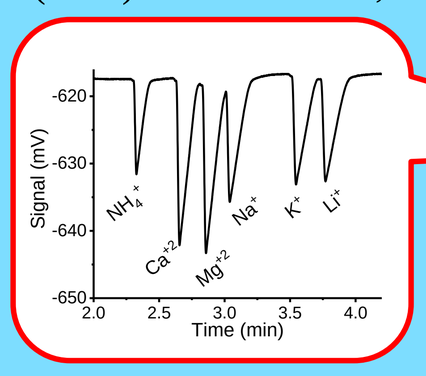

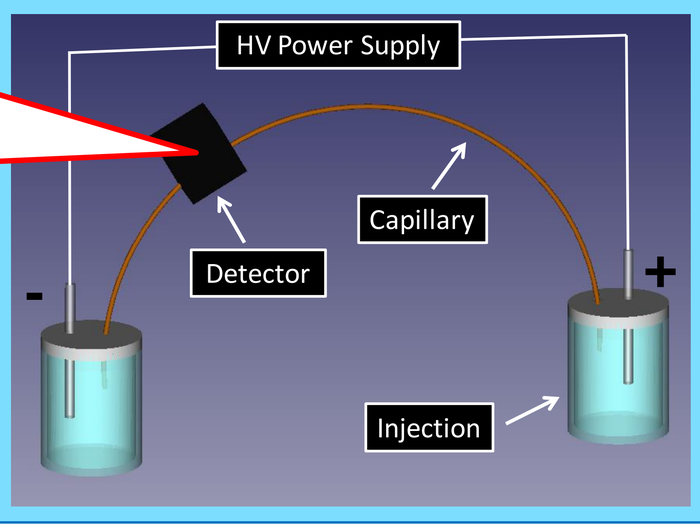

Fig. 1: Schematic drawing of a capillary electrophoresis system showing also a typical separation obtained for inorganic ions.

Results

Herein, we focus on analysis of samples of varying salinity that would be relevant for multiple planetary targets like Mars, Europa or Enceladus. Table 1 summarizes the performance of the conditions studied.

Table 1: Composition and performance of BGEs evaluated.

BGE	Composition	Pros / Cons	Inorganic ions separation	Amino acids detection	Flight compatibility	Salt tolerance	
						<50 mM	>50 mM
I	0.5 M Formic acid, 3 mM 18-C-6, 7.5% MeOH	Unstable baseline, poor LOD for amino acids	✓	✓	✗	✗	✗
II	0.5 M Acetic acid, 10 mM 18-C-6, 10% ACN	Compatible with CE-MS	✓	✓	✓	✓	✗
III	0.5 M Acetic acid	Compatible with CE-MS, no additives	✗	✓	✓	✓	✗
IV	2 M Acetic Acid	Compatible with CE-MS	✗	✓	✓	✓	✓
V	5 M Acetic Acid	No additives	✓	✓	✗	✓	✓

Results

Two buffers systems that could handle low and high salinity samples were selected for further studies (Fig. 2).

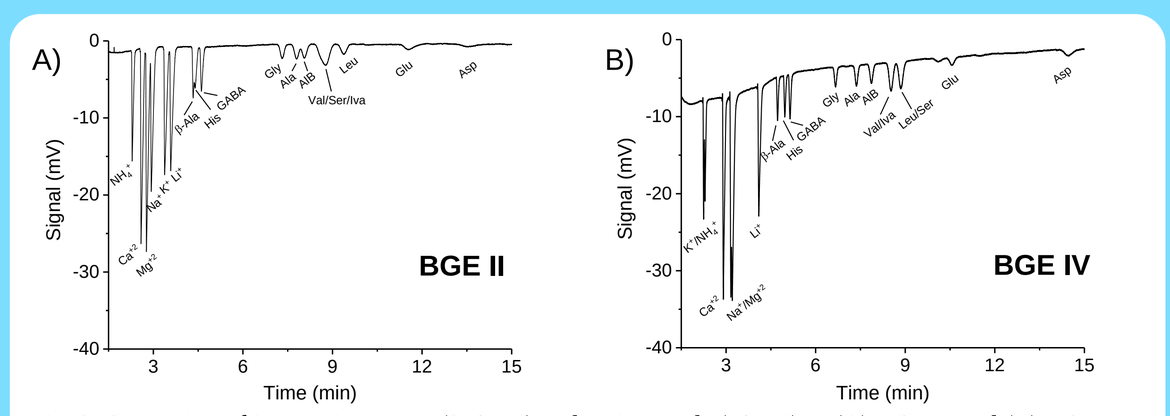

Fig. 2: Separation of inorganic cations (250µM) and amino acids (50µM) in (A) BGE II and (B) BGE IV.

Both methods were validated by analyzing samples from relevant environments with increasing salinity levels (Fig. 3 to 5)

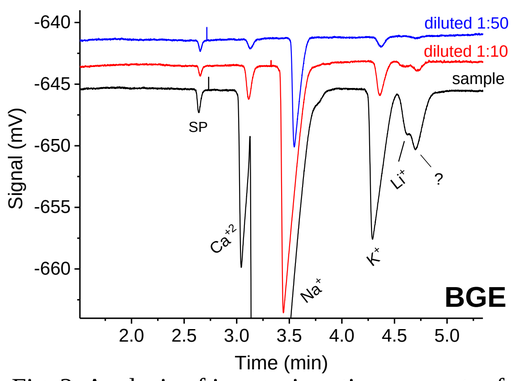

~6 mM of salts on creek water

Fig. 3: Analysis of inorganic cations on water from Hot Creek, CA.

Although amino acids were not observed on Hot Creek samples, BGE II allows the detection of inorganic ions in less than 7 minutes.

Cation	Concentration (mM)
Ca^{+2}	0.061 ± 0.002
Mg^{+2}	ND
Na^+	4.91 ± 0.07
K^+	0.210 ± 0.007
Li^+	NQ

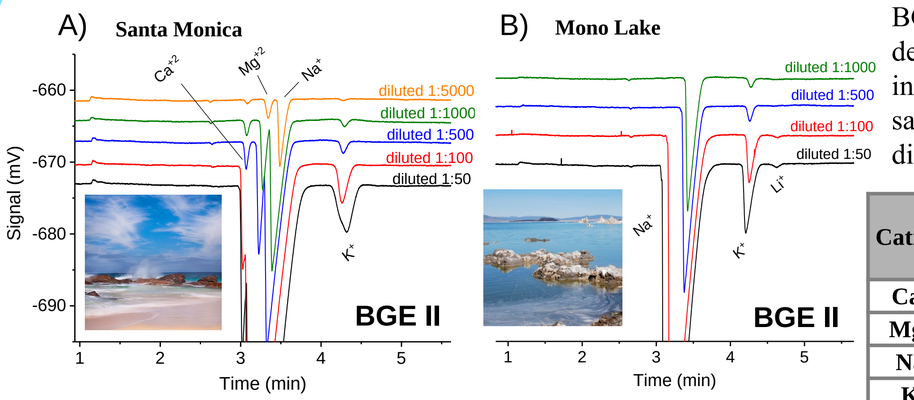

Fig. 4: Analysis of inorganic cations on (A) seawater from Santa Monica beach, and (B) Mono Lake water.

BGE II also allows the detection of inorganic ions in samples of much higher salinity after multiple dilutions.

Cations	Santa Monica (mM)	Mono Lake (mM)
Ca^{+2}	4.0 ± 0.2	ND
Mg^{+2}	30.4 ± 0.7	ND
Na^+	460 ± 20	245 ± 6
K^+	5.81 ± 0.01	5.10 ± 0.08
Li^+	ND	NQ

The detection of amino acids in high salinity samples was demonstrated using BGE IV on samples from Mono Lake. The two most common amino acids in biological samples Gly and Ala were detected demonstrating the screening capabilities of the technique.

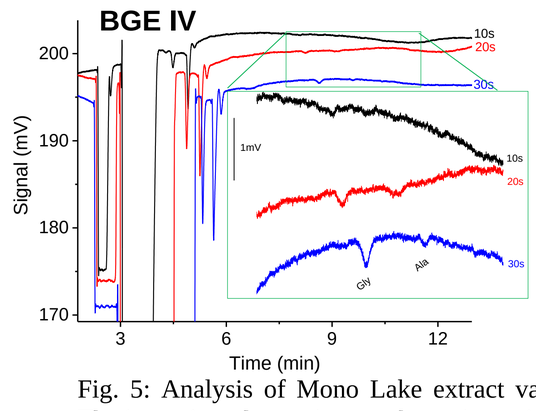

Mono Lake Water

Fig. 5: Analysis of Mono Lake extract varying the injection time. The insert is a closer view on the amino acids signal.

Concluding Remarks

- The selection of BGE depends on the sample salinity;
- BGE II allows inorganic cations quantification in samples of low and high salinity while BGE IV allows amino acids identification in high-salinity conditions;
- The selected BGE's are also compatible with CESI-MS;
- The strategies based in CE-C^4D could be used as a screening method before performing LIF analysis.

National Aeronautics and Space Administration

Jet Propulsion Laboratory
California Institute of Technology
Pasadena, California

www.nasa.gov

Poster T-21

National Aeronautics and Space Administration

Qualification of Phoenix Lander Heritage Ion-Selective Electrodes for Applications to Icy World Exploration

Author: Elizabeth Oberlin (389T)

Aaron Noell (389T), Richard Quinn (NASA Ames), Antonio Ricco (NASA Ames), Robert Gold (John Hopkins University), and Samuel Kounaves (Tufts University)

Introduction

Adapting flight proven technology from previous missions to Mars for use on icy worlds will reduce the time and cost associated with icy world exploration. The Wet Chemistry Lab (WCL) ion-selective electrodes (ISEs) used on the Phoenix lander successfully measured the pH and soluble primary cations in the Martian regolith. Due to their large dynamic range ISEs are well suited to measure the concentration of inorganic ions in unknown aqueous samples, and thus, are ideally suited for icy world exploration. To address the advances made in ISE technology since the design of the WCL ISEs, we are simultaneously developing a next generation solid contact (SC ISE) suitable for space flight.

Conclusions

- Carbon Black or SWCNT/graphene oxide solid contact layer allows for stable, miniaturized design
- Robustness to dehydration is sensitive to membrane plasticizer
- Robustness to radiation is ionophore dependent

Method

Performance of ISEs is evaluated based on sensitivity (calibration slope) and stability (standard potential and potential drift over time). Using these metrics we are comparing:

- 5 different materials for SC-ISEs
- WCL and SC ISEs after prolonged dehydration storage
- WCL and SC ISEs after exposure to 300krad radiation

Results

ISEs stored at < 0.5% relative humidity for 1 month

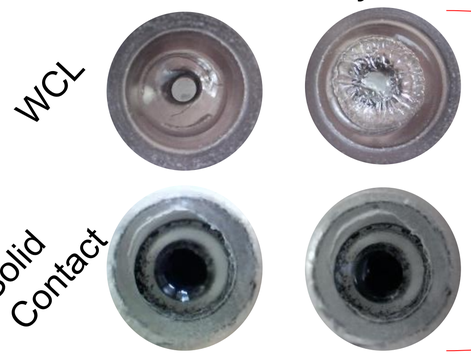

Despite visible dehydration of hydrogel. ISE performance depended on plasticizer, not transducing material

Two plasticizers with different lipophilicities were tested:

- 20% of DOS (log P = 10.9) based ISEs did not calibrate after storage
- 50% of NPOE (log P = 5.9) based ISEs did not calibrate after storage
- SC and WCL ISEs had the same percent failure after dehydration

ISEs exposed to 300 krad radiation

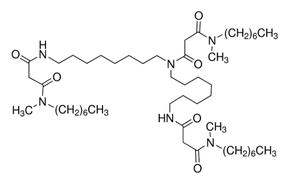

Mg Ionophore IV based ISEs

ISEs with Mg ionophore IV saw a 30% greater reduction in selectivity from the control

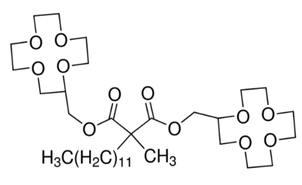

Na Ionophore VI based ISEs

ISEs with Na ionophore VI showed no reduction in selectivity from the control

Heritage WCL design:

6 mm diameter

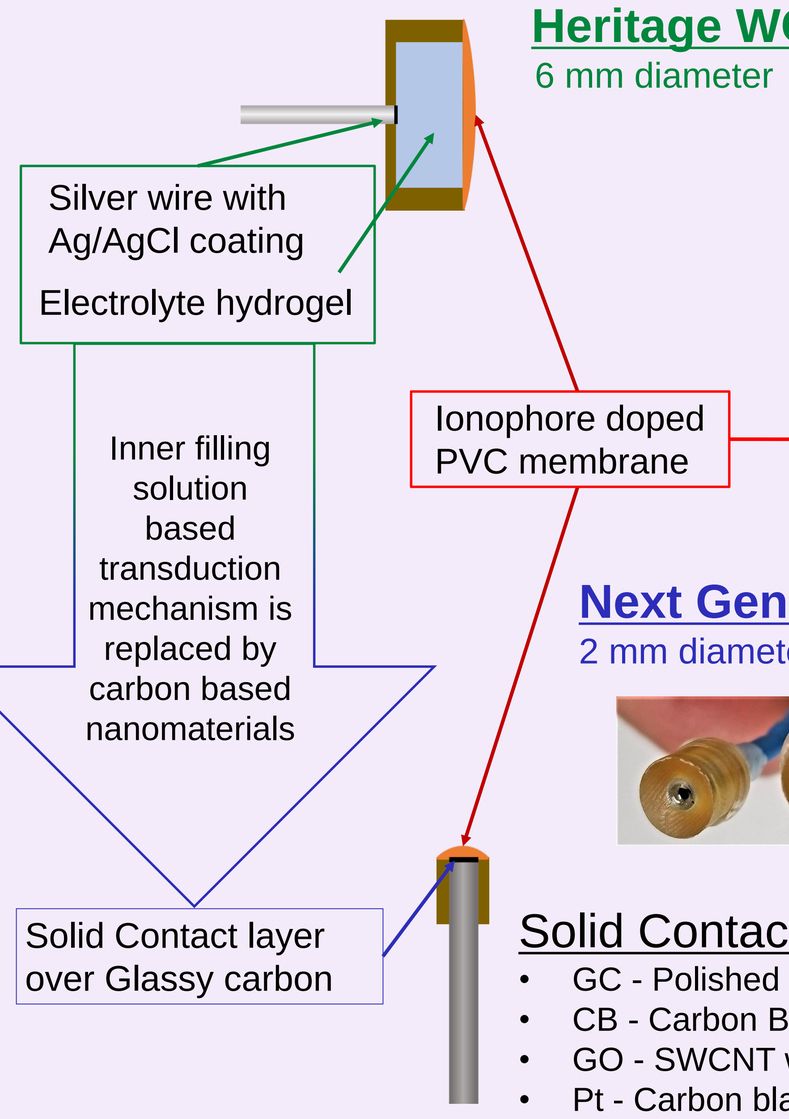

Next Gen SC design:

2 mm diameter

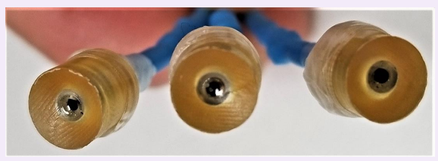

Solid Contact (SC) Layers

- GC - Polished Glassy Carbon
- CB - Carbon Black
- GO - SWCNT with graphene oxide
- Pt - Carbon black with nanoparticle Pt
- ETH - SWCNT with ETH500

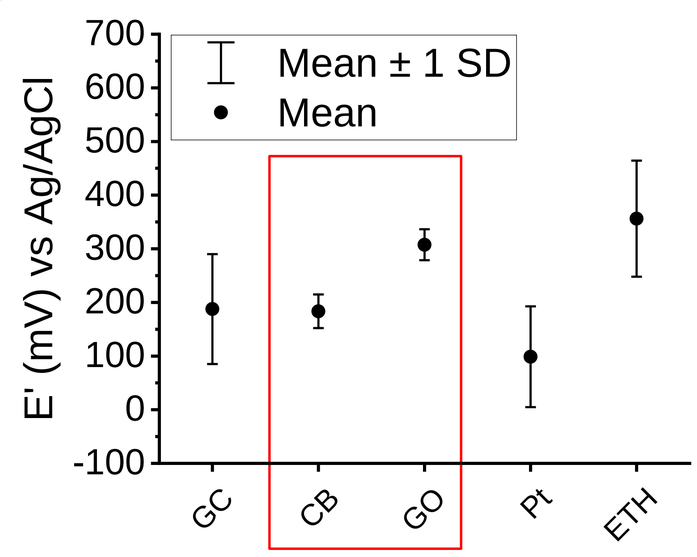

Carbon Black or SWCNT/GO solid contact layers are the most stable.

Next Steps

- Test ‘dry conditioning’ method to add robustness to dehydration
- Identifying ‘radiation resistant’ ionophore structures
- Continue comparing CB and GO SC-ISEs for long-term stability
- Perform more in depth impedance studies to elucidate the mechanism of ISE damage during dry storage and irradiation

National Aeronautics and Space Administration

Jet Propulsion Laboratory
California Institute of Technology
Pasadena, California

www.nasa.gov

Poster No. T-22

National Aeronautics and Space Administration

Europa Orbit Family Catalog

Author: Dayung Koh (392K), Rodney L. Anderson (392K)

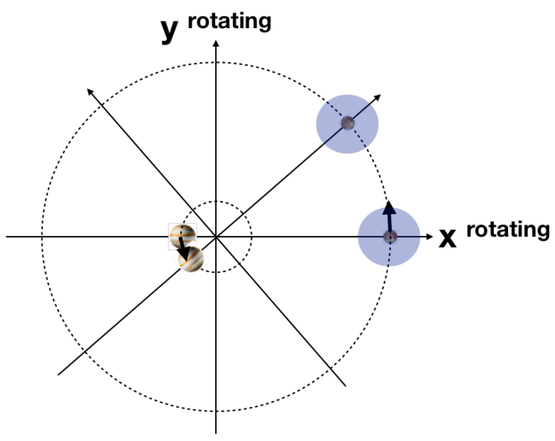

Problem

Extend our knowledge of the natural dynamical behavior around Europa to improve the design of orbit transfers in low-energy regimes.

Build a periodic-orbit catalog for Europa which includes an extensive set of families of three-dimensional solutions and bifurcations using cell mapping.

The invariant manifolds of these orbits may then be studied to form natural transitions between orbits.

Motivation

Exploring undiscovered systems or the global system behavior of known systems is challenging.

The use of libration point orbits, such as those used for the Genesis mission, opened up the possibility of flying an entirely new class of missions that are widely used today.

The current study is focused on exploring low-energy trajectory options for a potential Europa lander.

Cell Mapping Method

Benefits

+ Generic, Systematic
+ Easy to implement for any type of nonlinear dynamics EOM
+ Generates
  - Multiple-period periodic solutions
  - Invariant surface
  - Regions of attraction

Applications

+ Periodic orbits in the CRTBP
+ Periodic motion analysis of Spacecraft
+ Orbit and attitude coupled Periodic motion analysis around asteroids and other bodies

Result

Orbit Catalog

+ 10 families of orbits
+ Dimensionless Orbital Period **T** = 0.133 – 13.31
+ Jacobi constant **C** = 2.89773 -- 3.00375

Contribution

+ An orbit catalog with large range of Jacobi constant and periods of periodic orbit families is built
+ Found highly inclined and/or asymmetric 3D orbits
+ Studied bifurcation orbits to find global characteristics of the system
+ The study opens more options for landing and escape trajectories to/from Europa.

1 Select a cell state space and divide it into a finite number of cells

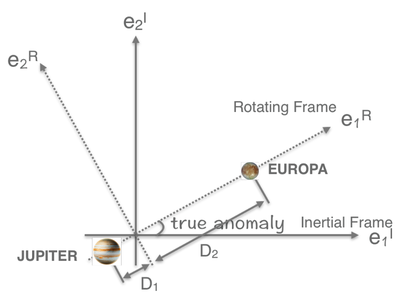

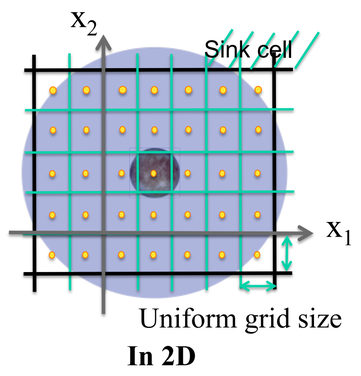

In 2D

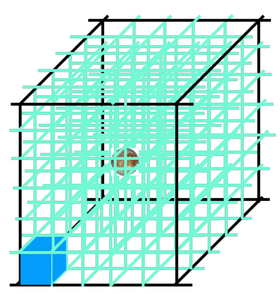

In 3D

2 Develop a cell mapping for the state space by integrating EOM

CONTINUOUS TIME → DISCRETE TIME

$\dot{X} = f(t, X(t), s)$ — f : any type of nonlinear system; X : state variable

$z(n+1) = C(z(n))$ — C : cell mapping; z : cell number

Cell mapping result (matrix)

Shown selected cells only

z	1	2	3	4	5
C(z)	9	9	10	10	…
z	6	7	8	9	10
C(z)	…	…	…	9	9
z	11	…	33	34	35
C(z)	…	…	25	…	…

(P – K solutions: K period of periodic solutions)

Cell mapping procedure

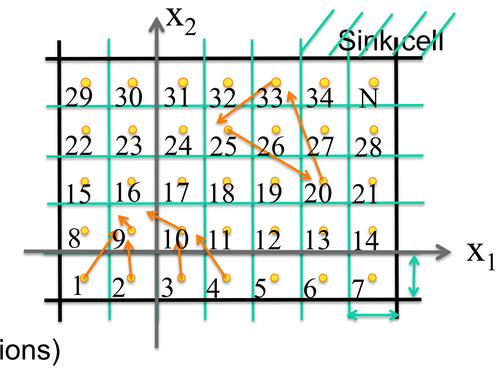

3 Employ the unraveling algorithm

4 Refine the solutions for a tolerance of approximately 1e-10

5 Evaluate the local stability characteristics and bifurcation conditions

1 Distant Retrograde Orbit Family (DRO)

Description: Planar, all stable, several bifurcations
Energy: C = 3.010499097 − 2.89773655
Dimensionless Period: T = 0.133 − 6.28

Bifurcations
P-1 to P-3 : C=2.99991236, T=2.504
P-1 to P-4 : C=3.00060754, T=1.65
P-1 to P-5 : C=3.000548827, T=1.7052
P-1 to P-6 : C=3.001068736, T=1.295

DRO P-1, P-3, P-4

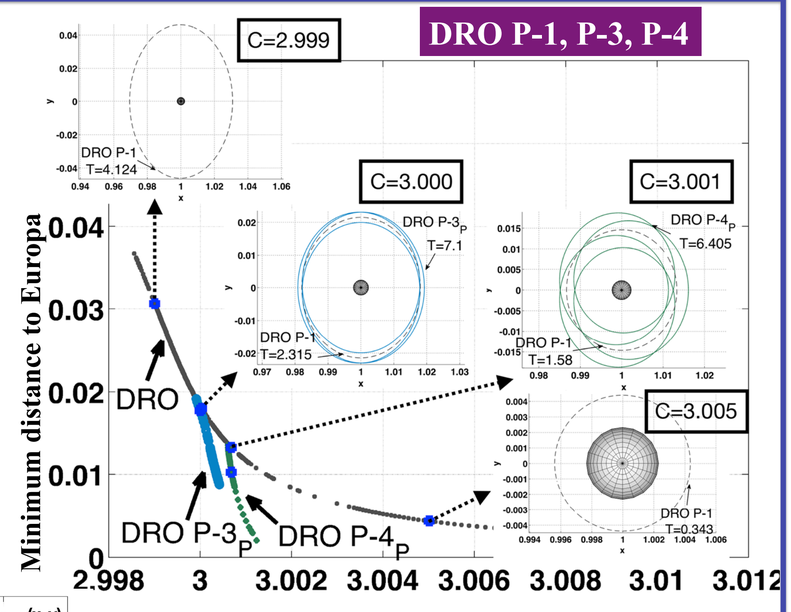

DRO P-6

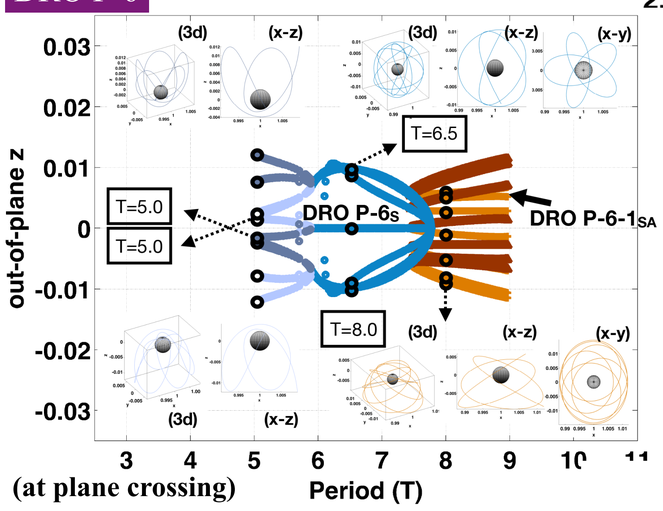

DRO Bifurcation Diagrams

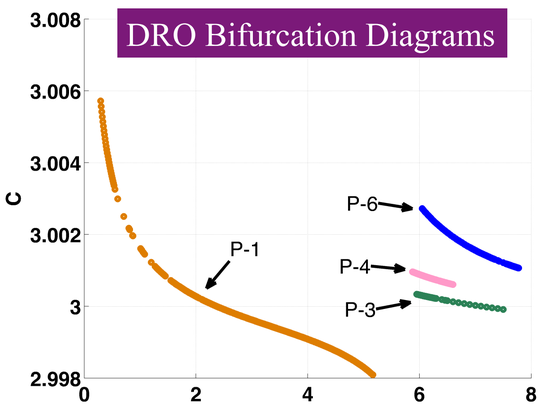

2 High Altitude Orbit Family (HAOhat)

Description: symmetric, asymmetric, unstable
Energy: C = 3.002604695 − 3.002375486
Dimensionless Period: T = 8.7 − 10

(impact the surface : T = 8.7 − 9.1 and C = 3.00260 − 3.00262)

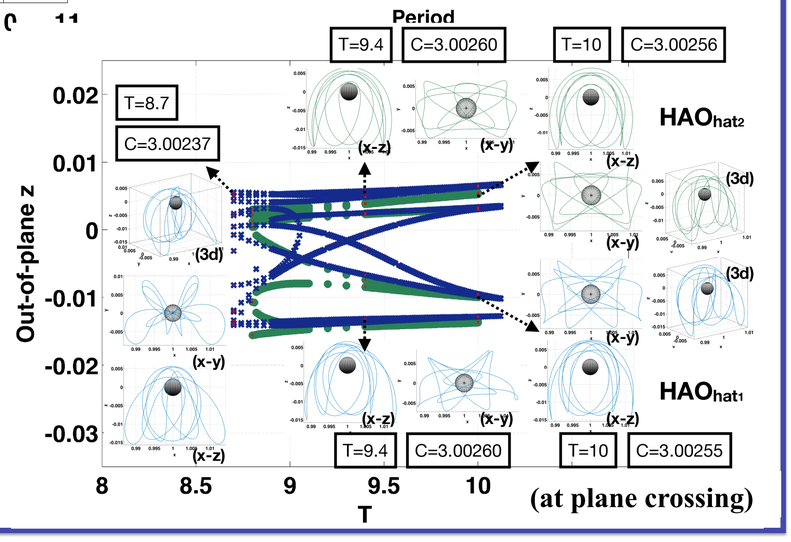

National Aeronautics and Space Administration
Jet Propulsion Laboratory
California Institute of Technology
Pasadena, California

To be presented at the 2018 AAS/AIAA Astrodynamics Specialist Conference, 19 - 23 August, Snowbird, Utah.

www.nasa.gov

Poster No. T-25

Long Term Asteroid Orbit Deflection Optimization

Siegfried Eggl (392-R)

Steven R. Chesley, Davide Farnocchia, Paul Chodas (392-R)

National Aeronautics and Space Administration

Introduction

The past decades have lead to great advances in space situational awareness. The majority of asteroids that could cause global disasters if striking the Earth, for instance, are now tracked on a regular basis [1-3]. The whereabouts of the vast majority of 100 m sized near-Earth objects (NEOs) remain largely unknown, however [4]. Should an asteroid be discovered and predicted to impact our planet near a population center, humankind now has the option of sending a space-mission to deflect the potentially hazardous object. A kinetic impactor (KI) spacecraft, for instance, could transfer momentum to the asteroid through a high velocity collision, thus changing the orbit of the latter. Differences in asteroid shape and composition, however, cause the magnitude and direction of the delivered momentum to be to some degree uncertain [5-7].

Kinetic Impact Momentum Enhancement

The change in an asteroid's heliocentric velocity vector ($\Delta\vec{V}$) caused by a kinetic impact can be described through the following momentum transfer equation [8]

$$\Delta\vec{V} \approx \frac{m}{M}[\vec{v}_\infty + \vec{\beta}], \qquad \vec{\beta} = (\beta - 1)(\vec{n}\cdot\vec{v}_\infty)\vec{n}, \qquad (1)$$

where M is the asteroid's mass, $\vec{n}$ the surface normal vector at the location of impact and m and $\vec{v}_\infty$ the impactor spacecraft's mass and relative velocity, respectively.

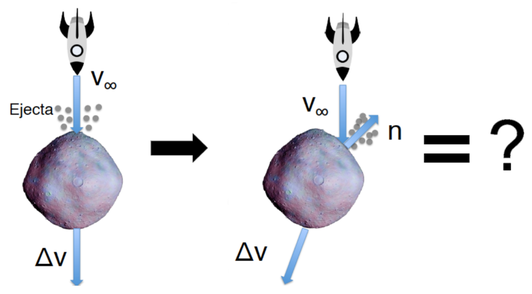

Figure 1: KI based asteroid deflection.

Ejecta from the impact crater that escape the gravitational sphere of influence of the asteroid cause an additional momentum enhancement ($\vec{\beta}$). Thus, the magnitude and direction of $\Delta\vec{V}$ depends on $\vec{\beta}$. Laboratory experiments and modeling efforts have seen some success in estimating the range of possible β values [5-7]. However, uncertainties in the direction and magnitude of the net ejecta momentum vector remain uncomfortably large, in particular due to a dependency on a target's shape [8-9]. Accounting for those factors, where should a potentially hazardous object best be targeted and what consequences for future encounters with the Earth can be expected?

Keyholes

The asteroid (101955) Bennu is the target of NASA's OSIRIS-REx mission (OREx) [10]. Bennu has several close approaches with the Earth in the near future. The effects of close encounters with our planet on an asteroid's orbit are best studied on the 2-body scattering plane (b-plane) [11]. The probability density of finding Bennu at a specific location with respect to the Earth during a close approach in 2135 is shown, for instance, in Figure 2. So-called '*keyholes*' are an ensemble of states that lead to future collisions with the Earth. Those states can be mapped onto the b-plane. For Bennu the location and size of keyholes in the 2135 b-plane are represented by vertical bars in Figure 2b. Bennu could enter a keyhole during its close encounter with the Earth in 2135 resulting in an impact 40-50 years later.

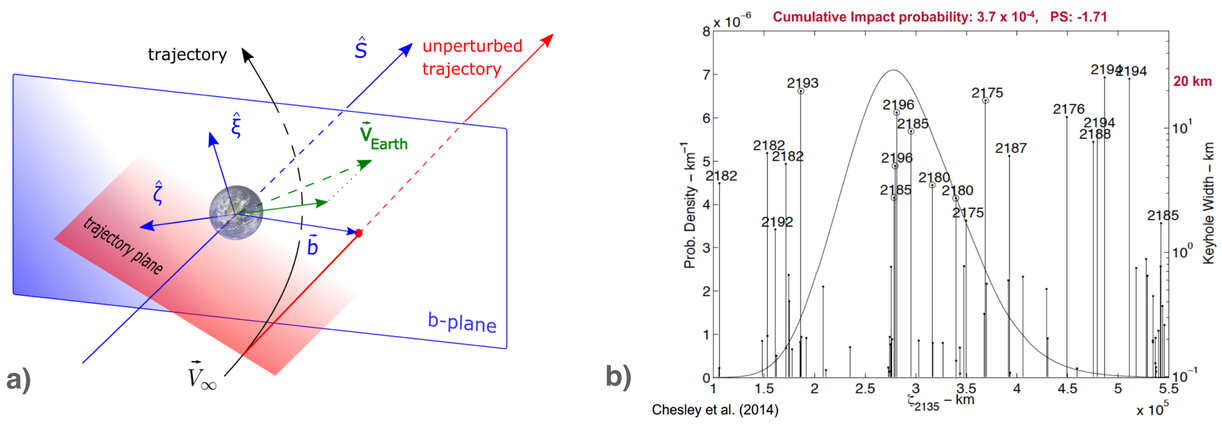

Figure 2: a) Sketch of the b-plane during a close approach of an asteroid (black trajectory) with the Earth. b) PDF and keyholes for Bennu during its close encounter with the Earth in the year 2135.

Would a timely orbit deflection mission reduce the probability of a collision with the Earth? Arriving at the asteroid in 2021 with a relative speed of 14.9 km/s a hypothetical impactor could change the heliocentric velocity of Bennu by up to 0.2 mm/s. This would alter Bennu's position in the 2135 b-plane enough to avoid a specific keyhole. The exact effect such a mission would have on future encounters between Bennu and the Earth depends not only on the momentum delivered by the impactor spacecraft itself, but also on the amount and direction of the momentum carried by crater ejecta. The shape and composition of the target asteroid plays a crucial role in this respect due to $\vec{\beta} = \vec{\beta}(\vec{n})$.

Summary

Without accurate information on where an asteroid is 'parked' after a deflection attempt, the same object may become a concern for planetary safety at a later date. In the worst case, the target asteroid enters a so-called 'gravitational keyhole', retaining a high probability to collide with our planet. In order to avoid such scenarios, we demonstrate how to best target an asteroid during a kinetic deflection maneuver so as to minimize the chances of an Earth impact in the foreseeable future. Keyhole avoidance maps are potent tools in this respect, allowing for an informed choice of a target location for kinetic impactor missions.

Keyhole Avoidance Maps

For a given kinetic impactor spacecraft approach trajectory we find locations on the surface of Bennu that, if hit, would push the asteroid into a keyhole leading to a future collision with the Earth (Figure 3a). Such keyhole avoidance maps are useful tools, but they require careful interpretation, as the amount of ejecta and the rotation phase of the asteroid both influence the location of keyholes on the surface (Figure 3b).

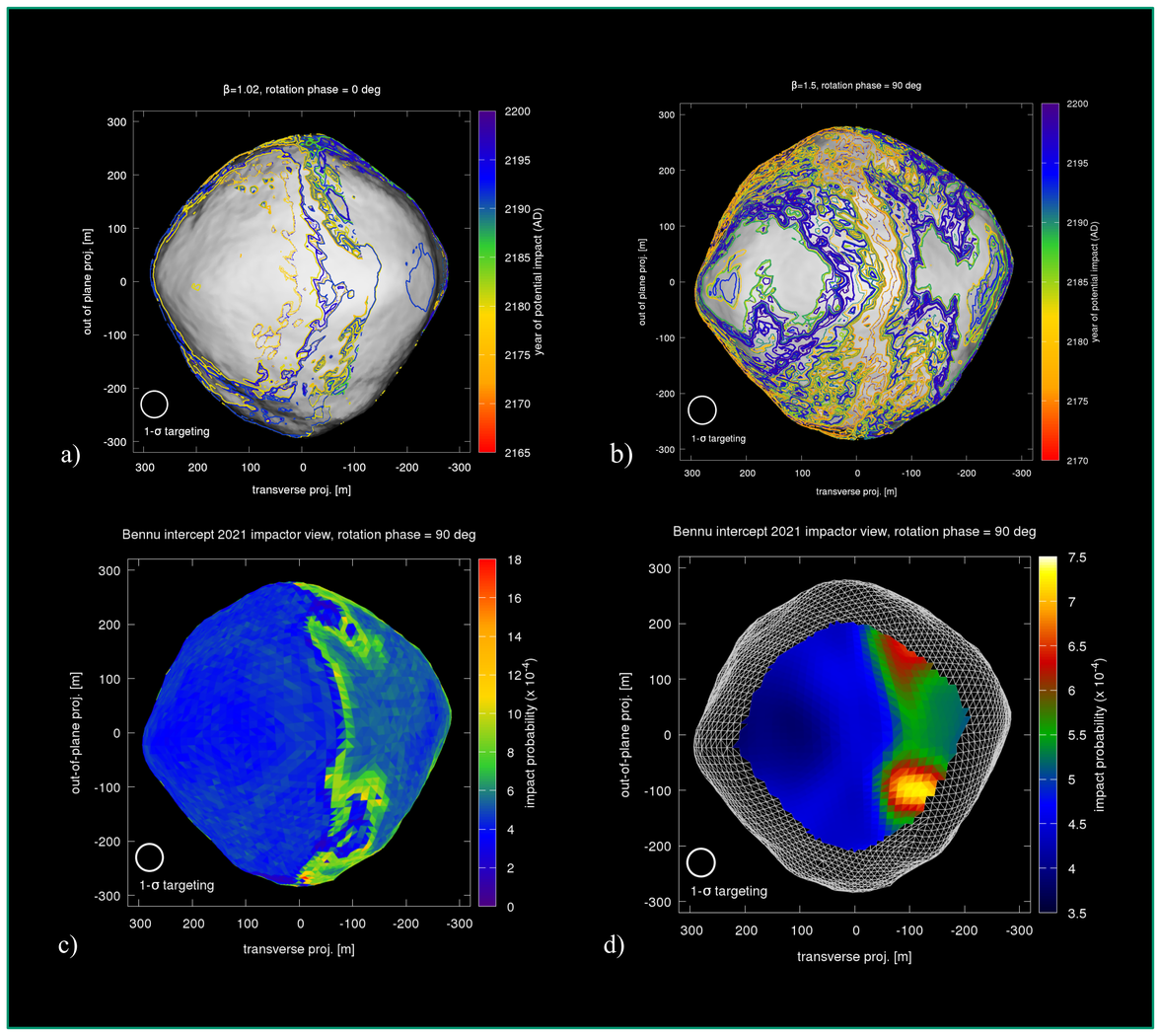

Figure 3: The b-plane displacement (top) and impact probability (bottom) for a simplified (left) and realistic shape (right) of the near-Earth asteroid (101955) Bennu are shown from an impactor spacecraft's perspective in the radial, transverse and out-of-plane system aligned with the asteroid's orbit.

In order to determine the impact location on the asteroid that would yield the lowest collision risk with our planet after the deflection attempt, we performed Monte-Carlo simulations assuming a uniform distribution of β between 1 and 3, (Figure 3c) as well as a 3-σ targeting uncertainty of 75 m with a Gaussian envelope (Figure 3d). Only the center region of the asteroid is targeted so as to avoid a miss. For a realistic shape model the orientation of the object at the time of impact needs to be considered. Targeting uncertainties and the shape of the asteroid influence the optimum impact location. Aiming for the center of the target would not necessarily be the best choice in terms of lowering the post deflection impact probability (Figure 3d). Similarly, maximizing the miss distance in 2135 would not guarantee a low future impact risk either. Figure 3d shows that the best place to hit Bennu is 'left' of the center, effectively slowing the asteroid on its heliocentric orbit. Targeting maps are useful tools to understand and optimize post deflection orbits of potentially hazardous asteroids in a quantitative fashion.

References

[1] Milani, A., et al. *Icarus* 173.2 (2005): 362-384.
[2] Chamberlin, A. B., et al. (2001): *Bulletin of the American Astron. Soc.* Vol. 33.
[3] Chodas, P. (2015): In *AAS/DPS Meeting Abstracts* (Vol. 47).
[4] Harris, A.W., & D'Abramo, G. *Icarus* 257 (2015): 302-312.
[5] Flynn, G. J., et al. *Planetary and Space Science* 107 (2015): 64–76.
[6] Jutzi, M. & Michel, P. *Icarus* 229 (2014): 247–253.
[7] Holsapple, K. A. & Housen, K. R. *Icarus 221* (2012): 2, 875-887.
[8] Scheeres D. J. et al. (2015), *Aerospace Conference* (2015): IEEE, 1-7.
[9] Eggl, S. et al. *Advances in Space Research* 56 (2015): 528–548.
[10] Valsecchi, G. B., et al. *Astronomy & Astrophysics* 408.3 (2003): 1179-1196.
[11] Chesley, S. R., et al. *Icarus* 235 (2014): 5-22.

Acknowledgements

This research has received funding from the Jet Propulsion Laboratory through the California Institute of Technology postdoctoral fellowship program, under a contract with the National Aeronautics and Space Administration.